ISOTHERMAL AND NON-ISOTHERMAL COMPARATIVE STUDY OF Zn-Sn SYSTEM USING REAL-TIME RBS

Mmangaliso Mpilonde Mnguni

A thesis submitted in partial fulfilment of the requirements for the degree of

Magister Scientiae.

UNIVERSITY OF THE WESTERN CAPE

&

iThemba LABS-NRF

Supervisor: **Dr. Lebogang Kotsedi**

Tandetron Laboratory

iThemba LABS-NRF

Co-Supervisor: **Dr. Remy Bucher**

Tandetron Laboratory

iThemba LABS-NRF

December 2021

Declaration

Student Number: 3987046

I declare that **Isothermal and non-isothermal comparative study of Zn-Sn system using Real-time RBS** is my work and that all sources that I have used or quoted have been indicated and acknowledged by means of complete references.

Signature: **Date:**

Mmangaliso Mpilonde Mnguni

Abstract

Insight into the effects of isothermal and non-isothermal annealing on bi-metallic thin film is important for material synthesis and application in everyday use. The effects of isothermal annealing on bi-metallic thin films has long been studied using various heating methods from a resistively heated filaments, by transferring heat via conduction, convection and irradiation. The effect of each method have been widely reported in literature. The diffusion coefficient and activation energies of the constituent atoms can calculated for each annealing method.

On the other hand, the effects of non-isothermal annealing on bi-metallic thin films has not been comprehensively studied, and there are areas of this annealing regime that need further investigation. In this study a femtosecond laser with a 1064 nm central wavelength was used to anneal bi-metallic thin films of Zinc-Tin (Zn-Sn) on a substrate. The experimental parameters of the laser were set such that the net fluence of the laser is below the ablation threshold of the metallic system. Rutherford backscattering spectrometry was used to study depth profile and atom mixing and migration during laser annealing. The net fluence of the laser was gently increased to study the effect of non-isothermal annealing. The diffusion coefficient and the activation energy of the system was studied using the raw data from Rutherford backscattering spectrometry. Other complimentary characterization techniques were used to have a comprehensive analysis of the samples.

Both isothermal and non-isothermal annealing of the bilayer resulted in intermixing of Zn and Sn with Sn diffusing through Zn.No alloying of Zn and Sn occurred during both isothermal and non-isothermal annealing. The activation energy and diffusion coefficient of Zn and Sn intermixing were calculated and found to be 0.46 eV and 44.6 kJ/mol respectively. X-ray diffraction (XRD) results of the bilayer showed the material to be crystalline and the absence of a peak belonging to Zn-Sn further supports that alloying did not occur.Morphological changes where observed in both isothermal and non-isothernal annealed samples. In the case of isothermal annealed samples, scanning electron microscopy (SEM) micrographs showed that the surface became smooth as the temperature increased. Atomic force microscopy (AFM) also showed a decrease in root mean square (R_a) value as the temperature increased. In the case of non-isothermal annealed samples, changes due to mixing and recrystallization of the material where observed.

Dedications

This work is dedicated to the following people:

My mother Nonhlanhla Mnguni, for her constant support throughout the years. My late grandmother BBT Mkhize, for seeing in me “uNgoye” even though I did not even know what going to uNgoye i.e., University of Zululand, meant. My uncle who sparked my interest in science Phumlani ‘Babayi’Mkhize, my sister (Amanda), brother (Mnqobi) and nephew (Siphesihle Chamane).

Abbreviations

AFM: Atomic force microscopy

XRD: X-ray diffraction

SCCM: Standard cubic centimetres per minute

PVD: Physical Vapour Deposition

CVD: Chemical Vapour Deposition

RBS: Rutherford Backscattering spectrometry

SEM: Scanning Electron Microscopy

E-beam: Electron beam evaporation

Zn: Zinc

Sn: Tin

Pb: Lead

Keywords

Atomic force microscopy

Diffusion

Femtosecond Laser

Fluence

Solid phase reaction

Microstructure

Scanning Electron Microscopy

Rutherford backscattering spectrometry

Tin

X-ray diffraction

Zinc

Acknowledgements

It takes a village to raise a child….so says the proverb.

It is with this great African proverb in mind that I wish to acknowledge the people that contributed towards the successful completion of this project. By naming names, I run the risk of omitting some people, and for that, I sincerely apologise.

- Firstly, I would like to thank my supervisor Dr Lebogang Kotsedi for the opportunity he gave me to pursue my MSc under his guidance and for the financial support. I will forever be grateful for that "out of the blue" call in April 2019.It was truly a privilege to work under such a passionate and knowledgeable person.
- I would also like to thank my co-supervisor, Dr Remy Bucher, for introducing me to XRD analysis and for helping with the analysis of XRD data.
- Dr Christopher Mtshali, thank you for teaching and training me in the use of RBS.Thank you for going above and beyond the call of duty and for always being available even when you were halfway across the world. Your patience, care for our wellbeing as students was greatly appreciated.
- Dr Zakhelumuzi Khumalo, thank you for the interest you showed in my study and for your assistant with RBS and for your guidance during the analysis of the results. Your one-on-one tutorials on XRD or RBS, were always brilliant, I sincerely hope that one day you take up lecturing at a University even on a part time basis.
- Dr N.P. Mongwaketsi, thank you for always being available to help with RBS analysis and for always being available to assist and advice.
- I would also like to thank the entire Accelerator team for always being available even after hours and on weekends.
- Dr Mlungisi Nkosi, thank you for welcoming me to your department and making my stay enjoyable.
- Ms Phumza Zantsi, thank you for everything you do for us as students at MRD.
- Dr Sifundo Khanyile, thank you for being a brother, a mentor, and a confidant. From you, I learnt patience when carrying experiments in the lab.
- Mr Muzi Mavundla, thank you for the many words on encouragements and support throughout this journey, as you always say:" *Phakama ndle'mnyama*.

- I would like to express my gratitude to my mother Nonhlanhla, my sister Amanda and my brother Mnqobi for their constant support even though they had no idea what I was up to. Special thank you to my sister Mbali Duma for showing interest in my work and for proof reading some of the chapters.
- I would also like to thank Mr Sam Sibiya from Armscor for his support and the support of the entire Armscor family, thank you for the support and making my life easier.
- My group mates, Ayanda Sobhoyise and Zizipho Mabanga, it was great working with you, wish you well in your future endeavours.
- Mr Ludwa Mbulwana, thank you for welcoming me to your house and the sacrifices you made in order not to disturb me, thank you.
- Lastly, Lungile Sangweni, my rock, my number one cheerleader, thank you for your support, understanding and for believing in me even during days when I did not believe in myself.

I end where I started, *it takes a village to raise a child*. I will forever be grateful to the many contributions that these and many other individuals made to my development as a person, a professional and scientist. It was not an easy journey made more difficult by Covid-19, Eskom and my other challenges, but your support, encouragements and understanding made it bearable.

List of figures

List of tables

Table of Contents

CHAPTER 1

Introduction

1. Background

Solid-state reactions of bi-metallic systems can be driven or activated by various external stimuli like pressure, energetic photons, energetic charged particles or heat. For an example, high pressure torsion can be applied to aluminium-copper (Al-Cu) to drive solid-state reaction [1.1]. Oh-ishi et al. [1.1] applied a pressure of 6 GPa to Al and Cu half discs. Following this, x-ray diffraction (XRD) and high-resolution transmission electron microscope (HRTEM) were used to confirm the formation of different intermetallic phases such as Al_2Cu and Al_4Cu_9.

One of the first reported case where photons were used to drive solid phase diffusion was reported in 1998 by Ditchfield et al. [1.2]. The study was carried out to study the non-thermal effects of photons illumination on surface diffusion, an important process in microelectronics fabrication. Surface diffusion governs several important steps in microelectronics fabrication including the formation of hemispherical grained silicon used in memory devices [1.2], filling of channels with metals for devices interconnection purposes among others [1.2]. In this study, germanium-indium (Ge-In) on silicon was used because the thermal diffusion of this system was well understood [1.3]. Surface diffusion was measured in ultrahigh vacuum via second harmonic microscopy when the sample was illuminated with pulsed Nd: YAG laser at a wavelength of 1064 nm [1.3]. This study showed conclusively that photons could be used to drive solid-state reactions.

Several studies in literature have shown that solid-state reactions are mostly driven by conventional thermal annealing methods such as vacuum annealing, ambient (*atmospheric*) annealing and gas ambient annealing. These annealing methods are an effective way of driving reactions in solid-state material, which could result in diffusion, alloying or improving the crystalline quality of thin film. Furthermore, annealing could also improve conductivity and surface properties of thin films [1.4].

Hakeem et al. [1.5] made use of vacuum annealing to study the effect of annealing on the surface of hafnium oxide (HfO_2). After depositing thin films with electron beam (*e-beam*), the films were subjected to vacuum annealing at 500 °C for 1 hour. The films were then

characterized with XRD, atomic force microscopy (AFM) and optical spectrophotometry. It was found that HfO_2 which was amorphous pre-annealing transformed to polycrystalline monoclinic post-annealing. The surface roughness of the thin films decreased, and reflectivity increased post-annealing.

Annealing can also be carried out under various atmospheres for example air, argon, nitrogen, and hydrogen. Zulkifle et al. [1.4] studied the effect of annealing zinc oxide (ZnO) for field emission display in hydrogen atmosphere. ZnO thin films were deposited with Radio frequency sputtering on a glass substrate. Subsequently, the films were annealed at 100 °C, 200 °C and 450 °C respectively at a hydrogen flow rate of 100 sccm. The films were then characterized with XRD, AFM, UV-VIS, and Raman spectroscopy. The study showed that both sheet resistance and field emission improved with annealing in hydrogen while there were no significant changes in optical properties.

Common among the annealing methods used in the above-mentioned studies is that there were done under isothermal conditions i.e., the temperature remained constant during annealing. However, annealing can also be done under non-isothermal conditions, as is the case when a laser is used to anneal a sample.

This chapter therefore, gives a general introduction and background to the study of this thesis. A brief introduction to thin film technology and application of thin films is given. This is followed by methods that can be used to fabricate thin films and techniques used for characterization of thin films. The problem or knowledge gap that this thesis seeks to address is identified, and the aims and objectives of the study are defined. Finally, the layout of the thesis is given.

1.1 Thin Films Technology

Thin films are a class of materials that have a thickness in a range of a few nanometres to several micrometres [1.6]. Thin film technology has been an active area of research, with bi-metallic layers, semiconductors and insulators being of particular interest [1.7]. Several cutting-edge technologies including superconducting technology, storage technology and the emerging 5G network technology have some form of thin film coating in them [1.6]. Research in thin films has had a profound impact on health, energy, and general human progress. The

societal benefits of thin films have seen their application in reflectors, fluorescent screens, integrated circuits, and micro-electronics among other areas [1.7].

When materials are fabricated with their dimension reduced to nanometre, or to a few microns (*thin films*), it has been observed that this can alter the physical properties of that material. This can lead to improved transmission, reflection, absorption or electronic properties of that material. The abrasion resistance of alloys can also be modified, and the electrical behaviour of material can also be enhanced [1.8]. Thin films have also had a huge economic impact for many years, for an example, the market value of semiconductor devices exceeded $515 billion in 2019 [1.9].

Much of the progress in the field of thin film technology has been driven by advances made in the methods that can be used to deposit thin films [1.8]. These methods include physical vapour deposition (PVD) and chemical vapour deposition (CVD), with methods like sputtering and electron beam (*e-beam*) becoming increasingly important. Also contributing to progress in thin film research is the availability of vacuum technology. Carrying deposition under vacuum has several advantages which includes the fact that films of high purity are produced, and properties of thin films are reproducible [1.10]. Furthermore, carrying deposition under vacuum also reduce the risk of the growing thin film from undergoing oxidation.

1.2 Preparation of Thin Films

There are several methods that can be used for the fabrication of thin films [1.7]. These methods can be divided into two broad categories which are chemical vapour deposition (CVD) and physical vapour deposition (PVD) methods respectively [1.8]. CVD methods involves the reaction of volatile compounds generally in a gaseous state. The reaction of gases is activated by thermal energy, resulting in a non-volatile continuous solid thin film being deposited on a substrate [1.11]. There has been an increased interest in CVD method because it can be used to produce a variety of thin films of high purity on large surfaces. Figure 1.1 show a schematic diagram of chemical vapour deposition chamber and its components, during operation.

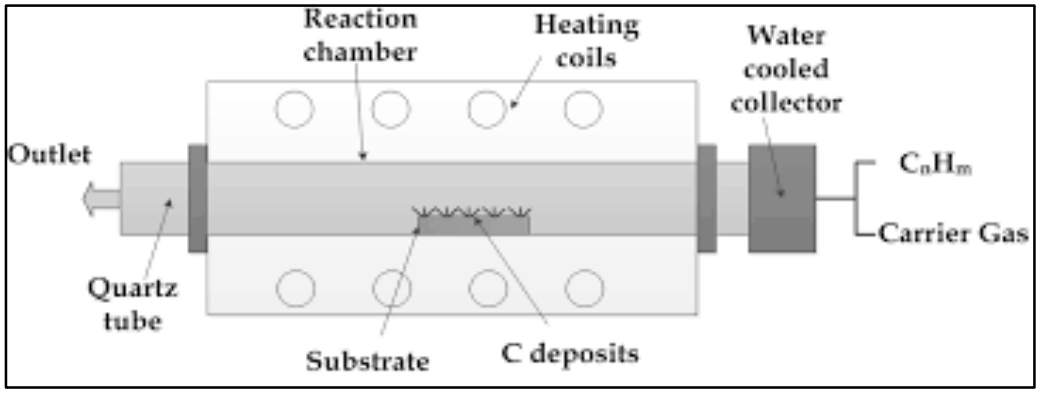

Figure 1.1: *Schematic of CVD chamber showing all the components [1.12].*

CVD process is also a popular deposition method because it allows for controllable deposition of thin films with varying stoichiometry by proper adjustment of deposition conditions [1.11]. There are several types of CVD that have been developed over the years, with Atmospheric Pressure CVD, Low-pressure CVD, Hot-Wire CVD, and Plasma Enhanced CVD being amongst the popular ones [1.8].

In Atmospheric Pressure CVD, the reaction process takes place in reaction chamber which is at atmospheric pressure. This eliminate the need for the use of vacuum technology and associated accessories, and as a result, it is cheaper to operate and to maintain. One major disadvantage of Atmospheric Pressure CVD is that oxygen from the atmosphere can be adsorbed by the growing thin film. This is a major challenge especially when depositing material that oxidizes easily. Low-pressure CVD is a method that is similar to Atmospheric pressure CVD. The only difference is that the whole chamber is under high vacuum pressure. Figure 1.2 shows a typical set for a Low-pressure CVD.

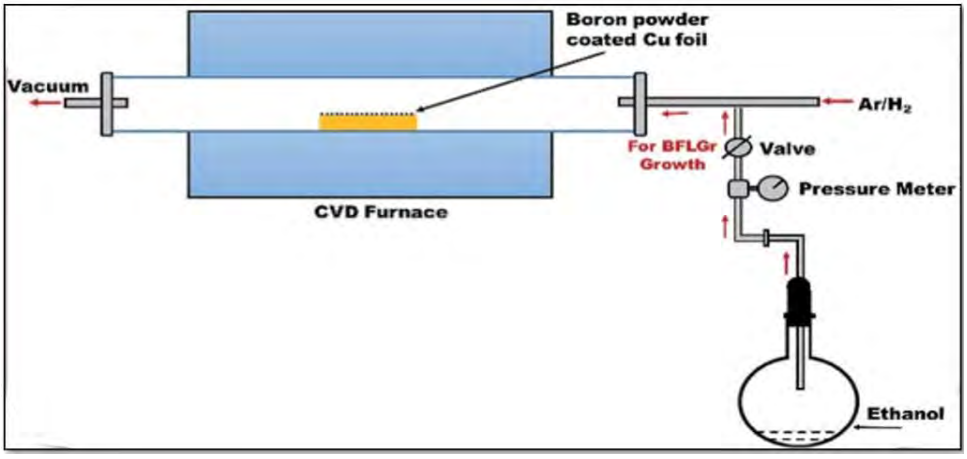

Figure 1.2: *Typical set-up of a Low-Pressure CVD for thin film deposition [1.13].*

In Hot-Wire CVD, deposition is carried out under high vacuum therefore, the problem of oxidation that is associated with Atmospheric Pressure CVD is eliminated. This method makes use of a hot wire made of a refractory metal for example Tungsten or Tantalum [1.11]. The wire acts as a pyrolytic catalyst to break organic and inorganic gases. These gases react and result in the formation of a thin homogenous layer on a substrate. Hot-Wire CVD can also be used to deposit metals. A typical set up of Hot-Wire CVD and related accessories is shown in figure 1.3.

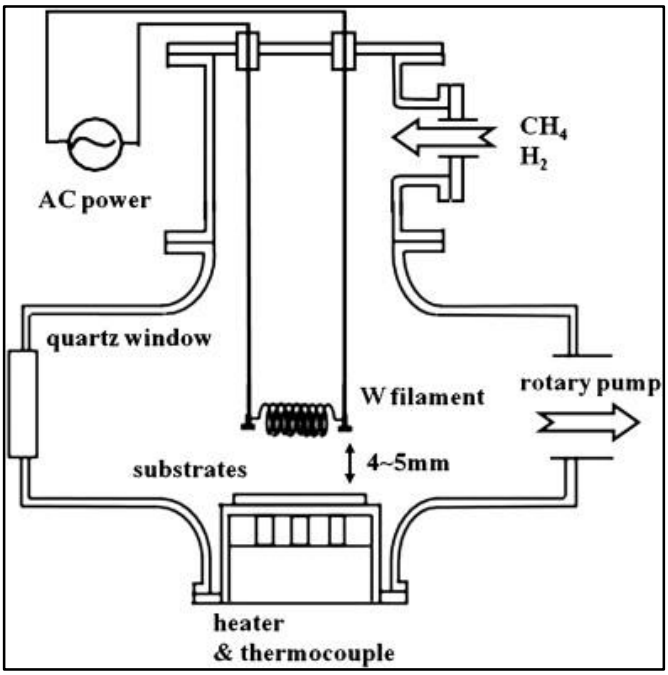

Figure 1.3: *Hot-Wire CVD reaction chamber and its operational components [1.14].*

A major advantage of CVD is that deposition can be done at easily controllable physical parameters for example low temperature, low pressure or high pressure, etc. [1.10]. It is also an uncomplicated and economically competitive process. The disadvantage of CVD is that chemical precursors with high vapour pressure and high volatility when exposed to air are required [1.15]. The by-products of CVD can at times be toxic and corrosive, and as a result might require neutralization after the process [1.15].

PVD methods on the other hand entails the transfer of atoms from a source material to a substrate where the growth of the thin film occurs. An example of a PVD technique is electron beam deposition (*e-beam*) which is a technique that was used in this study and details of which are given in **Chapter 3**. This type of PVD involves the transfer of atoms from the target material by thermionic electrons to deposit them on a substrate. Thermionic electrons from a

resistively heated tungsten filament are used to heat a solid target material. These electrons are emitted from the surface of a resistively heated filament (*by applying high potential difference*). Electromagnetic field and a spray shield are used to focus electron beam onto the target material in the water-cooled crucible. Depending on the physical properties of the target, the material can either melt, then evaporate or directly sublimate when heated by thermionic electrons. The evaporated or sublimated atoms travel to the substrate, and when the atoms are on the substrate, they find energetically favourable sites before condensing. This will result in agglomeration and coalescence of atoms resulting in a smooth continuous thin film [1.16]. The major advantages of this method are high deposition rate and good vacuum which allows for the growth of film to occur in a clean environment [1.11].

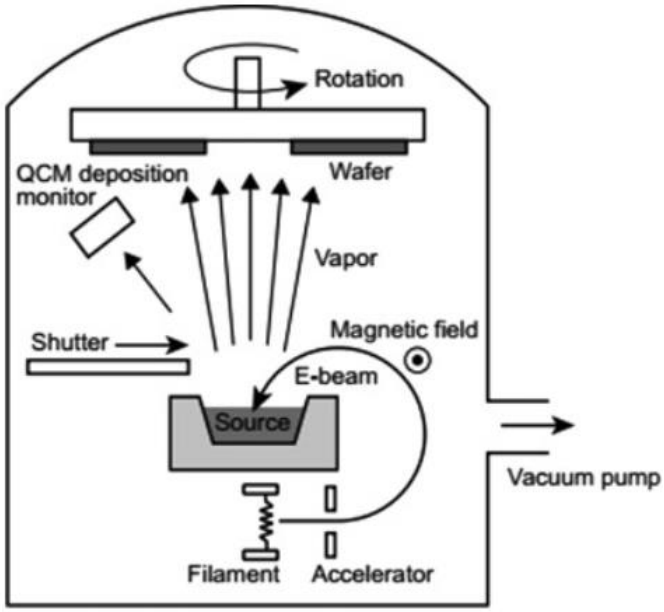

Figure 1.4: *Schematic diagram of electron beam evaporation system [1.11].*

Another example of PVD method is sputtering. Sputtering involves the ejection of atoms from a target material by bombarding it with energetic ions and thereafter the ejected atoms are accelerated to the substrate where they are deposited. The process of sputtering involves the introduction of argon (Ar) gas into the sputtering chamber. The Ar is then ionised by electric field to produce Ar^+ which is then used to bombard the target. Sputtering can be operated in 2 modes i.e., direct current (DC) sputtering also known as diode sputtering and radiofrequency (RF) mode. Figure 1.5 show an experimental set-up of the sputtering machine.

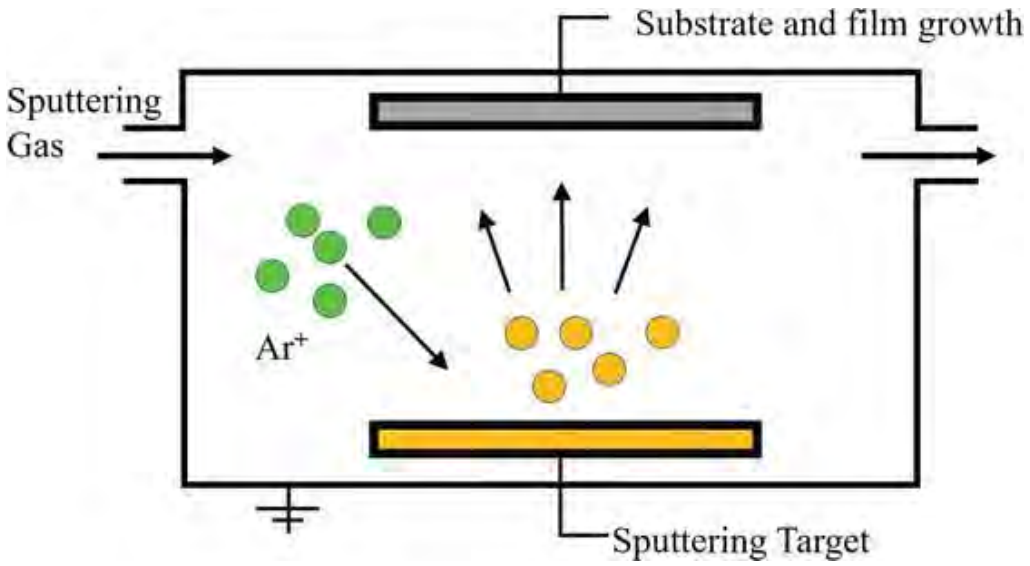

***Figure 1.5**: Schematic diagram of a sputtering chamber with argon ionized atoms [1.17].*

RF mode is used for the sputtering of insulating material. The advantage of RF mode is that high voltage can be applied to target material without discharge occurring. The disadvantage of RF mode is that it has a low deposition rate. DC sputtering on the other hand is used for the sputtering of conductive material. This mode consists of two electrodes i.e., cathode (*target material*) and anode (*substrate*). The advantage of this mode is that it has a high deposition rate. Furthermore, this mode requires low temperature and does not produce toxic products, as is the case with CVD.

Thermal evaporation is another popular PVD method for growing thin films. In this method, deposition in carried out under vacuum with the metal to be deposited placed in a refractory metal boat. High potential difference is then applied on either ends of the boat.As the boat temperature is raised due to resistive heating, the contents of the boat starts to melt and evaporate. The disadvantage of this method is that it is difficult to produce high purity thin films because some metal tends to react with the boat resulting in the formation of an alloy. Figure 1.6 show a typical thermal evaporation experimental set-up.

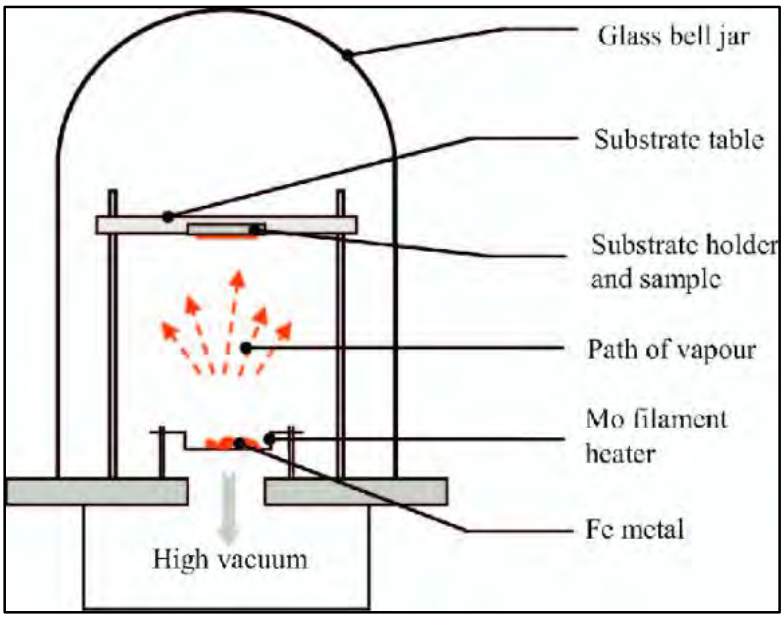

Figure 1.6: *Typical set-up of a thermal evaporation experimental chamber [1.18].*

1.3 Thin film growth mechanism

The type of deposition method that is used for thin film deposition depends on the desired material characteristics [1.19]. A general mechanism that describes thin film growth can be explained from the interaction of the atoms/molecules as soon as they reach the substrate. One of three things can happen to atoms that reach the substrate from the target material (*generally in a gaseous state*). The atoms can be reflected by the substrate, absorbed to the substrate, or penetrate the substrate. The atoms that are adsorbed to the substrate tend to find energetically favourable sites and bond to the substrate. When other incident atoms interact with these atoms, they will nucleate and coalesce, and turn into bigger footprint on the surface, resulting in the formation of a thin film on the substrate. Figure 1.7 shows a general schematic representation of the film growth process.

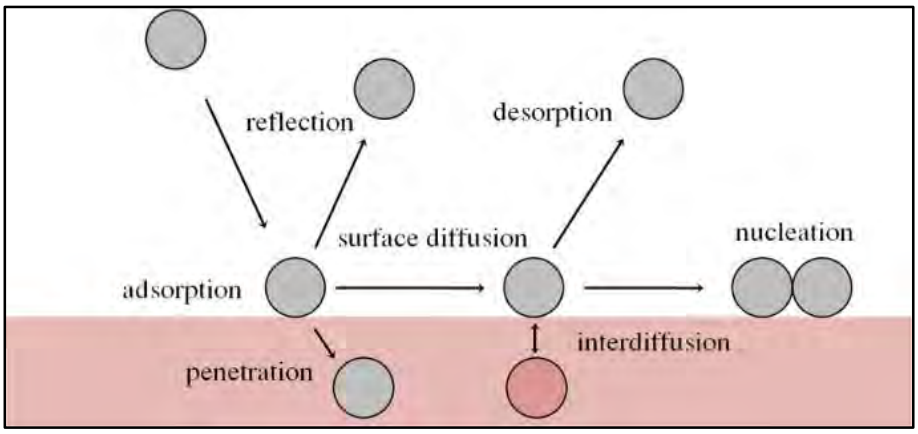

Figure 1.7: *Representation of a general process of thin film growth on a substrate [1.20].*

Regardless of the deposition method used, the specific growth mechanism of thin films can be classified into one of three modes i.e., *Volmer-Weber (V-W)* [1.21], *Frank-Vander Merwe (FM)* [1.22] or *Stranski-Krastanove (S-K)* [1.23]. The surface morphology of the growing film is generally tied to the growth mechanism.

Volmer-Weber, also known as island growth, is the dominant growth mechanism in systems of metals on insulators, graphite, and mica substrate [1.11]. This mode occurs in cases where atoms bound strongly to each other than to the substrate resulting in the formation of islands that grow in 3 dimensions. Figure 1.8 shows the schematic representation of Volmer-Weber growth mode. Volmer-Weber mode result in the formation of rough multi-layer film on the substrate.

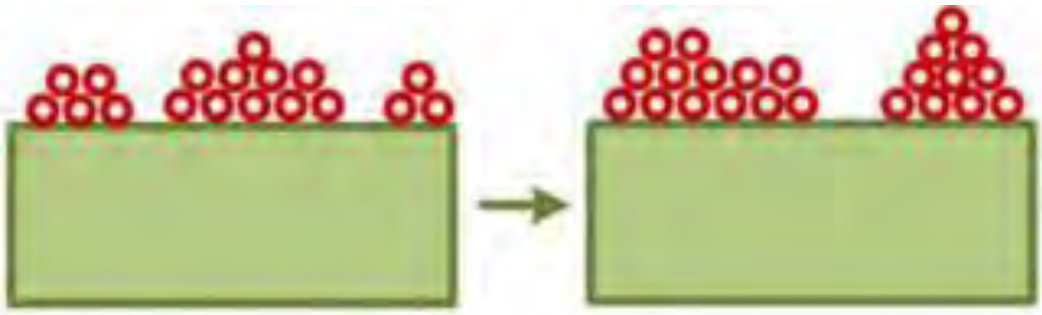

Figure 1.8: *Schematic diagram of Volmer-Weber growth mode [1.24].*

A growth mechanism that is preferred in the thin films of electronic devices is layer-by layer growth, also known as Frank-Vander Merwe. The evidence of this growth mechanism is the occurrence of 2-dimensional continuous film and result in the formation of planar sheets [1.11].

This occurs in circumstances where the atoms bound more strongly to the substrate than to each other. This growth pattern commonly occurs in single crystal epitaxial of semi-conductors [1.11]. As can be seen in figure 1.9, atoms attach themselves to surface sites and this result in the formation of smooth layer of film.

Figure 1.9: *Schematic diagram of Frank-van der Merwe growth mode [1.24].*

Stranski-Krastanove is a combination of both island growth and layer growth. This is common in metal-metal systems and metal semi-conductor systems. This mode starts with the formation of a complete film of up to several monolayers thickness in a layer-by-layer fashion [1.23]. The thickness that is deposited in a layer-by-layer fashion depends on the strain and the chemical potential of the deposited film. Once this critical thickness has been reached, growth then proceeds via nucleation and coalescence of islands [1.23] as shown in figure 1.10.

Figure 1.10: *Schematic diagram of Stranski-Krastanov growth mode [1.24].*

1.4 Characterisation of thin Films

Several different techniques can be used to characterize thin films. Initially, the characterisation of thin films focused on thickness determination and the determination of optical properties [1.11]. This was because thin films were used mainly for optical applications. However, with an increase in the areas of application and especially in microelectronics, more characterization techniques were developed.

Currently, characterization techniques include those that are used to determine thickness, morphology, structure, as well as chemical composition. Common among all these techniques is their use of electrons, ions, or photons [1.11]. These interact with the surface of a thin film such that secondary electrons or ions are emitted which carry information about chemical or structural composition of the thin film.

The determination of thickness of thin films is important because the behaviour and properties of thin films are affected by the thickness. Several techniques can be used to determine the thickness of thin films. These can be destructive or non-destructive techniques. Some of these techniques for example, Fringes of equal thickness (FET), rely on optical measurements to determine thickness [1.11]. These are highly accurate techniques that are based on the interference of two or more beams of light. The optical length difference of these light beams can be related to the thickness of the thin film. Others like Stylus-method profilometry and crystal oscillators are mechanical in nature. Only a limited number of techniques can be used to measure the thickness of the film as it is growing, most of these measures the thickness once the film has been grown.

Structural information of interest can be obtained by using a variety of techniques. These range from those that provide information about surface topography and morphology to those that provide information about grain size. Examples of techniques that provide structural information include scanning electron microscopy (SEM), transmission electron microscopy (TEM) and x-ray diffraction (XRD). Both SEM and XRD which were used in this study are dealt with in detail in **Chapter 3**. Chemical composition of a thin film is also important in determining the behaviour of thin film. Energy dispersive x-ray (EDX), Auger electron spectroscopy (AES) and Rutherford backscattering spectrometry (RBS) are some of the techniques that can be used to determine chemical composition of a thin film. A variant of RBS, *real-time* RBS, has the added advantage of following the reaction in real time, this technique was used in this study and is dealt with in detail in **Chapter 3**.

1.4 Problem statement

Soldering alloys are used to join an array of semiconductor chips in device fabrication [1.25]. Lead (Pb) and Pb containing alloys have been the soldering alloys of choice over the years because of their excellent electrical and mechanical properties [1.26]. However, due to the toxicity of Pb, many countries have banned the use of Pb and Pb containing products. As a result, considerable effort has been put into finding Pb free soldering alloys. Zinc-Tin (Zn-Sn) alloy has come up as a top contender for replacing Pb containing soldering alloys.

When a bilayer of Zinc (Zn) and Tin (Sn) is annealed, a Zn-Sn alloy is formed. Several studies looking at different aspects of this alloy have been conducted in the past. Jiang et al. [1.27] for example, studied the oxidation behaviour of this alloy at high temperature and high humidity. In this study, samples of Zn-Sn alloys were exposed to a constant temperature of 85 °C and relative humidity of 43 %, 64 % and 85 % respectively. The samples were then characterised with a variety of techniques to ascertain microstructure, phase evolution and to identify phases that were present. The techniques used included scanning electron microscopy (SEM), electron probe micro-analysis, electron backscattering diffraction and energy dispersive x-ray spectrometry. The results showed an increase in the rate of oxidation with an increase in relative humidity. This was attributed to diffusion of Zn along the grain boundaries and the subsequent formation of ZnO.

Lee et al. [1.28] made use of Radio-frequency co-sputtering to fabricate Zn-Sn thin films to study the morphology and conductivity of Zn-Sn. The sputtering was carried out in ultrahigh vacuum in which a temperature of 293 K was maintained. Thin films of different thicknesses where deposited. Four-point probe, X-Ray Photoelectron Spectroscopy (XPS), XRD, AFM and SEM were used respectively to determine oxidation state, electrical, crystallinity and morphological properties of the thin films respectively. The results showed that a higher portion of Zn is oxidised than Sn, this is due to the difference in standard reduction potential between Zn and Sn. It was also concluded that as the thickness of the thin film increase the conductivity also increased. Furthermore, x-ray diffraction (XRD) showed improvement in the crystallinity of Zn-Sn film compared to that monometallic thin film.

Two common treads stand out from the studies mentioned above. Firstly, the annealing of the samples was done by conversional method and can be said to be isothermal. Secondly, the characterisation of the samples was done *ex-situ*. Ex-situ characterisation generally suffers from lack of reproducibility of experimental conditions and sample quality.

An unconventional way of annealing a sample is by using a laser. While annealing in the studied above could be termed isothermal, laser annealing could be said to be non-isothermal. Non-isothermal annealing leads to the formation of out of thermodynamic equilibrium phases [1.29]. Several studies have been conducted that used laser annealing and resulted in the formation of out of thermodynamic equilibrium phases.

Weber et al. [1.30] used electron beam evaporator (*e-beam*) to deposit iron (Fe) and silicon (Si) respectively on amorphous silicon (*a-Si*). The thin films were annealed with nano-second laser of different energy densities to investigate the formation of non-equilibrium epitaxial silicide. Rutherford backscattering spectrometry (RBS) and Transmission electron microscopy (TEM) were used to study the films. Complete epitaxial layer of non-equilibrium Ni and Fe silicide phases were found. Upon annealing, the non-equilibrium phases decayed into equilibrium phases.

Comrie et al. [1.31] studied the formation of metastable iron silicide phase by pulse laser annealing. Previous studies showed that during the growth of iron silicide there is a competition between stable phases (ε-FeSi,α-$FeSi_2$ and β-$FeSi_2$) and metastable phases ([CsCl]FeSi,γ-$FeSi_2$) [1.31]. Iron silicide thin films were produced by the deposition of Fe on Si<111> substrate under high vacuum after which the films were annealed at 450 °C. The films were then irradiated with a pulse excimer laser with energy density that ranged between 0.30 - 0.90 J/cm^2 in order to study phase formation and crystallization of metastable phases. The samples were then characterized with Rutherford backscattering spectroscopy (RBS), channelling spectrometry and cross-sectional transmission electron microscopy. The results showed that it was possible to form metastable phases of ε-FeSi by pulsed laser annealing.

Rutherford backscattering spectrometry (RBS) is a technique that is commonly used to study composition, thickness, and depth profile in thin films [1.32]. In conventional RBS, samples are annealed in sequence and thereafter analysed to study solid phase reaction evolution. This approach is therefore prone to problems for example variation in samples and reproducibility of experimental conditions. Furthermore, conventional RBS requires more samples which leads to wastage of material. In situ real-time RBS, details of which are given in **Chapter 3**, is a variant of RBS that can eliminate the challenges associated with conventional RBS. This essentially eliminates the problems of conventional RBS by allowing the use of a single sample to monitor the evolution of solid phase reaction in real-time while annealing.

There is a general lack in literature of studies that combine *in-situ*, real time RBS and non-isothermal annealing despite the benefits of *in-situ* analysis alluded to above. This study therefore seeks to fill this gap in literature. In this study, an unconventional annealing method is used to anneal Zn-Sn thin film. A 1064 nm femtosecond laser is used to anneal the samples. Furthermore, the reaction is monitored in real time with *in-situ* Rutherford backscattering spectrometry (RBS) which minimise the problems associated with *ex-situ* characterization.

1.5 Aim and Objectives

The aims and objectives of this study are therefore to:

- Synthesis Zn-Sn thin films with electron beam evaporator (*e-beam*).
- Characterize the thin films with x-ray diffraction (XRD), Scanning Electron Microscopy (SEM), Atomic Force Microscopy (AFM) and Rutherford backscattering Spectrometry (RBS).
- Vacuum anneal (*isothermal annealing*) the thin films and characterize them post annealing.
- Anneal the thin films with femtosecond laser (*non-isothermal annealing*) while tracking the evolution of the reaction with real time RBS.
- Compare the results of vacuum annealed (*isothermal annealing*) thin films to those of laser annealed (*non-isothermal annealing*) samples.

1.6 Thesis outline

This thesis consists of 5 chapters.

Chapter 1: This chapter gives a general introduction to the study of this thesis. Key principles that will be encountered in subsequent chapters of this thesis are introduced. Finally, aims and objectives of the study are defined.

Chapter 2: In this chapter, a review of literature of the subject of this study is presented. The review covers soldering, material that can be used for soldering and properties thereof. This is followed by a detailed review of the Zn-Sn alloy system as a potential replacement for lead based alloys for high temperature application. RBS and it variant i.e., *in situ* RBS are

introduced together with laser. The interaction of matter with laser is also reviewed by looking at studies that used laser to anneal samples.

Chapter 3: This chapter focuses on the theoretical basis upon which the experimental and characterisation techniques used in this study are built upon. The theory of each technique is followed by a detailed experimental setup for each experiment.

Chapter 4: In this chapter, experimental results obtained during this study are presented and discussed. Both imperial and analytical methods are used in the discussion of the results.

Chapter 5: This chapter gives the summary and conclusion from this study. Suggestions about possible future work is also given in this chapter.

1.7 References

[1.1] Oh-Ishi, K., Edalati, K., Kim, H.S., Hono, K. and Horita, Z., 2013. High-pressure torsion for enhanced atomic diffusion and promoting solid-state reactions in the aluminum–copper system. Acta Materialia, 61(9), pp.3482-3489.

[1.2] Ditchfield, R., Llera-Rodriguez, D. and Seebauer, E.G., 1998. Nonthermal effects of photon illumination on surface diffusion. Physical review letters, 81(6), p.1259.

[1.3] Allen, C.E., Ditchfield, R. and Seebauer, E.G., 1996. Surface diffusion of In on Si (111): Evidence for surface ionization effects. Journal of Vacuum Science & Technology A: Vacuum, Surfaces, and Films, 14(1), pp.22-29.

[1.4] Zulkifli, Z., Sharma, S., Shinde, S., Kalita, G. and Tanemura, M., 2015. Effect of annealing in hydrogen atmosphere on ZnO films for field emission display. In IOP Conference Series: Materials Science and Engineering (Vol. 99, No. 1, p. 012030). IOP Publishing.

[1.5] Hakeem, A., Ramzan, M., Ahmed, E., Rana, A.M., Khalid, N.R., Niaz, N.A., Shakoor, A., Ali, S., Asghar, U. and Nadeem, M.Y., 2015. Effects of vacuum annealing on surface and optical constants of hafnium oxide thin films. Materials Science in Semiconductor Processing, 30, pp.98-103.

[1.6] Mbam, S.O., Nwonu, S.E., Orelaja, O.A., Nwigwe, U.S. and Gou, X.F., 2019. Thin-film coating; historical evolution, conventional deposition technologies, stress-state micro/nano-level measurement/models and prospects projection: a critical review. Materials Research Express, 6(12), p.122001.

[1.7] Maissel, L.and Clang, R.1970. Handbook of Thin Film Technology. New York: McGraw.

[1.8] Seshan, K., 2001. Handbook of thin film deposition processes and techniques. William Andrew.

[1.9] Deloitte, Semi-conductors-the Next wave, Opportunities and winning strategies for semiconductor companies, April 2019.

[1.10] Frey, H. and Khan, H.R. eds., 2015. Handbook of thin film technology. Berlin: Springer. Berlin: Springer.

[1.11] Ohring, M., 1992. Shikimic The Material Science of Thin Films. California: Academic Press.

[1.12] Lin, Y. ed., 2016. Advanced nano deposition methods. John Wiley & Sons.

[1.13] Srivastava, S., Jain, S.K., Gupta, G., Senguttuvan, T.D. and Gupta, B.K., 2020. Boron-doped few-layer graphene nanosheet gas sensor for enhanced ammonia sensing at room temperature. RSC Advances, 10(2), pp.1007-1014.

[1.14] Ashfold, M.N., May, P.W., Petherbridge, J.R., Rosser, K.N., Smith, J.A., Mankelevich, Y.A. and Suetin, N.V., 2001. Unravelling aspects of the gas phase chemistry involved in diamond chemical vapour deposition. Physical chemistry chemical physics, 3(17), pp.3471-3485.

[1.15] Pierson, H.O., 1999. Handbook of chemical vapor deposition: principles, technology, and applications. William Andrew.

[1.16] Döpp, C., Design Modifications of a High Vacuum Unit for Thin Film Formation by Electron Beam Evaporation. Diploma Thesis, Savonia University of Applied Science (2007).

[1.17] Shi, F., 2018. Introductory Chapter: Basic Theory of Magnetron Sputtering. In Magnetron Sputtering. IntechOpen.

[1.18] Martín-Palma, R.J. and Lakhtakia, A., 2013. Vapor-deposition techniques. In Engineered Biomimicry (pp. 383-398). Elsevier Inc.

[1.19] Bunshah, R.F., 1982. Deposition technologies for films and coatings. New Jersey: Noyes Publication.

[1.20] Chouhan, A.S., 2017. Tuning of Magnetic and Electrical Properties in Complex oxide Thin Films Deposited by Pulsed Laser Deposition. ArXiv preprint arXiv: 1705.11003.

[1.21] Oura, K., Lifshits, V.G., Saranin, A.A., Zotov, A.V. and Katayama, M., Surface Science: An Introduction. 2003. Berlin: Springer.

[1.22] Pimpinelli, A. and Villain, J., 1999. Physics of crystal growth (p. 400). Cambridge: Cambridge University Press.

[1.23] Venables, J., 2000. Introduction to surface and thin film processes. Cambridge University Press.

[1.24] Kunar, C., Synthesis of strongly correlated oxides and investigation of their electrical and optical properties. PhD Thesis, Luxembourg Institute of Science and Technology (2017).

[1.25] Yeh, C.H., Chang, L.S. and Straumal, B., 2010. Wetting transition of grain boundaries in tin–rich indium-based alloys and its influence on electrical properties. Materials transactions, 51(9), pp.1677-1682.

[1.26] Wang, C.H., Chen, H.H. and Li, P.Y., 2012. Interfacial reactions of high-temperature Zn–Sn solders with Ni substrate. Materials Chemistry and Physics, 136(2-3), pp.325-333.

[1.27] Jiang, J., Lee, J.E., Kim, K.S. and Suganuma, K., 2008. Oxidation behaviour of Sn–Zn solders under high-temperature and high-humidity conditions. Journal of alloys and compounds, 462(1-2), pp.244-251.

[1.28] Lee, S., Park, J., Kang, Y., Choi, A. and Kang, Y.C., 2017. Spectroscopic and morphological investigation of ZnSn thin films obtained by radio frequency cosputtering. Bulletin of the Korean Chemical Society, 38(11), pp.1340-1346.

[1.29] Von der Linde, D., Sokolowski-Tinten, K. and Bialkowski, J., 1997. Laser–solid interaction in the femtosecond time regime. Applied Surface Science, 109, pp.1-10.

[1.30] Weber, B., Gärtner, K., Witzmann, A., Kaschner, C. and Kasko, I., 1992. Non-equilibrium epitaxial silicides-a special effect of silicide formation by ns-laser irradiation. Applied surface science, 54, pp.381-385.

[1.31] Comrie, C.M., Falepin, A., Richard, O., Bender, H. and Vantomme, A., 2004. Metastable iron silicide phase formation by pulsed laser annealing. Journal of applied physics, 95(5), pp.2365-2370.

[1.32] Wang, Y.Q. and Nastasi, M., 2009. Handbook of modern ion beam materials analysis, chaps. 5 and 6. Warrendale, PA: Materials Research Society Publisher.

CHAPTER 2

Literature review

2. Background

In this chapter, an in-depth literature review of the subject of this study is presented. As stated in **Chapter 1**, the overall aim of this study was to compare isothermal (*constant thermal annealing*) and non-isothermal *(pulsed laser annealing*) annealing of Zinc-Tin (Zn-Sn) metallic bilayer using *in-situ* Rutherford backscattering spectrometry (RBS) as a major probing tool. Other complimentary characterization techniques were used to have a comprehensive analysis of the samples.

The Zn-Sn system is particularly suitable for use in soldering application, for example in electronic and automobile industries. This literature review will therefore focus on various alloys that can be used in soldering, advantages and disadvantage of these alloys, and their properties. Focus will be given to lead (Pb) containing alloys and the problems that these Pb containing alloys present from an environmental and health point of view. This will be followed by consideration of Pb free alternatives including Zn-Sn system which is the major focus of this study. The Zn-Sn system will be looked at in terms of physical properties, applications as well as what has been studied previously (*state of the art*). A brief introduction to RBS and it variant, *in situ* RBS, will be presented, this technique will be presented in fuller detail in **Chapter 3**. This will be followed by looking at the interaction of laser with matter and a brief introduction to femtosecond laser. A more detailed look at femtosecond laser is given in **Chapter 3**.

2.1 Introduction to soldering

Soldering is a process that is used to join 2 or more metals together by melting a filler metal (*solder*) between them. When the solder cools, a permanent joint between the metals is formed. The process of soldering is different from welding in that with welding, the metals that are to be joined need to melt, while that is not the case with soldering. It is only the soldering alloy that melt, and the alloy usually has a relatively low melting temperature, generally less than 450 °C [2.1].

The process of soldering is used in the electronic industry to provide interconnection between the electronic components and the substrate [2.2]. These interconnections must have both good conductivity and mechanical strength. Solders are also used in optical device packaging, die attach and bonding of semiconductor devices [2.3]. There are many different types of soldering alloys available for different applications. By far the most common soldering alloys are those that are based on tin (Sn) for example, tin-lead (Sn-Pb), tin-zinc (Zn-Sn), tin-copper (Sn-Cu), tin-bismuth (Sn-Bi) and tin-silver (Sn-Ag) [2.4].

2.2 Properties of a good soldering alloy

The required properties of a soldering alloy depend largely on it application and on the conditions in which the material being joined will be exposed to. For example, the properties of a soldering alloy used to join material that will be exposed to high humidity, will be different from a soldering alloy for materials that will be exposed to a dry, low temperature environment. In general, a good soldering alloy should have most of the following properties [2.4]:

- Good mechanical properties.
- Fatigue resistance and good wettability.
- Low rate of formation of intermetallic compounds (IMC).
- Melting temperature must be suitable for service temperature range.
- Cheap and environmentally friendly.

In practice however, it is almost impossible to find an alloy that meet all these criteria all the time. It is therefore important to determine which of these properties are the most important for a particular application and to choose a soldering alloy that meet those requirements.

2.3 High temperature soldering alloys

High temperature solders are used as die-attach solders in automobile circuit boards [2.5] and bonding semi-conductor device to substrate [2.6]. The automotive, aerospace, and avionic industries are among the industries that have led to an increase in the use of high temperature solders [2.7]. Alloys that are used as high temperature solders should have the following properties [2.8]:

- Melting temperature of between 260 – 400 °C.
- Good electrical and thermal conductivity.
- Good mechanical properties, especially fatigue resistance.
- Excellent wettability.

For decades, alloys that have been used as high temperature solders have been high Pb bearing alloys such as Pb-Sn, Pb-Ag [2.8]. These alloys have been mostly used for packaging of electronic components and devices [2.9]. Lead based alloys have been used because they are cheap, have good mechanical properties and because of their excellent wetting behaviour. In the Sn-37Pb system for example, Pb reduces the surface tension of Sn thereby improving the wetting behaviour of the alloy [2.10]. It further prevents the transformation of β-Sn phase to α-Sn phase [2.10]. If this transformation were to occur, it could lead to an increase in volume which will eventually lead to structural integrity of the alloy being compromised [2.11].

While these Pb based alloys have been used for a long time, their continued used has come under scrutiny from the Environmental Protection Agency (EPA) and other environmental agencies. This is because Pb is listed as one of the most hazardous chemicals, with serious health and environmental consequences [2.12]. Acute exposure to Pb can lead to vomiting, convulsions, and abdominal pain, while prolonged exposure can lead to liver and kidney failure [2.13]. Other studies have shown that exposure during pregnancy could lead to miscarriages [2.14]. As a result of these health challenges, some countries have put a ban on the use of Pb and Pb containing consumer products [2.13].

As a result of the challenges associated with Pb based alloys, there has been considerable effort put into finding Pb free soldering alloys, especially for high temperature application purposes. Several research groups have studied different alloys as potential replacement for Pb containing alloys for high temperature application with varying degrees of successes. These alloys include Au-Sn, Zn-Al, Au-Ge, Bi-Ag and Sn-Zn [2.15]. Further examples of other possible Pb-free

binary alloys are shown in table 2.1. These Pb free solders are not without their own challenges. For example, the melting temperature for Ag, Cu and Zn are 961 °C, 1083 °C and 420 °C, respectively. These temperatures are significantly higher than that of Pb which is 327 °C and as a result, a higher temperature is needed when soldering with these Pb free alloys. On the other hand, the use of Au and Bi based alloys has been limited by costs, poor mechanical properties as well as the formation of intermetallic compounds with different eutectic temperatures [2.15].

Table 2.1: *Other possible Pb-free binary alloys systems.*

System	Composition	Melting temperature (˚C)
Sn-Ag	96.5/3.5Ag	221
Sn-Sb	95Sn/5Sb	232-240
Sn-Bi	58Bi/42Sn	138
Sn-In	48Sn/52In	120
Sn-Cu	99.3Sn/0.7Cu	227

2.4 Lead free alloying systems overview

As stated in the previous section, several alloying systems have been fabricated to study their suitability as Pb free soldering alloys. A study of Sn-Ag alloys was conducted by Osorio et.al [2.16]. In this study, samples of Sn-Ag were prepared by casting (*high purity*) Sn and Ag from molten elements. The weight composition of starting elements were Sn-2 wt. % Ag and Sn-3.5 wt. % Ag, respectively. After annealing the samples, it was observed that there were areas with light streaks and dark streaks. The percentage of the loaded Ag in the Sn in the light streak area was 0.05 wt. % Ag and the dark area had 3.5 wt. % Ag. The eutectic was reported to be formed by a cooperative's growth of Ag_3Sn intermetallic of estimated 73 wt. % Ag. This was as expected based on the phase diagram of the Sn-Ag system in figure 2.1 below.

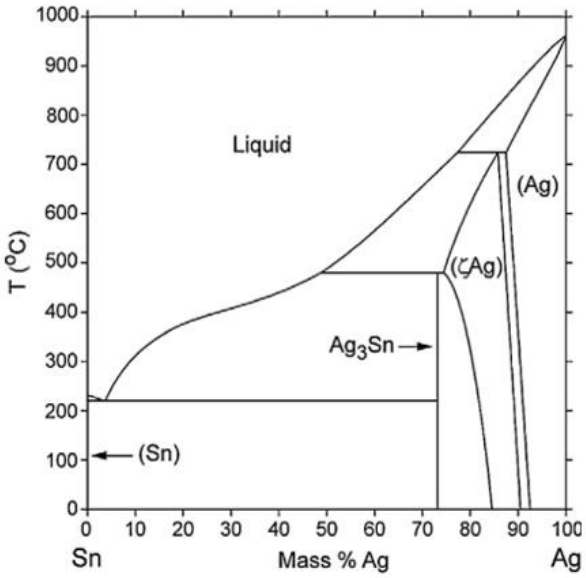

Figure 2.1: *Phase diagram of Sn-Ag system showing predicted phases and stoichiometry [2.17].*

The other system that has been explored is the Sn-Sb alloy system. Samples of Sn-Sb were prepared using high purity Sn and Sb. These were placed in quartz tube and heated into a molt at 1000 ºC and subsequently quenched to form a solid pellet alloy. The microstructure was studied with x-ray diffractometer (XRD). The XRD results showed the existence of Sn_2Sb_3 and β-SnSb. A drawback of this system is that it tends to be difficult to separate or distinguish different phases and different research have diverging views on the phase diagram of the Sn-Sb alloy. A typically the phase diagram of Sn-Sb is as shown in figure 2.2.

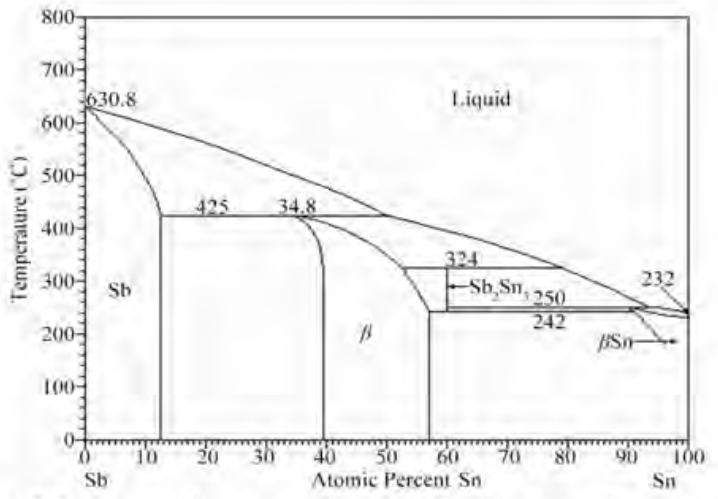

Figure 2.2: *A typical representation of Sn-Sb phase diagram [2.18].*

2.5 Phase diagram of Zn-Sn

Zinc (Zn) is a lustrous metal that is diamagnetic with a hexagonal crystal structure. It has a melting point of 419.5 ˚C and a boiling point of 907 ˚C [2.19]. Zinc is malleable in the temperature range between 100 ˚C to 150 ˚C [2.20].

Tin (Sn) is a ductile and malleable metal with a melting point of 231.9 ˚C as can be seen in figure 2.3. There are 2 allotropes of Sn i.e., beta (β) phase, also known as white tin and alpha (α) phase which is also known as grey tin. The beta phase tin is stable between 13 ˚C and 232 ˚C, while the alpha tin is stable below 3 ˚C [2.21].

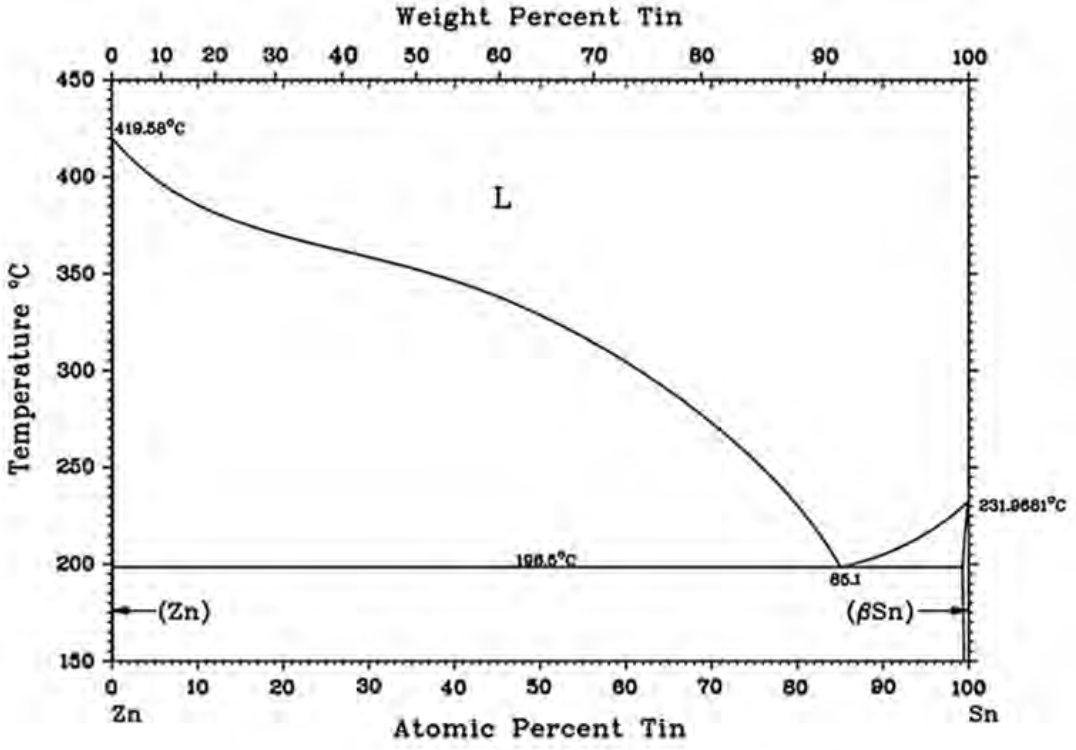

Figure 2.3: *Eutectic phase diagram of Zn-Sn [2.22].*

Figure 2.3 above shows the eutectic phase diagram of Zn-Sn system. The eutectic microstructure consists of phases which are β-Sn phase (body cantered tetragonal) and a hexagonal Zn phase.

2.6 The state of the art of the Zn-Sn bi-metallic system

Several authors have studied different aspects of the Zn-Sn alloy system. Some of these studies have focused on the oxidation behaviour of this alloy, while others focused on the wettability challenge associated with this alloy system. The effect of different alloying elements on the system has also been a subject of study by some authors.

Chen et al. [2.9] studied the effects of adding small alloying elements on the Zn-Sn alloy system. This was done to ascertain the effect of these elements on two of the most important obstacles that have prevented wide scale adaption of this alloy system commercially i.e., oxidation resistance and wettability. Studies have shown that oxidation is major factor behind poor wetting, this is due to the ease with which Zn undergoes oxidation. In this study, Chen et al. [2.9] tested the effect that alloying elements lanthanum (La), titanium (Ti), aluminium (Al) and chromium (Cr) had on oxidation resistance and wetting properties of Zn-Sn. The Zn-Sn alloys were prepared in vacuum quartz tube after which they were homogenized. The alloys where then characterized with inductively coupled plasma atomic emission spectrometry (ICP-AES), scanning electron microscopy (SEM), thermal gravimetric analysis (TGA), x-ray diffraction (XRD) and Auger electron spectroscopy (AES). The study found that the addition of Al, Ti and Cr improved the oxidation resistance of the alloy. The addition of La was found to accelerate oxidation of the alloy.

Jiang et al. [2.23] studied Zn-Sn alloy system under high temperature and high humidity conditions. Furthermore, the study also investigated the mechanism of oxidation in the Zn-Sn alloy as well as the effect of adding bismuth (Bi) as an alloying element. The alloy was exposed to a temperature of 85 °C and different levels of relative humidity, 43 %, 67 % and 85 % respectively. The samples were them characterized with SEM, Electron probe microanalysis and energy dispersive x-ray spectrometry. XRD and electron backscattering diffraction were used to identify the crystallographic phases present. The study concluded that the oxidation of the alloy is due to the oxidation of Zn which diffuses to the Sn grain boundaries and forms ZnO. It was also concluded that the oxidation rate increases with increasing relative humidity. The addition of Bi to the alloy increased the rate of oxidation. The addition of Bi was also found to be responsible for the formation of cracks along the Sn grain boundaries.

While the studies above have focused on the oxidation behaviour of Zn-Sn alloy system, other authors have studied the interfacial properties of Zn-Sn alloy system as a potential high temperature Pb free soldering alloy. Choa-hong et al. [2.16] investigated the interfacial reaction

of Zn-xSn (*x = 20, 30, 40, 50 wt. %)* on a Ni substrate over a range of temperatures, ranging from 380 °C – 420 °C. SEM and optical microscopy were used to characterize the microstructure of the reaction layer. The composition of reaction phase was determined with energy-dispersive X-ray spectrometer. In the reaction that was carried out at a temperature range of 380 °C – 420 °C, γ-Ni_5Zn_{21} phase formed at the interface. When the reaction was carried out at 400 °C and the wt. % of Sn was 20 wt. %, a porous structure of Ni_5Zn_{21} formed and this structure grew rapidly. However, when the wt. % of Sn was greater than 20 % the rate of growth was slow and a denser structure, Ni_5Zn_{21} formed.

Jae-Ean Lee et al. [2.8] conducted a similar study using Zn-xSn (*x = 20, 30 and 40 wt. %*) on a copper (Cu) substrate. In this study, it was found that two reaction layers formed adjacent to the solder and the other facing the Cu substrate, respectively. The layer adjacent to solder consisted of ε-$CuZn_5$ and the layer facing the substrate consisted of γ-Cu_5Zn_8 .The thickness of these layers decreased as a function of Sn.

2.7 Thin film Analysis using Rutherford backscattering spectrometry

Rutherford backscattering spectrometry (RBS) is one of the ion beam analysis techniques that is well suited for the analysis of thin films and multi-layers. It found prominence when it was used to analyse the composition of lunar soil in the 1960s [2.24].The technique has found application in several research fields including physics, biology, and material science.

RBS involves the scattering of energetic alpha particles on the surface of the material that is being analysed. When the alpha particles interact with a target material, the alpha particle penetrates deep into the sample to a depth of up to 10 μm (*depending on the energy of the particles and the scattering angle*) [2.25] and as the alpha particles travel through the material, kinetic energy is lost. Some of the alpha particles collide with the atoms of the target and are backscattered. The mass of the atoms from which the scattering occurred can be determined by measuring the energy that is lost due to scattering.

RBS allows for the determination of elemental composition and depth profiling in thin films, this technique relies upon 3 basic physical principles which are dealt with in detail in **Chapter 3**, these are kinematic factor, energy loss and differential scattering cross section. These principles give the RBS the capability to determine mass, depth resolution and to do quantitative analysis of atomic composition, respectively.

RBS can also be combined with other ion beam analysis techniques should it be necessary, to improve the analysis of the material. For example, Karl et al. [2.26] combined RBS with secondary ion-mass spectrometry (SIMS) to obtain stoichiometric and absolute atomic concentration of buried layer. RBS can also be combined with channelling to obtain information about local structure in crystalline system. Other features that make RBS a powerful technique include [2.27]:

- Allows for quantitative analysis of elements simultaneously.
- Depth resolution of about +/-10 nm.
- Good sensitivity to heavy elements.
- Non-destructive.

One major disadvantage of RBS is its inability to detect light elements for example boron, hydrogen, and lithium [2.25]. This is a major problem since these elements are of great significance in near-surface regions of thin films [2.24]. This problem can be overcomed by depositing the thin film on low atomic mass substrates [2.24]. RBS is also unable to determine crystallographic phases that are present in the sample.

2.8 In situ RBS

Real time RBS is a variant of RBS that complements conventional RBS. Real-time RBS has an advantage over conventional RBS in that it allows for the annealing of a sample while collecting the spectra at pre-determined temperature, and this is done in real time. This gives real-time RBS the ability to analyse a sample while simultaneously subjecting it to thermal annealing to induce solid phase reaction. This approach therefore essentially eliminates the problems that are associated with conventional RBS, for example annealing a series of samples at varying temperature to track the reaction. Doing so might lead to bigger experimental error due to difficulty in reproducing exact experimental conditions. Figure 2.4 (a) and (b) show a typical example of spectra and colour coded contour plot respectively that are typically obtained from real-time RBS. The spectra is from a study by Magogodi et al. [2.27] in which a palladium, titanium, and palladium (Pd/Ti/Pd) multilayer was deposited on Ti substrate to study interdiffusion.

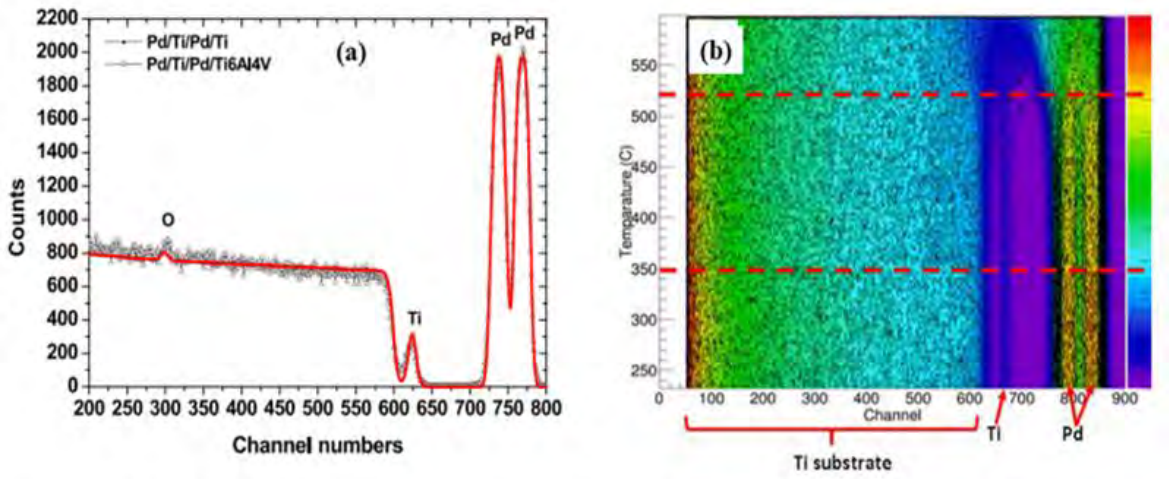

Figure 2.4: *(a) Real time RBS spectra with simulation (red line) and (b) colour coded in-situ, real time RBS plot [2.27].*

Several authors have taken advantage of the benefits of *in situ*, real-time RBS to study and monitor reactions of thin films. Theron et al. [2.28] demonstrated the applicability of *in situ*, real-time RBS in studying solid-state reactions in film by measuring the reaction kinetics of formation of Pd_2Si on Si substrate. They were also able to obtain the activation energy and pre-exponential factor from a single sample after a single annealing process in real time.

Chowles et al. [2.29] used real-time RBS to characterise the formation of $CuInSe_2$ that was grown by sequential evaporation of copper (Cu), indium (In) and selenium (Se) elemental layers onto molybdenum (Mo) coated glass. The as-deposited layers were characterised using RBS and XRD, respectively. The results of RBS showed that Cu and In had already mixed at room temperature, however no peak associated with Cu/In was seen on XRD. The thin film was then subjected to annealing at 200 °C and characterised using XRD and real-time RBS. XRD showed the presence of $CuSe_2$ and α-CuSe while real-time RBS showed interdiffusion of Cu and Se.

Real time RBS was also used by Pondo [2.30] to understand the processes and mechanism involved in germanium metallization and properties of phases formed. Electron beam (*e-beam*) was used to deposit the tantalum (Ta) an inert marker and nickel (Ni) on Germanium (Ge) substrate. The films where then studied with *in situ*, real-time RBS. The study identified that Ni_5Ge_3 phase forms first followed by NiGe. Furthermore, it was also determined that during the formation of Ni_5Ge_3 only Ni diffuse while both Ni and Ge diffuse during the formation of NiGe.

These selected studies show the advantages of real time RBS as a characterization technique for thin films, and tracking of the reactions while subjecting the sample to thermal treatment.

2.9 Light Amplification by Stimulated Emission of Radiation

Light Amplification by Stimulated Emission of Radiation (*Laser*) was first developed in the 1960s [2.31]. Since those early days and through extensive research and development, lasers have found application in many different fields. These range from material processing, material characterisation, telecommunication, and medical field among others [2.32]. The application of laser is such diverse fields is largely due to the properties of laser light. Laser light has a high degree of spatial and temporal coherence, is monochromatic and has a narrow spectral width [2.33].

Laser consists of 3 basic components i.e., lasing medium, pumping source and optical resonator [2.31]. The lasing medium is usually a solid crystal or a gas. For lasing and light amplification to occur, population inversion must occur between the energy states i.e., more atoms must be at the excited level. When excited atoms absorb a photon, they move to lower level by releasing photon thereby amplifying the light. Figure 2.5 show a 4-level laser action.

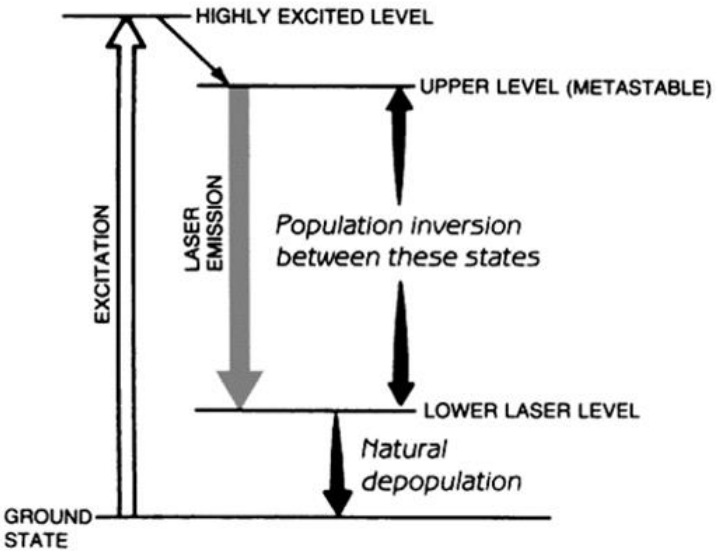

Figure 2.5: *Schematic diagram of energy levels in a 4-level laser [2.31].*

Also shown in figure 2.5 is the presence of a metastable state. This is necessary because excited atoms will release photons within nano- or pico-seconds of their elevation to the excited state [2.31]. This time is too short for stimulated emission to occur hence the need for metastable state. This state lasts for milliseconds which is a long enough time for stimulated emission to occur.

Population inversion comes about because of pumping. Pump source for solid-state laser is usually flash lamps or another laser [2.31]. In the case of a gas laser, pump source can be either direct current (dc) or radiofrequency (RF). As lasing atoms in the excited state relax via radiative process, photon emission occurs spontaneously or because of stimulation [2.34]. Spontaneously emitted photons have random directionality therefore not useful in the design of a laser other than as the initiator of emission [2.34]. Stimulated emission photon strikes the excited medium resulting in stimulated emission. The photon released because of stimulated emission has the same frequency, phase, polarization, and propagation direction as the photon that induced the stimulated emission [2.34]. The optical resonator is used to reflect laser light back through the lasing medium for purpose of amplification via stimulated emission while the pumping source maintains a population inversion between upper and lower energy state.

2.9.1 Laser matter interaction

The interaction of laser with matter has also been an area of active research ever since the ruby laser was developed in the 1960s [2.35]. The interest in understanding laser matter interaction is driven by the need to understand the processes that occur when laser interact with matter since laser has many applications e.g., micromachining, chemical analysis, and pulse laser deposition of thin films to name a few. Interaction of laser with solid matter is a complex process that can result in several processes as shown in figure 2.6. The interaction involves heating, melting, vaporization, ejection of atoms, shock waves, plasma initiation and plasma expansion [2.36]. The response of the material depends on the type of material i.e., conductors, semi-conductors and dielectrics will respond differently to laser. Also important are the characteristics of the laser for example, wavelength, pulse duration, repetition rate and pulse energy.

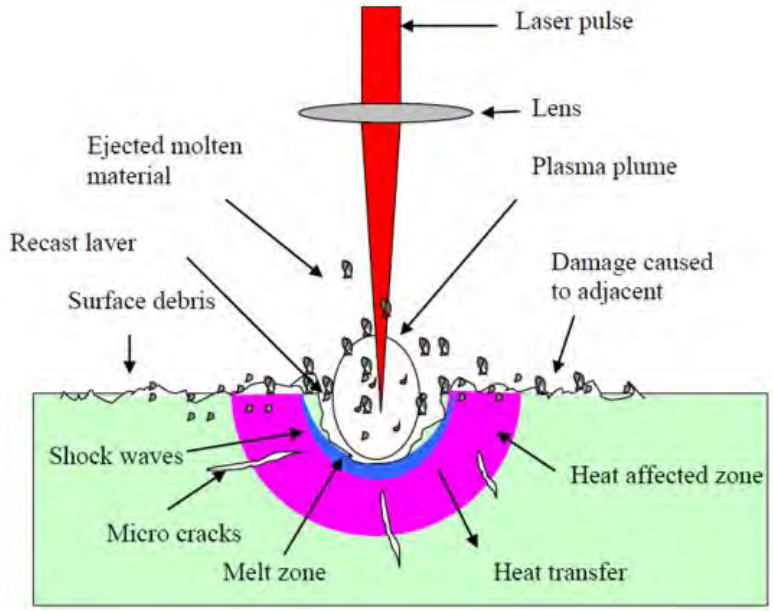

Figure 2.6: *Schematic diagram of the interaction of laser with matter [2.32].*

The response of the material to laser can either be thermal or non-thermal [2.37]. Thermal response is more pronounced when the pulse duration is long. In this case, laser radiation is absorbed by the electrons of the material. This absorption is followed by phonon-lattice interaction which leads to the conversion of the energy absorbed into heat in the material. This takes place within picosecond or nano-second after the deposition of laser pulses [2.38]. This leads to the melting and vaporization of the target material [2.39]. The increase in temperature of the material with time can be estimated with Fourier heat equation [2.39] given below:

$$[C_p + L_m(T - T_m) + L_v(T - T_v)]\rho \frac{\partial T(x,y,x,t)}{\partial t} - \nabla[k\nabla T] = Q \qquad (2.1)$$

where k = thermal conductivity ($\mathrm{W}m^{-1}K^{-1}$), ρ = material density ($\mathrm{kg}m^{-3}$),T_m melting temperature, T_v vaporisation temperature,L_v latent heat of vaporisation and Q laser source term ($\mathrm{W}m^{-3}$).

The temperature profile within the material after interaction with laser is Gaussian [2.38]. This creates a temperature gradient within the material which leads to the diffusion of heat along the temperature gradient. The diffusion is given by equation 2.2 below:

$$\rho C_P \frac{\partial T}{\partial t} = \mathrm{k}\nabla^2\mathrm{T} \tag{2.2}$$

While the heat diffusion length is given by equation 2.3 below:

$$l_t = \sqrt{2\,Dt_p} \tag{2.3}$$

where t_p is the duration of laser pulse and D is heat diffusivity [2.40] given by equation 2.4:

$$D = \frac{k}{C_p} \tag{2.4}$$

Non-thermal response occurs when the pulse duration is shorter. With a shorter pulse duration, the laser energy might be high enough to cause the bond between neighbouring atoms of the target material to break, while the electrons cools faster than the phonon-lattice interaction process [2.39].

2.9.2 Material Response to femtosecond laser

Femtosecond laser is a type of pulsed laser where the energy is compressed into a period of 10^{-13} s [2.40]. The development of femtosecond laser has thus opened several opportunities in material modification, studying of behaviour of material and properties under extreme conditions [2.41]. A detailed presentation of Femtosecond laser in given in **Chapter 3**.

When femtosecond laser is used to irradiate materials, the energy is absorbed by the electrons. The excited electrons thermalize [2.42] via electron-electron collisions. The collision of electrons leads to a significant increase in the temperature of the material. While the collisions are happening, the temperature of the lattice remain unchanged. As a result, a temperature gradient between the electrons and the lattice is created. This leads to heat flow from the high temperature electrons to the low temperature lattice [2.43]. This leads to the lattice continuing to receive heat for several picoseconds after the laser irradiation has passed [2.44]. This transfer of energy between the electron and the lattice leads to mechanical response and phase

transformation that occur far from equilibrium [2.45] i.e., out of thermodynamic equilibrium crystallographic phases can be formed when this type of fast pulsing heating is used.

2.9.3 Annealing with laser

Several authors have made use of different types of lasers in their studies to anneal the samples. This unconventional way of annealing results in the formation of out of thermodynamic equilibrium crystallographic phases.

In their study of liquid phase growth of Ni and Fe silicide, Weber et al. [2.46] made use of a nanosecond laser to irradiate the samples. The sandwich structures were deposited using electron beam evaporator on a Si substrate. These were then irradiated with 40 ns pulse duration Q switched Nd: YAG glass laser ($\lambda = 1.06$ μm) at energy densities varying between 0.3-1.9 J/ cm^{-2}. The samples were then investigated using RBS and TEM. The results showed the presence of a complete epitaxial layer of non-equilibrium Ni and Fe silicide phases, these decayed into equilibrium phases upon annealing. The composition of the film was determined with RBS and found to be 3-48 % Ni and 19-31 % Fe.

Allen et al. [2.47] studied phase transformation in laser irradiated Au-Si thin films, in this study, thin films or Au-Si were deposited on sapphire substrate in vacuum. These were then irradiated with pulses from Nd: YAG glass laser that was operated in Q-switch mode ($\tau \approx 30$ nm) or free running mode ($\tau \approx 300$ μs). The samples where quenched and characterized with XRD, RBS and the electrical conductivity was determined. XRD patterns of the sample that was irradiated with pulse of 30 nm showed that amorphous Au-Si structure formed with traces of metastable Au-Si. The sample irradiated with 300 μs pulse showed the formation of polycrystalline Au-Si structure and the presence of a metastable phase like that obtained in the sample irradiated with 30 nm pulses.

There have been several studies where laser was used for annealing samples and thereafter RBS used to characterise the sample as indicated in the some of the studies above. However, there is lack (or rather a gap) in literature of studies that combine both *in situ*, real-time RBS with laser annealing despite the benefits of *in situ,* real-time RBS in tracking of reaction.

In this study we therefore explore an unconventional method of annealing i.e., laser and *in situ* real-time RBS to monitor the formation Zn-Sn alloy in real time. A femtosecond pulsed

laser will be used to activate a reaction between two metals in a bi-metallic thin film system (Zn-Sn). This will be done in the RBS chamber, while probing the sample with energetic alpha particles for the tandetron accelerator. The results of this set up will be compared to the isothermal heating.

2.10 References

[2.1] Padhy, M. and Prasad, C.S., 2015. *Comparative Study of the Sn-Ag and Sn-Zn Eutectic Solder Alloy* (BTech Thesis).

[2.2] Wu, C.L., Yu, D.Q., Law, C.M.T. and Wang, L., 2002. The properties of Sn-9Zn lead-free solder alloys doped with trace rare earth elements. *Journal of electronic materials*, *31*(9), pp.921-927.

[2.3] Musa, S.A., Mohd Salleh, M.A.A. and Norainiza, S., 2013. Zn-Sn based high temperature solder-A short review. In *Advanced Materials Research* (Vol. 795, pp. 518-521). Trans Tech Publications Ltd.

[2.4] C.A.Harper (1997).Electronic Packaging and Interconnection Handbook,2rd ed.New York:McGraw-Hill

[2.5] Suganuma, K., Kim, S.J. and Kim, K.S., 2009. High-temperature lead-free solders: Properties and possibilities. *JOM Journal of the Minerals, Metals and Materials Society*, *61*(1), p.64.

[2.6] Menon, S., George, E., Osterman, M. and Pecht, M., 2015. High lead solder (over 85%) solder in the electronics industry: RoHS exemptions and alternatives. *Journal of Materials Science: Materials in Electronics*, *26*(6), pp.4021-4030.

[2.7] Shi, Y., Fang, W., Xia, Z., Lei, Y., Guo, F. and Li, X., 2010. Investigation of rare earth-doped BiAg high-temperature solders. *Journal of Materials Science: Materials in Electronics*, *21*(9), pp.875-881.

[2.8] Lee, J.E., Kim, K.S., Suganuma, K., Takenaka, J. and Hagio, K., 2005. Interfacial properties of Zn–Sn alloys as high temperature lead-free solder on Cu substrate. *Materials Transactions*, *46*(11), pp.2413-2418.

[2.9] Chen, X., Li, M., Ren, X.X., Hu, A.M., and Mao, D.L., 2006. Effect of small additions of alloying elements on the properties of Sn-Zn eutectic alloy. *Journal of Electronic Materials*, *35*(9), pp.1734-1739.

[2.10] Vianco, P.T., 1993. *Development of alternatives to lead-bearing solders* (No. SAND-93-0225C; CONF-9308126-1). Sandia National Labs. Albuquerque, NM (United States); National Centre for Mfg. Sciences, Ann Arbor, MI (United States).

[2.11] Handbook, M., 1990. Vol. 2. *Properties and Selection: Nonferrous Alloys and Special-Purpose Materials*, *713*.

[2.12] Lewis Sr, R.J., 2008. *Hazardous chemicals desk reference*. John Wiley & Sons.

[2.13] Needleman, H.L. and Bellinger, D., 1991. The health effects of low-level exposure to lead. *Annual review of public health*, *12*(1), pp.111-140.

[2.14] Papanikolaou, N.C., Hatzidaki, E.G., Belivanis, S., Tzanakakis, G.N. and Tsatsakis, A.M., 2005. Lead toxicity update. A brief review. *Medical science monitor*, *11*(10), pp.RA329-RA336.

[2.15] Wang, C.H., Chen, H.H., and Li, P.Y., 2012. Interfacial reactions of high-temperature Zn–Sn solders with Ni substrate. *Materials Chemistry and Physics*, *136*(2-3), pp.325-333.

[2.16] Osório, W.R., Leiva, D.R., Peixoto, L.C., Garcia, L.R. and Garcia, A., 2013. Mechanical properties of Sn–Ag lead-free solder alloys based on the dendritic array and Ag3Sn morphology. *Journal of Alloys and Compounds*, *562*, pp.194-204.

[2.17] Karakaya, I. and Thompson, W.T., 1987. The Ag-Sn (silver-tin) system. *Bulletin of Alloy Phase Diagrams*, *8*(4), pp.340-347.

[2.18] Okamoto, H., 2012. Bi-Sb (bismuth-antimony). *Journal of Phase Equilibria and Diffusion*, *33*(6), pp.493-494.

[2.19] Goodwin, F.E., 2018. Zinc and zinc alloys. In *Springer Handbook of Materials Data* (pp. 431-442). Springer, Cham.

[2.20] Vollweiler, F. O. (1993). Intermetallic growth at the interface between copper and

Bismuth-tin solder. NAVAL POSTGRADUATE SCHOOL MONTEREY CA.

[2.21] Li, W.L. "Microstructure and adhesion strength of Sn-9Zn-1.5Ag-xBi (x=0wt% and 2 wt. %) /Cu after electrochemical polarization in a 3.5wt% NaCl solution", Journal of Alloys and Compounds

[2.22] P. Nash, A. Nash, H. Baker et al, “Alloy phase diagrams, ASM Handbook 3”, Materials Park, OH, (1990), p.372

[2.23] Jiang, J., Lee, J.E., Kim, K.S. and Suganuma, K., 2008. Oxidation behaviour of Sn–Zn solders under high-temperature and high-humidity conditions. *Journal of alloys and compounds*, *462*(1-2), pp.244-251.

[2.24] Wein-Kan Chu, James W Mayer, Marc-A.Nicolet, Backscattering Spectroscopy Academic Press (1978).

[2.25] Kimura, K., 2006. Rutherford Backscattering Spectroscopy. *Encyclopedia of Analytical Chemistry: Applications, Theory and Instrumentation*.

[2.26] Karl, H., Großhans, I., Wenzel, A., Stritzker, B., Claessen, R., Strocov, V.N., Cirlin, G.E., Egorov, V.A., Polyakov, N.K., Samsonenko, Y.B. and Denisov, D.V., 2002. Stoichiometry and absolute atomic concentration profiles obtained by combined Rutherford backscattering spectroscopy and secondary-ion mass spectroscopy: InAs nanocrystals in Si. *Nanotechnology*, *13*(5), p.631.

[2.27] Magogodi, S., Mtshali, C., Halindintwali, S., Khumalo, Z., Mongwaketsi, N., Cloete, K., Madito, M., Pieters, C., Sook, A., Mc Donald, E. and Cummings, F., 2019. Effect of the annealing atmosphere on the layer interdiffusion in Pd/Ti/Pd multilayer stacks deposited on pure Ti and Ti-alloy substrates. *Nuclear Instruments and Methods in Physics Research Section B: Beam Interactions with Materials and Atoms*, *461*, pp.37-43.

[2.28] Theron, C.C., Mars, J.A., Churms, C.L., Farmer, J. and Pretorius, R., 1998. In situ, real-time RBS measurement of solid-state reaction in thin films. *Nuclear Instruments and Methods in Physics Research Section B: Beam Interactions with Materials and Atoms*, *139*(1-4), pp.213-218.

[2.29] Chowles, A.G., Engelbrecht, J.A.A., Neethling, J.H. and Theron, C.C., 2000. In situ RBS analysis of CuInSe2. *Thin solid films*, *361*, pp.93-97.

[2.30] Pondo, K.J. 2010.*In situ real time RBS study of Ni/Ge interaction.* MSc thesis, University of Zambia.

[2.31] Hecht, J., 2018. *Understanding lasers: an entry-level guide*. John Wiley & Sons.

[2.32] Steen, W.M. and Mazumder, J., 2010. *Laser material processing*. Springer Science & Business media.

[2.33] Paschotta, R., 2008. Field guide to lasers (Vol. 12). Bellingham, WA: SPIE.

[2.34] Harter, D.J., Pessot, M.A., Squier, J.A., Nees, J.A., Bado, P. and Mourou, G.A., 1990, May. Short pulse amplification in tunable solid state materials. In *Femtosecond to Nanosecond High-Intensity Lasers and Applications* (Vol. 1229, pp. 19-28). International Society for Optics and Photonics.

[2.35] Darke, S.A. and Tyson, J.F., 1993. Interaction of laser radiation with solid materials and its significance to analytical spectrometry. A review. *Journal of Analytical Atomic Spectrometry*, *8*(2), pp.145-209.

[2.36] Arrowsmith, P., 1987. Laser ablation of solids for elemental analysis by inductively coupled plasma mass spectrometry. *Analytical Chemistry*, *59*(10), pp.1437-1444.

[2.37] Fardel, R., Nagel, M., Lippert, T., Nüesch, F., Wokaun, A. and Luk'Yanchuk, B.S., 2008. Influence of thermal diffusion on the laser ablation of thin polymer films. *Applied Physics A*, *90*(4), pp.661-667.

[2.38] McDonnell, C., 2015. *Pulsed laser material interaction with thin indium tin oxide films* (Doctoral dissertation, PhD Thesis, National University of Ireland, Galway).

[2.39] Russo, R.E., Mao, X., Liu, H., Gonzalez, J. and Mao, S.S., 2002. Laser ablation in analytical chemistry—a review. *Talanta*, *57*(3), pp.425-451.

[2.40] Ossi, P.M. and Zhigilei, L. eds., 2014. *Lasers in materials science*. Cham: Springer.

[2.41] Shugaev, M.V., Wu, C., Armbruster, O., Naghilou, A., Brouwer, N., Ivanov, D.S., Derrien, T.J.Y., Bulgakova, N.M., Kautek, W., Rethfeld, B. and Zhigilei, L.V., 2016. Fundamentals of ultrafast laser–material interaction. *MRS Bulletin*, *41*(12), pp.960-968.

[2.42] Chichkov, B.N., Momma, C., Nolte, S., Von Alvensleben, F. and Tünnermann, A., 1996. Femtosecond, picosecond, and nanosecond laser ablation of solids. *Applied physics A*, *63*(2), pp.109-115.

[2.43] Ivanov, D.S. and Zhigilei, L.V., 2003. Effect of pressure relaxation on the mechanisms of short-pulse laser melting. *Physical review letters*, *91*(10), p.105701.

[2.44] Sokolowski-Tinten, K., Bialkowski, J., Cavalleri, A., von der Linde, D., Oparin, A., Meyer-ter-Vehn, J. and Anisimov, S.I., 1998. Transient states of matter during short pulse laser ablation. *Physical Review Letters*, *81*(1), p.224.

[2.45] Gattass, R.R. and Mazur, E., 2008. Femtosecond laser micromachining in transparent materials. *Nature photonics*, *2*(4), pp.219-225.

[2.46] Weber, B., Gärtner, K., Witzmann, A., Kaschner, C. and Kasko, I., 1992. Non-equilibrium epitaxial silicides-a special effect of silicide formation by ns-laser irradiation. *Applied surface science*, *54*, pp.381-385.

[2.47] Von Allmen, M., Lau, S.S., Mäenpää, M. and Tsaur, B.Y., 1980. Phase transformations in laser-irradiated Au-Si thin films. *Applied Physics Letters*, *36*(3), pp.205-207.

CHAPTER 3

Sample preparation and characterisation techniques

3. Background

In this study, electron beam evaporation system (*e-beam*) was used to deposit zinc-tin (Zn-Sn) thin films on borosilicate glass substrate. The pristine and treated thin films were characterized with the following techniques: x-ray diffraction (XRD), Rutherford backscattering spectrometry (RBS), scanning electron microscopy (SEM) and atomic force microscopy (AFM). This chapter, therefore, gives the theoretical basis upon which the experimental and characterisation techniques used in this study are built upon. The theory of each technique is followed by a detailed experimental setup for each of the experiments. Also presented in this chapter is a detailed explanation about the functioning of a femtosecond laser together with the theories of phase formation and reaction kinetics analysis.

3.1 Electron Beam Evaporation

Thin films can be deposited using various deposition techniques, with the most commonly used being physical vapour deposition (PVD), chemical vapour deposition (CVD) and liquid-phase processes [3.1]. PVD are deposition techniques that use targets that are in a solid state (i.e., metals, ceramics, and dielectrics). During a PVD, the atoms are transferred from the target to the substrate either by thermal process or energetic particles sputtering off the atoms to the substrate. CVD deposition technique on the other hand generally use gaseous state molecules to deposit thin films on a substrate.

In this study, thin films where deposited using electron beam evaporator (*e-beam*) which is a type of PVD technique. Electron beam evaporation is one of the more popular PVD technique for the deposition of thin films due to its versatility. E-beam can evaporate target materials with high melting points relatively easy and the rate of deposition is controllable [3.1]. This technique uses thermionic electrons from a resistively heated tungsten filament. The electrons are emitted from the surface of the filament. Electromagnetic field focuses these electrons onto the target material in the crucible. Depending on the physical properties of the target, the material can either melt, and evaporate or directly sublimate when being heated by thermionic

electrons. The evaporated or sublimated atoms travel to the substrate, once on the substrate, the atoms find energetically favourable sites before condensing. This will result in agglomeration and coalescence of the atoms resulting in a smooth continuous thin film [3.2]. The evaporation of the thin films takes place under high vacuum in order to have good free mean path between the atoms and substrate. Furthermore, high vacuum prevents air contamination of the growing thin film. Rotatory pump, turbo pump and titanium sublimation pump are employed to maintain the high vacuum pressure of the system.

3.1.1 Substrates preparation and cleaning

In this study, thin films were deposited on borosilicate glass substrate. The substrates were cut into squares of approximately 10 mm × 10 mm. The substrates were ultrasonically cleaned in a bath of acetone, methanol, and de-ionised water sequentially with each step lasting 10 minutes. Prior to being loaded to the e-beam, the substrates were blown with nitrogen gas.

3.1.2 Electron beam evaporation experimental setup

Electron beam evaporation (*e-beam*) system shown in figure 3.1 was used to deposit Zn-Sn thin films. The e-beam used is found in the solid-state laboratory within the Tandetron Laboratory at iThemba LABS-NRF.

Figure 3.1: *Electron beam evaporation system at iThemba LABS that was used for deposition of thin films.*

The substrates were mounted onto labelled sample holders. The sample holders where then placed on a rotating platform shown in figure 3.2a. The sample holders were place on the platform such that the substrates were facing down as shown in figure 3.2b.

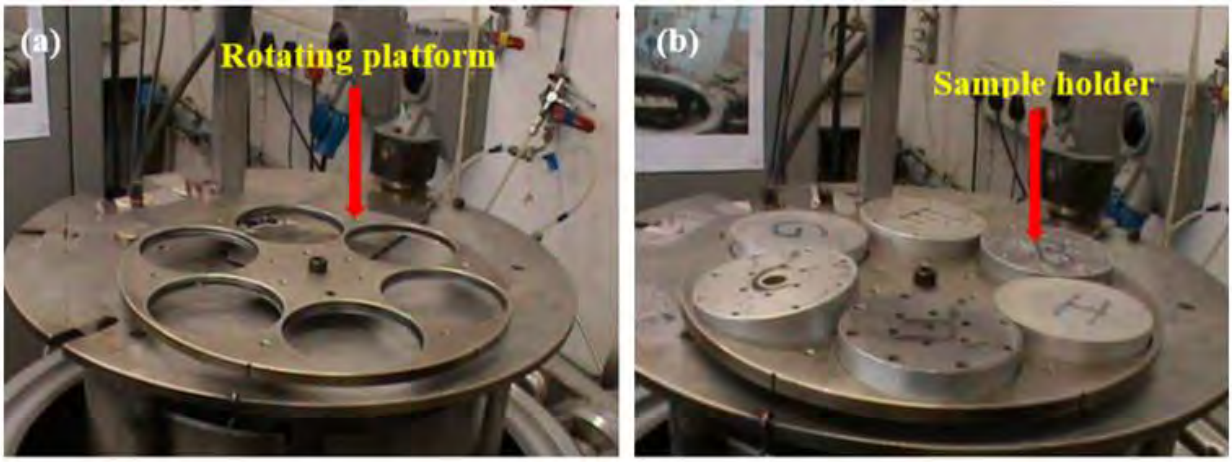

Figure 3.2: *(a) Rotating platform and (b) Sample holders inside e-beam chamber.*

The evaporator consists of a copper crucible with three target holders for the material to be evaporated (*target material*). To prevent contamination during evaporation, the holders are separated from each other by a partitioning wall that is approximately 20 mm in height as shown in figure 3.3. Prior to placing Sn and Zn in their respective holders, the holders were cleaned with acetone. Once the substrates and target material were placed within their respective holders, the e-beam chamber was closed. Rotary pump was used to evacuate the chamber. Turbo pump and sublimation pump were then used to pump down the chamber to a base pressure of $3 \times 10^{-6} mbar$ overnight. To obtain an even high vacuum pressure within the chamber, liquid nitrogen was added in the ion trap chamber which resulted in a pressure of $2 \times 10^{-7} mbar$ prior to deposition.

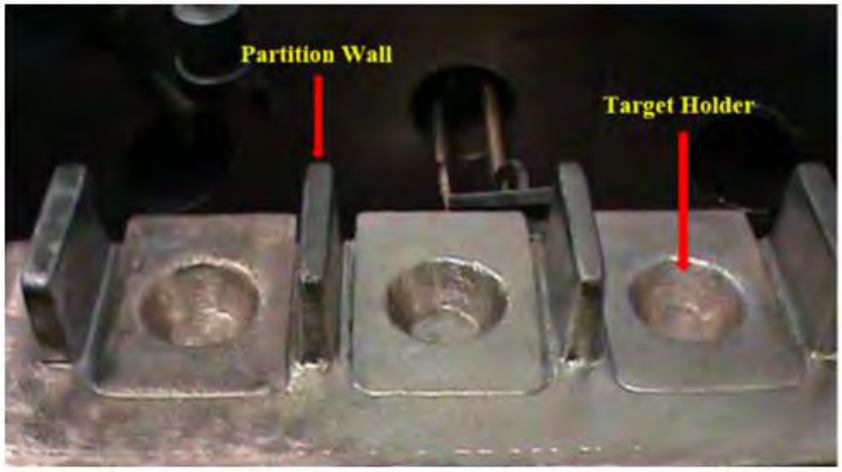

Figure 3.3: *Copper crucible where target material is placed.*

The electron gun was switched on and Sn was degassed prior to deposition. Once degassing was complete, the shatter was opened using magnet shown in figure 3.4, Sn was deposited onto the substrates at a rate of between 1.2 Å/s and 3 Å/s. The rate was kept between this range by adjusting the current that flowed through the tungsten filament. The thickness of the Sn was measured by a crystal monitor and it was measured to be 50 nm.

Figure 3.4: *Shutter of the e-beam and magnet used to open and close it during experiment.*

Once 50 nm of Sn was deposited, the shatter was closed. The holder with Zn was then moved into position, i.e., in line with the filament and hence the path of electron beam. Tin was then degassed after which the shatter was opened, and Zn was deposited on top of the Sn layer that was already deposited. Zinc was deposited at a rate between 2.4 Å/s and 4 Å/s, pressure inside the chamber during deposition was $3 \times 10^{-7} mbar$.

3.2 X-ray diffraction technique (XRD)

X-ray diffraction (XRD) is a technique based on the interaction of mono-chromatic x-rays with the lattice planes of the sample being analysed. When this mono-chromatic beam of x-rays impinges on a sample, it is diffracted, and the intensity of the diffracted beam is measured. Figure 3.5 shows the schematic diagram of x-ray diffractometer with the different components and their relation to each other.

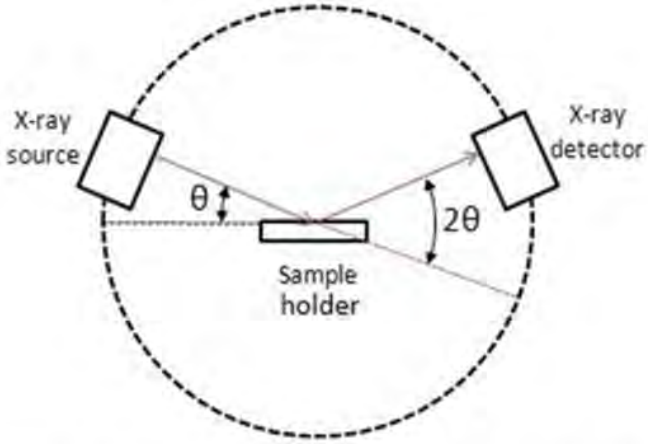

Figure 3.5: *Schematic diagram of the components of XRD and how they relate to each other [3.3].*

From the diffracted x-rays, certain important information about the sample can be extracted. For example, it can be determined whether the sample is crystalline, poly-crystalline or amorphous, particle size as well as unit cell size dimension can also be determined.

3.2.1 X-ray emission

X-rays are electromagnetic radiation with short wavelengths of between 10 nm and 10 pm [3.3]. The lower wavelength x-rays are classified as hard x-rays and the longer wavelength are classified as soft x-rays [3.3]. X-ray radiation is produced within the x-ray tube (*see figure 3.6*) when a thermionic gun that is capable of emitting electrons is resistively heated by passing a current through it. The emitted electrons are then accelerated through the potential difference of 200 kV. These electrons hit the copper target which leads to the excitation of some of the target's electrons to the anti-bonding state from their orbital [3.3]. This excitation creates a vacancy which is filled by electrons from higher energy orbital. During this transition from

higher energy orbital to lower energy orbital, energy in the form of x-rays is released because of the energy difference between initial and final energy states.

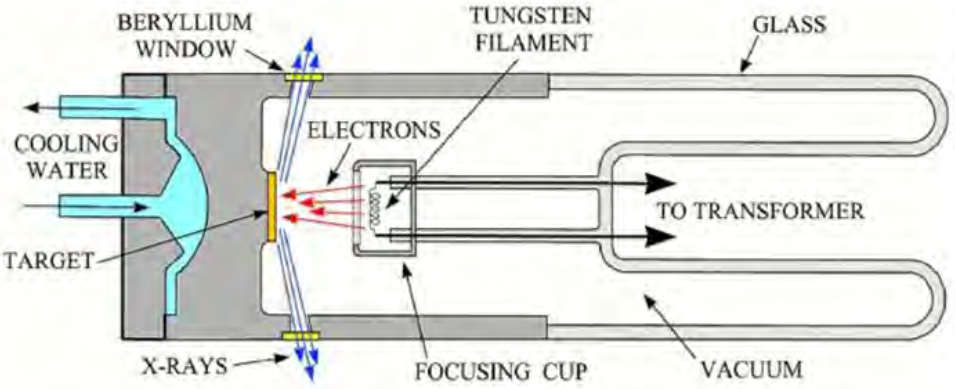

Figure 3.6: *Cross section of x-ray tube showing the process during the production of x-rays [3.4].*

During x-ray emission, rays of different wavelengths are emitted. However, for the purposes of analysis, monochromatic x-rays are required. As a result, a filter material is used in order to remove the undesired wavelengths for the purposes of analysis. This material is designed in such a way that its absorption edge lies more towards the K_β of the cupper target [3.3]. This attenuate the unwanted wavelengths such that only the $K_{\alpha 1}$ monochromatic x-ray is left [3.3]. It is this monochromatic x-ray that impinge on the sample that is being analysed. When this monochromatic x-ray impinges on the sample, some are transmitted while others are diffracted by atomic planes in the sample. The diffracted x-rays are collected by the detector and analysed by a digital data acquisition system.

3.2.2 Braggs Law

Once the x-rays have been produced inside the x-ray tube, they are collimated and directed towards the sample for characterization purposes. When x-rays beam impinges on a crystalline material, it is scattered by the scattering centres that lie on the lattice plane of the sample [3.5]. These planes are separated by interplanar spacing d. Figure 3.7 shows the interaction of x-ray beam with crystalline sample.

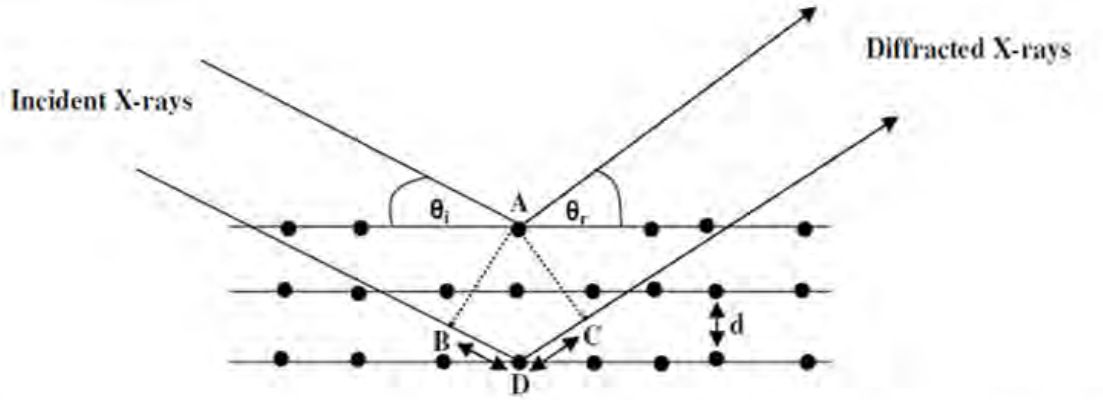

Figure 3.7: *Schematic of the interaction of x-rays with atoms of a crystalline material [3.6].*

The scattering of monochromatic x-rays by planes leads to the formation of x-ray diffraction pattern by constructive interference of the scattered beam at specific angels. Constructive interference occurs only when Braggs Law [3.6] conditions are met. Braggs Law is given by equation 3.1 below:

$$n\lambda = 2d\sin\theta \tag{3.1}$$

where n - 1, 2, 3… order of diffraction, λ − wavelength of incident x-ray, d - distance between adjacent plane and θ − diffraction angle in degrees.

Bragg's law is only satisfied when the parallel x-rays that impinges on the sample undergo constructive interference. From figure 3.7 above, x-rays diffracted by atoms at A will follow a different path from those diffracted by atoms at D. If, however the difference in the paths of the two x-rays is an integer number of λ, the x-ray will at some point be on the same phase [3.6]. When this occurs, constructive interference takes place, and a diffraction pattern is produced. The intensities of the diffracted x-rays are recorded as a function of 2θ angle. By plotting the intensities against the 2θ, a pattern that is specific to the material that is being studied is obtained.

3.2.3 Scherrer equation

The size of the crystallite in the sample can be related to the broadening of the peaks in the XRD Bragg peak. This relationship is given by the Scherrer equation 3.2 below:

$$D = \frac{K\lambda}{B\cos\theta} \tag{3.2}$$

where D = mean crystal size, K= dimensionless shape factor, λ = wavelength of x-ray, B = line broadening at full width half maximum (FWHM) and Θ = Braggs angle.

This equation is used to determine the size of crystallite in the material. Scherrer equation can only be applied to nano-size particles and not in grains larger than 0.1 – 0.2 μm [3.5].

3.2.4 Experimental setup

The crystal structure of the as-deposited samples as well as annealed samples were studied with x-ray diffractometer. A Bruker Advance D8 X-ray diffractometer shown in figure 3.8 was used.

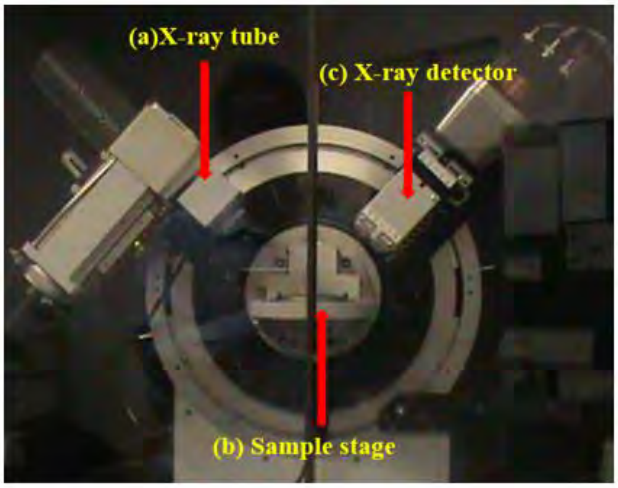

Figure 3.8: *D8 Bruker diffractometer with components: a) X-ray tube, b) Sample stage and c) x-ray detector.*

The diffractometer was configured such that the x-ray tube and the detector moved in a locked couple mode, 2θ-θ scan mode. In this mode, when the x-ray tube moves by an angle θ, the detector also move by θ. During the analysis, both the detector and the x-ray tube move while the sample remains in a fixed position. The diffractometer used monochromatic $K_{\alpha 1}$ copper X-rays as x-ray source with wavelength of 1.54 Å. The x-ray tube was operated with voltage and current of 40 kV and 40 mA, respectively. Data was collected between 20° and 90° in 2θ and the step size and time were 0.034 and 1 s per step, respectively. The x-ray diffraction patterns were then compared to the patterns found in the International Centre for Diffraction Data (ICDD) in order to identify the phases. The XRD data was then plotted using Origin Software.

3.3 Rutherford backscattering spectrometry (RBS)

Since the first scattering experiment by Geiger and Marsden [3.7], whose effects where later explained by Rutherford atomic model, Rutherford backscattering spectrometry (RBS) has become one of the most commonly used analytical technique [3.8]. As an analytical technique, RBS is a simple technique that can be used to study thin films. Figure 3.9 shows the layout of RBS line at iThemba LABS that was used in this study.

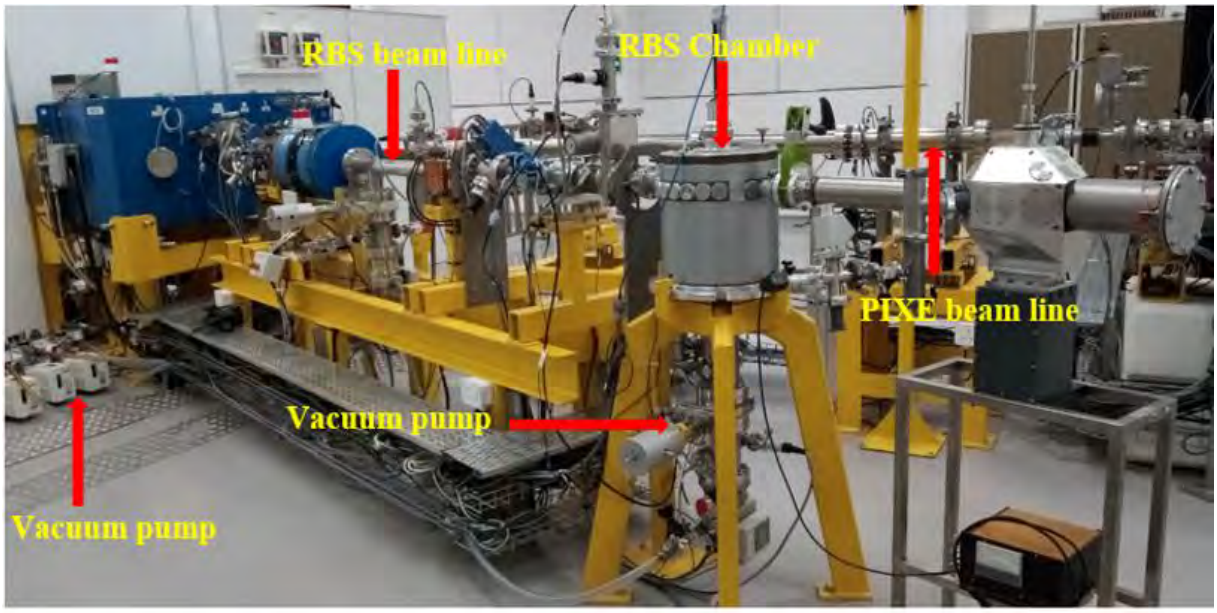

Figure 3.9: *Tandetron Accelerator at iThemba LABS that was used in this study.*

During RBS experiment, a collimated, mono-energetic alpha particle, typically He^{++} particle impinges on a target material. The alpha particles penetrate the target material and gradually slow down. Some of the alpha particles collide with the atoms of the target material and this results in scattering and energy transfer. When the backscattered alpha particle strikes a detector, an electrical signal is generated.

Rutherford backscattering is based on 3 physical principles:

- Kinematic factor (K)
- Energy loss $\left(\frac{dE}{dx}\right)$
- Differential scattering cross section $\left(\frac{d\sigma}{d\Omega}\right)$

3.3.1 Kinematic factor (K)

When atoms of a stationary target material are bombarded with alpha particles, the alpha particles maybe scattered by the atoms of the target material. For this to occur, the energy of the alpha particle must be larger than the binding energy of the atoms in the material being bombarded by the alpha particles [3.9]. The energy of the alpha particle must however be below the energy at which nuclear reaction occurs [3.9]. In such a case, the interaction of alpha particles and the target can be treated as simple elastic collision [3.9] and therefore the laws of energy and momentum conservation can be applied.

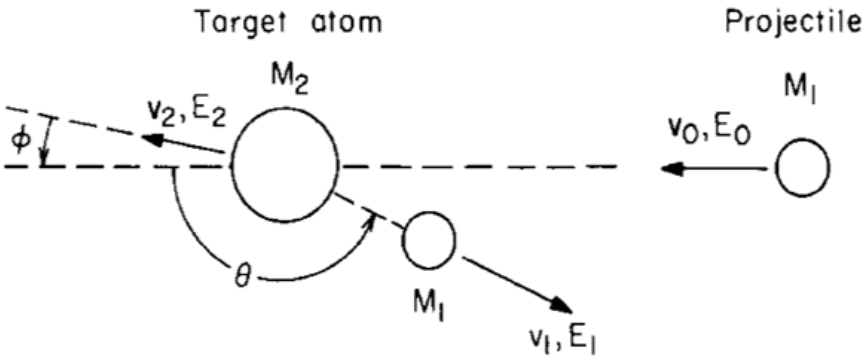

Figure 3.10: *Schematic diagram of elastic collision between a projectile M_1 and a target atom M_2 [3.10].*

Figure 3.10 shows an interaction between alpha particle of mass M_1, velocity v_0 and energy E_0 with a stationary mass M_2. When the alpha particle collides with a stationary target M_2 , energy is transferred from M_1 to M_2. The velocities and energy after collision are v_1,E_1 and v_2,E_2 respectively. The energy of the backscattered particles depends on the mass of the incident particles and the mass of the target atoms.

Kinematic factor (K), is defined as a ratio of energy before collision (E_0) and the energy after collision (E_1) as shown in equation 3.3:

$$K = \frac{E_1}{E_0} \tag{3.3}$$

If the collision between M_1 and M_2 is elastic, the ratio of projectile energies can be calculated by applying the principle of energy and momentum conservation provided that $M_1 < M_2$:

$$K = \frac{E_1}{E_0} = \left[\frac{\sqrt{M_2^2 + M_1^2 \ sin^2\theta} + M_1 \cos\theta}{M_1 + M_2}\right]^2 \tag{3.4}$$

Equation 3.4 shows that the energy of the backscattered particles depends on the mass of the target and scattering angle. The equation also shows that kinematic factor on the other hand depends on M_2 because M_1 and angle of the detector remain constant.

If E_0 and M_1 are known, then the mass of M_2 can be determined by measuring E_1, the energy of backscattered particle. Equation 3.4 show that the heavier the element the higher the energy that is scattered. The scattered energy E_1 is maximum when the scattering angle is 180˚. Kinematic factor allows for the identification of mass of target atom by measuring the scattered particle energy.

3.3.2 Energy loss

When alpha particles impinge on a target material, they penetrate the target material. As the alpha particle travel along the path, it interacts with electrons of the target material and thus lose energy. The amount of energy loss along the path depends on three things, the distance

travelled by the alpha particle, the velocity of the particle and the density and composition of target material [3.11]. Depth perception in RBS follows directly from the energy lost by the alpha particles and energy loss affects both quantitative and compositional analysis [3.12]. The amount of energy lost by a particle per unit length is defined by equation 3.5 below as:

$$\frac{\Delta E}{\Delta x} \equiv \frac{dE}{dx} \tag{3.5}$$

When the collision between alpha particle and target is major, the particle will change trajectory into an outward direct and will continue to lose energy until it emerges.

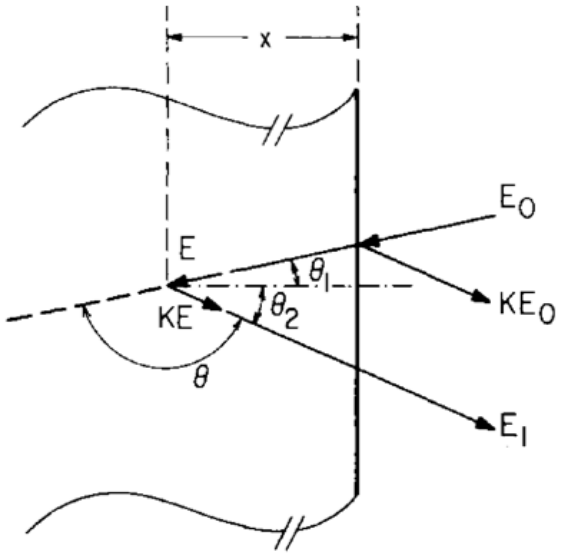

Figure 3.11: *Schematic diagram showing the loss of energy by a projectile as it is backscattered from a depth x [3.10].*

Figure 3.11 shows the path travelled by the alpha particle with E_0, E, KE and E_1 being energy of the incident particle, energy before scattering at depth x, energy after scattering at depth x and energy that emerges at the surface, respectively. From figure 3.11, there are three ways in which the particle can lose energy as it transverse the target material:

1. Energy loss as the alpha particle moves along the inward path of the target and this is given by equation 3.6:

$$\Delta E_{in} = \frac{x}{cos\theta_1}\frac{dE}{dx}\Big|_{in} \tag{3.6}$$

2. Energy loss due to backscattering of projectile given by equation 3.7:

$$\Delta E \ (\Delta E = E\text{- } KE) \tag{3.7}$$

3. Energy loss on the outward path given by equation 3.8:

$$\Delta E_{out} = \frac{x}{cos\theta_2}\frac{dE}{dx}|_{out} \tag{3.8}$$

It is therefore possible to determine the energy loss of backscattering particles and depth x by equation 3.9:

$$\Delta E = [S]x \tag{3.9}$$

where ΔE = is difference in energy between particles scattered from atom at surface and those scattered from atom at depth x and S is the energy loss factor:

$$[s] = \frac{K}{cos\theta_1}\frac{dE}{dx}|_{in} + \frac{1}{cos\theta_2}\frac{dE}{dx}|_{out} \tag{3.10}$$

Therefore, by measuring energy difference ΔE, thickness of the sample can be determined. Alternatively, the thickness can be determined by simulation of the spectra by making use of a software like SIMNRA.

3.3.3 Differential scattering cross section

Differential scattering cross section $\left(\frac{d\sigma}{d\Omega}\right)$, gives the relationship between the number of atoms in the target material and detected particles. The number of particles that can be detected by a detector with solid angle Ω is given by equation 3.11 below:

$$Y = \sigma(\theta)\Omega Q N_s \tag{3.11}$$

where σ (θ) is scattering cross section, which represent the probability of a particle being backscattered towards a detector at an angle θ, N_s is the number of target atoms per cm^2 and Q is the total number of incident particles.

By considering the Coulomb repulsion of two nuclei, the differential scattering cross section can be determined by Rutherford scattering cross section in the laboratory frame of reference:

$$\left(\frac{d\sigma}{d\Omega}\right) = \left(\frac{Z_1 Z_2 e^2}{4E_0}\right)^2 \frac{4\left(M_2\, cos\, cos\, \theta\, + \sqrt{M_2^2 - M_1^2 sin^2\theta}\right)^2}{M_2 sin^4\theta \sqrt{M_2^2 - M_1^2 sin^2\theta}} \tag{3.12}$$

Z_1 and Z_2 are the atomic number of a projectile of mass M_1 and target atoms of mass M_2 respectively. From equation 3.12, it can be seen that $\left(\frac{d\sigma}{d\Omega}\right)$ has a proportionality relation with Z_2^2 i.e., $\left(\frac{d\sigma}{d\Omega}\right) \propto Z_2^2$ .This shows that RBS is more sensitive to high Z elements.

3.3.4 In-Situ Real Time RBS

In this study, a variant of conventional RBS i.e., *in-situ*, real time RBS was used. After it was first used by Rennie et al. [3.13] and further developed by Theron et al. [3.14], *in-situ*, real time RBS has become a more convenient technique than conventional RBS in studying thin films. This technique combines both the depth profiling and compositional capabilities of conventional RBS with *in-situ* annealing [3.15].

With conventional RBS, samples are prepared, annealed and spectra obtained after annealing in furnace [3.16]. The samples are then compared to look at phase evolution at different annealing temperatures. This approach has several problems including [3.17]:

- Variation in sample preparation
- More material required.
- More time required.

Because of some of the reasons mentioned above, *in-situ*, real time RBS is more convenient as only one sample is used for the whole annealing range of temperatures and thus eliminating the limitations associated with conventional RBS.

3.3.5 Rutherford Experimental Setup

The Zn-Sn thin films were characterized with in-situ, real time RBS. This was carried out at the Tandetron Laboratory at iThemba LABS.

The thin film was mounted onto a sample stage made of copper with conductive silver paste. The stage was then placed inside the RBS chamber at a tilt angle of -5° with respect to the respect to the oncoming beam of alpha particle.

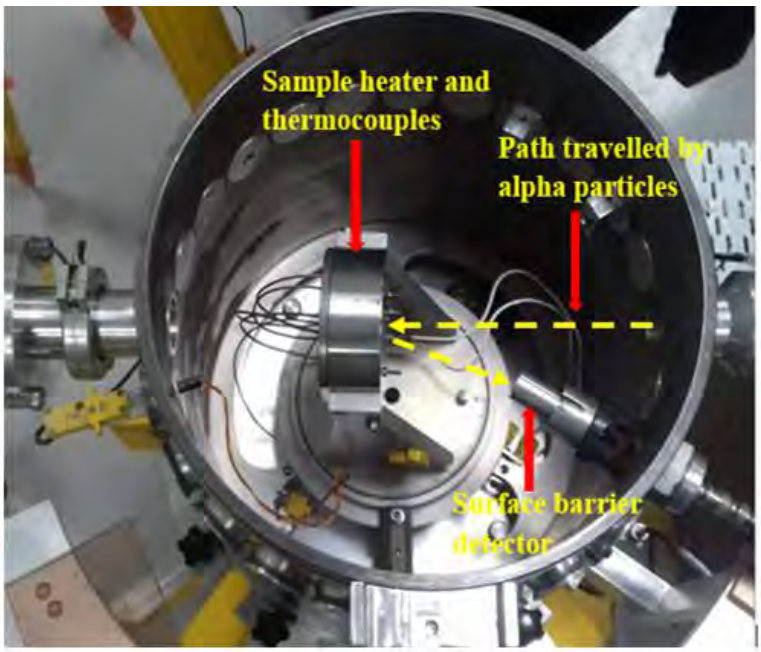

Figure 3.12: *Interior of RBS chamber showing sample heater, surface barrier detector and path travelled by alpha particles from beam line to the detector.*

A thermocouple was then mounted at the back of the stage to monitor the temperature during the experiment. The chamber was closed and pumped down to a base pressure of 5×10^{-6}mbar using a combination of turbo pump and rotary pump.

The sample was then irradiated with alpha particles with an energy of 3.045 MeV, with a scattering angle of 165°. The alpha particles emanated from the Tandetron accelerator, during the irradiation, the current and charge were 60 nA and 20 μC, respectively, and the beam spot size was 2 mm.

While being irradiated and spectra was being collected, the sample was subjected to ramped temperature annealing from room temperature to 350 °C at a rate of 2 °C/minute. The ramping was controlled by 818 Eurotherm microprocessor. The microprocessor serves as a link between the power supply and the thermocouple connected at the back of the sample stage. The spectra were collected continuously and stored regularly after every 30 s. The collected spectra were analysed with SIMNRA software.

3.4 Vacuum annealing experimental setup

In order to carry out complimentary characterization technique, pristine samples were annealed in vacuum annealed in a furnace. The samples where annealed at 180 °C, 200 °C and 260 °C The annealing process was carried out in a gauge pressure of 1×10^{-7}mbar, using an Elite Thermal System Limited furnace that is found in the solid state laboratory at iThemba LABS. The samples were placed in ceramic boats and loaded into the quartz tube of the furnace.

3.5 Introduction to femtosecond laser

Femtosecond laser is a type of pulsed laser where energy is compressed into a time period of 10^{-13}s [3.18]. The peak power of femtosecond laser can routinely be more than 10^{12}W, this is significantly higher than the peak power of 1000 W that can be achieved by continuous lasers [3.18]. The development of femtosecond laser has thus opened several opportunities in material modification, studying of behaviour and properties of material under extreme conditions [3.19].

The energy that comes out of a femtosecond laser can range from nanojoules to millijoules. At the nanojoule range, the energy is not enough for some of the applications where femtosecond

laser is employed. As a result of this, the pulses need to be amplified to microjoule or millijoules. However, because of the high pulse intensity of the femtosecond laser, direct amplification of this energy could result in damage of the optics of the laser.

Chirped pulse amplification (CPA) is a technique that was developed for the amplification of pulses without damaging the active medium or the optics [3.20]. CPA consists of 4 components i.e., oscillator, stretcher, amplifier, and compressor [3.20]. Figure 3.13 is a schematic diagram of chirped pulse amplification.

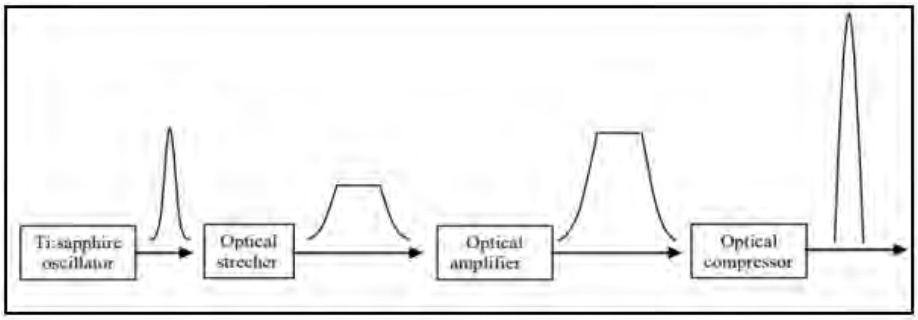

Figure 3.13: *Schematic diagram showing components of Chirped pulse amplification [3.21].*

3.5.1 Oscillator

The generation of laser pulses in the femtosecond time domain requires an active medium with a broad emission bandwidth [3.21]. The reason for this requirement is because of the relation between spectral bandwidth and pulse duration which is governed by equation 3.13, the Fourier-transform-limited pulse relation [3.21]:

$$\Delta v\, \Delta t \geq K \tag{3.13}$$

where Δv is the frequency bandwidth at full-width half maximum (FWHM), Δt is the FWHM in time of pulse and K constant that depends on pulse shape.

As a result of this requirement, a limited number of active media can be used for the generation and amplification femtosecond laser pulses [3.22].With a broad gain bandwidth of approximately 200 nm, high thermal conductivity and high damage threshold, titanium-sapphire ($Ti:Al_2O_3$) is the most used gain medium for the generation and amplification of femtosecond pulses [3.23]. The minimum pulse that can be generated by the $Ti:Al_2O_3$ is

approximately 5 fs [3.24]. This is determined from equation 3.14, the Fourier transformation equation:

$$\Delta t = K \frac{\lambda_0^2}{\lambda c} \tag{3.14}$$

where λ_0 is the central wavelength and c is the speed of light.

Due to the dependence of refractive index of a medium on wavelength, when light travels through a dispersive medium, different frequencies will travel at different speeds [3.21]. As a result of this, short pulses made up of different frequency components are stretched. For example, in positive dispersion, the higher frequency travels slower than the lower frequency and the pulse is thus positively chirped [3.21]. In a case of negative dispersion, the opposite occurs i.e., higher frequency component travels faster than lower frequency component and the pulse is said to be negatively chirped [3.21]. In ultra-short laser oscillator, positive dispersion in the gain medium and other optical components must be compensated. This is done by inserting an optical component with negative dispersion in the oscillator [3.21]

3.5.2 Stretcher

Pulses coming from the oscillator are of energy in the nanojoule and pulse duration of a few femtoseconds. These pulses are stretched before they are amplified to avoid damaging the optics and the gain medium. By using dispersion properties of gratings, the pulses can be stretched in time. Figure 3.14 shows the arrangement of the grating-pair used to stretch the pulses.

A telescope is placed between the grating pair, the dispersion is controlled by the effective distance between the second grating and the image of the first grating [3.25]. By making the distance between the gratings negative, the sign of dispersion of the grating pair can be changed from negative to positive [3.26]. Different frequency are dispersed by the grating into different direction. Therefore, each frequency has a different optical path and the one with the shorter path length comes out of the stretcher earlier than the one with a longer length leading to a stretched pulse. The amount of stretching that occur can be determined equation 3.15:

$$L_s = 4f - L_{sg} \tag{3.15}$$

where L_{sg} is the stretcher grating separation and f is the focal length.

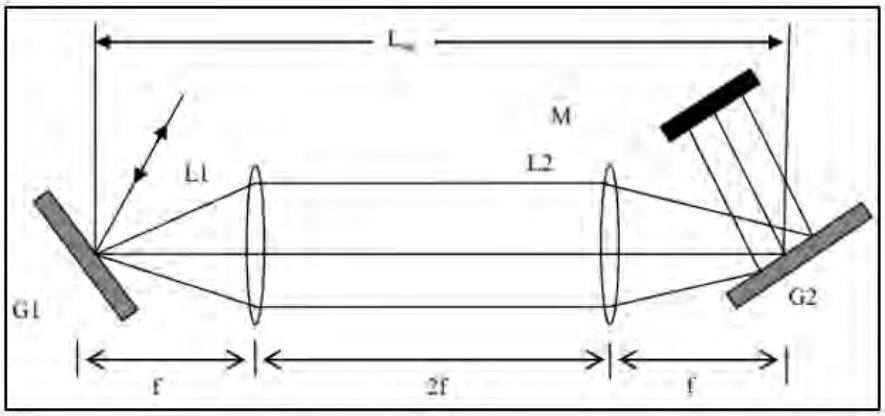

Figure 3.14: *Schematic diagram of grating-pair arranged such that they give positive dispersion. G_1 and G_2 are diffraction gratings, L_1 and L_2 are lenses separated by twice their focal lengths, and M mirror [3.27].*

3.5.3 Amplification

Once stretched, laser pulses can then undergo amplification without the risk of damaging the optics or active medium. Regenerative and multipass amplifiers are two most commonly used amplifiers.

In solid-state lasers, regenerative amplifier is the preferred technique for the generation of microjoule and millijoule energy ultra-short pulses [3.28]. This is done by injecting and trapping the low energy stretched pulses in the laser cavity using fast-switching Pockels and thin film polarizer [3.25]. This is done by stepping the voltage in two stages. Firstly, the stepping is by a quarter of wavelength. This is done to trap the pulse in the amplifier. Secondly, the stepping is by half a wavelength, this is done to eject the pulses from the amplifier. The energy of the pulses that can be obtained by using the regenerative amplifier is in the order of millijoules [3.20]. Figure 3.15 is a schematic diagram showing the workings of a regenerative amplifier.

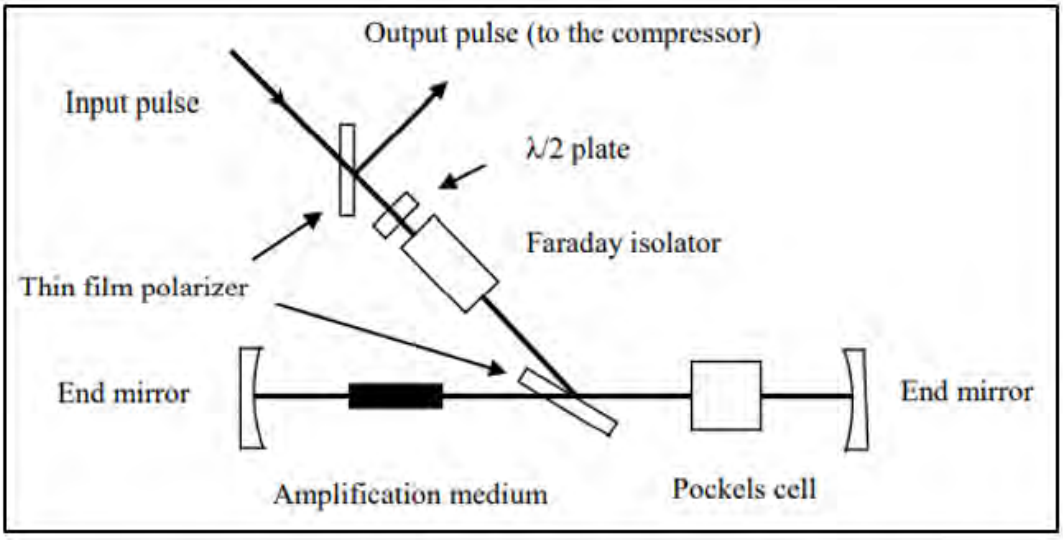

Figure 3.15: *Schematic diagram of regenerative amplifier [3.25].*

To amplify the laser pulses even further, multipass amplifiers, shown in figure 3.16, are used. In the case of multipass, the laser pulse passes through the medium multiple times without being trapped inside the cavity. The multipass amplifier is however less efficient when compared to regenerative amplifier. This is because of an overlap in pump-signal overlap. The pump-signal changes as the pulse through the gain medium in order to extract beam by separating it spatially [3.27].

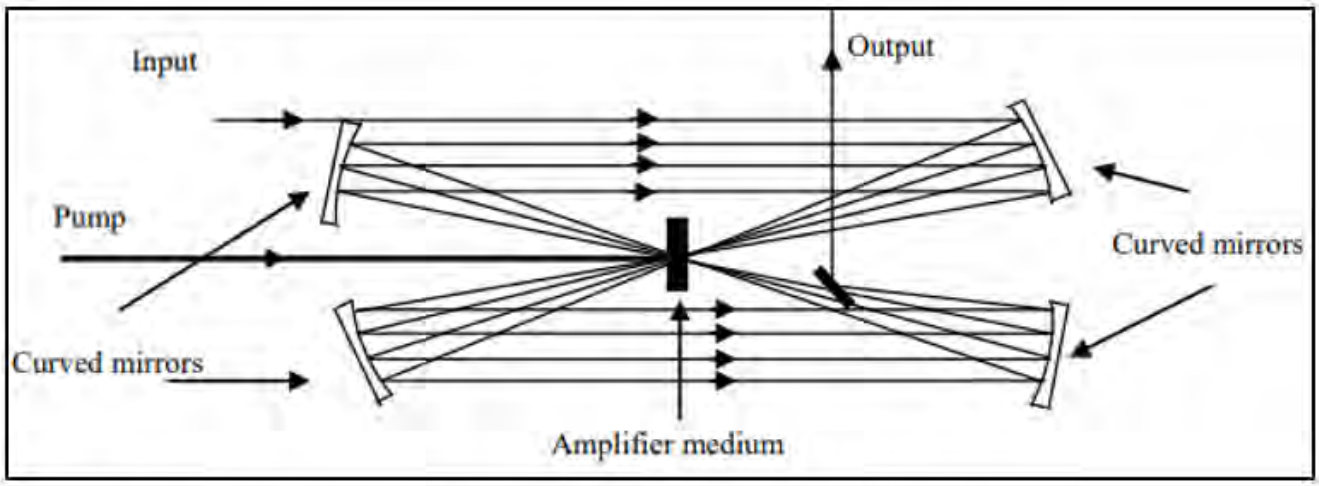

Figure 3.16: *Schematic diagram of a multipass amplifier [3.25].*

3.5.4 Compressor

Compression is the final stage of CPA. To achieve pulse compression, grating pair which are similar to those used in stretching are used. The difference is that the gratings are arranged in such a way that they give opposite dispersion as can be seen in figure 3.17. The amount of compression that occurs is a function of grating separation i.e. (L_c).

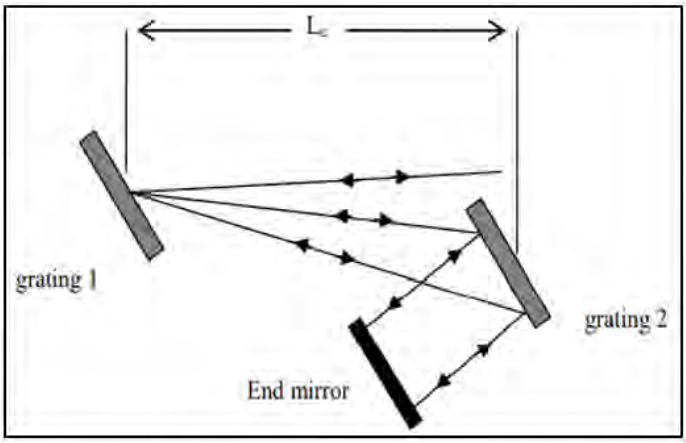

Figure 3.17: *Schematic diagram of the arrangement of grating pair for pulse compression during CPA process [3.27].*

3.5.5 In situ Femtosecond Laser RBS Annealing experimental setup

Zn-Sn bi-metallic thin film were subjected to non-isothermal annealing using femtosecond laser. This heating was done in the RBS chamber pumped down to a base pressure of 1×10^{-5} mbar, the collimating pin hole in front of the sample was set to 0.7 mm diameter. The train of energetic photons from the laser source were focused using a Mitutoyo apochromatic NIR objective lens with a working distance of 30.5 mm. The net-fluence of the focused laser was calculated from the selected power output of the laser. The station for the laser setup is as shown in figure 3.18 and the parameters of the laser used are shown in table 3.1.

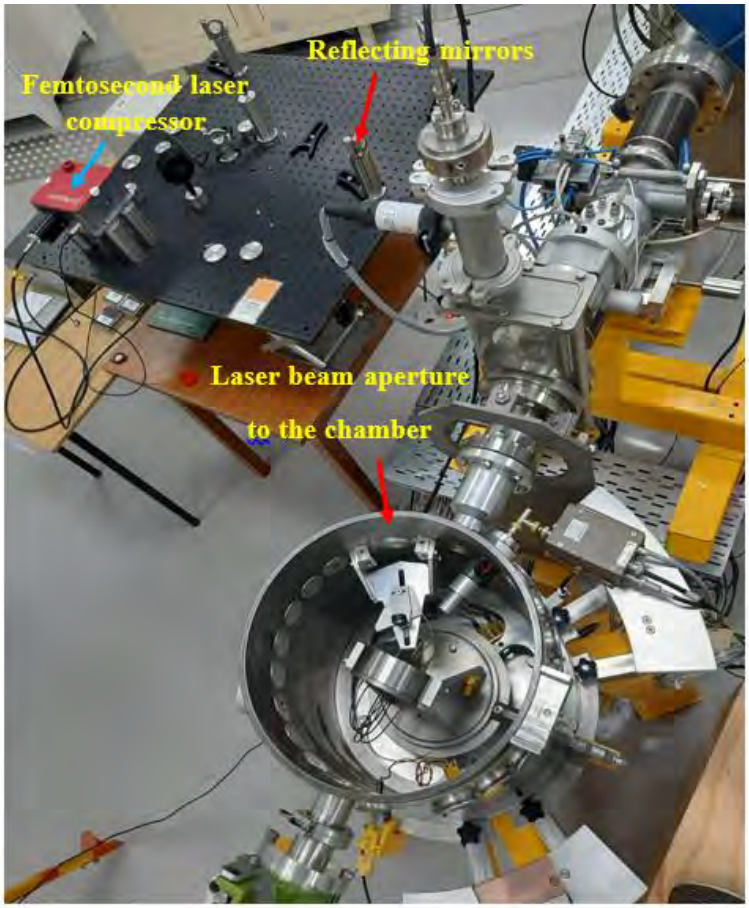

Figure 3.18: *Experimental station setup for the laser-RBS measurement.*

Table 3.1: *Laser parameter of the femtosecond laser used.*

Parameters		
Wavelength	Λ	1064 nm
Pulse duration	T	120 fs
Repetition rate	R	200 kHz
Maximum pulse energy	E	90 Nj
Beam quality factor	M^2	1.2
Spot size	d_f	0.7 mm

The focused laser spot was aligned with the RBS beam on the sample stage, such that the photons from the laser and the alpha particles from the tandetron accelerator overlap on top of each other as shown in figure 3.19. This was done in order to only probe (*with RBS*) the part of the sample that was heated by the laser.

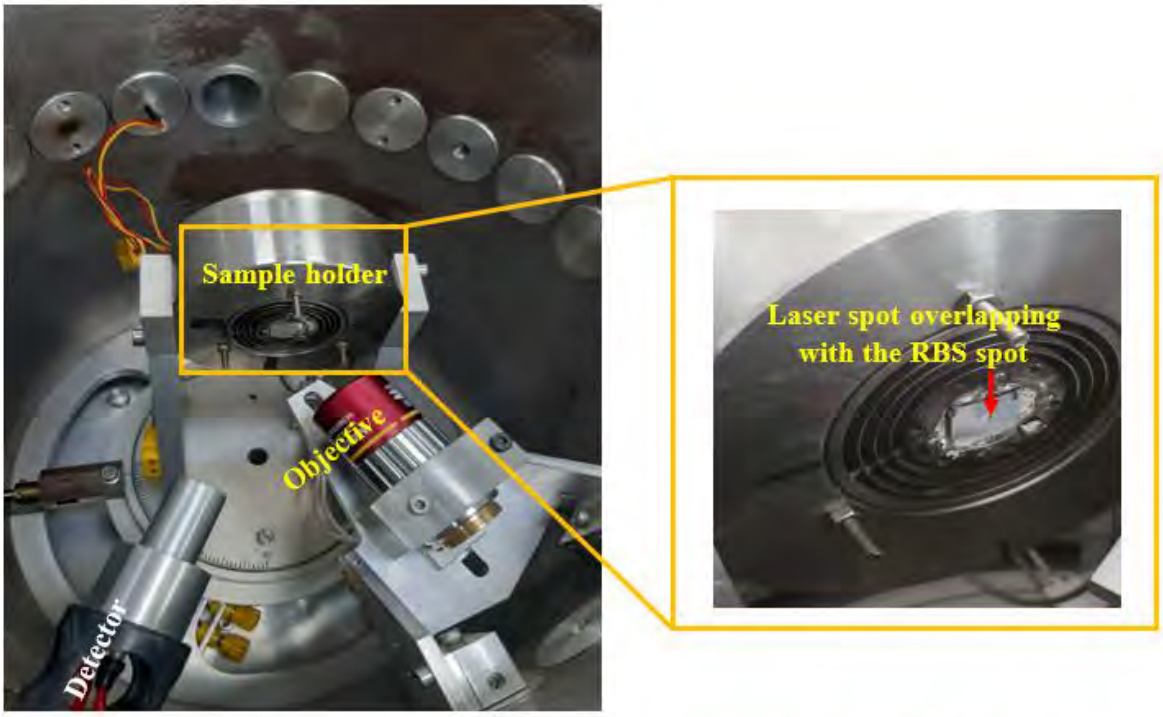

Figure 3.19: *Alignment of laser with alpha particles inside RBS chamber.*

In this set up, energetic photons from a laser source are used to heat the bi-metallic thin film, the heating process when photons interacts with the samples is non-isothermal in nature. The electrons are first to absorb the heat, and the lattice gets heated after the electrons have relaxed from the heat. This heating is different from the isothermal heating.

3.6 Scanning electron microscopy (SEM)

Scanning electron microscopy (SEM) is a technique that is used to study surface morphology, topography, chemical composition, and orientation of grains by producing images of the surface of the material [3.29]. The image of the surface is produced by scanning it with a highly

focused beam of electrons. Figure 3.20 below is a schematic diagram of SEM showing it basic components.

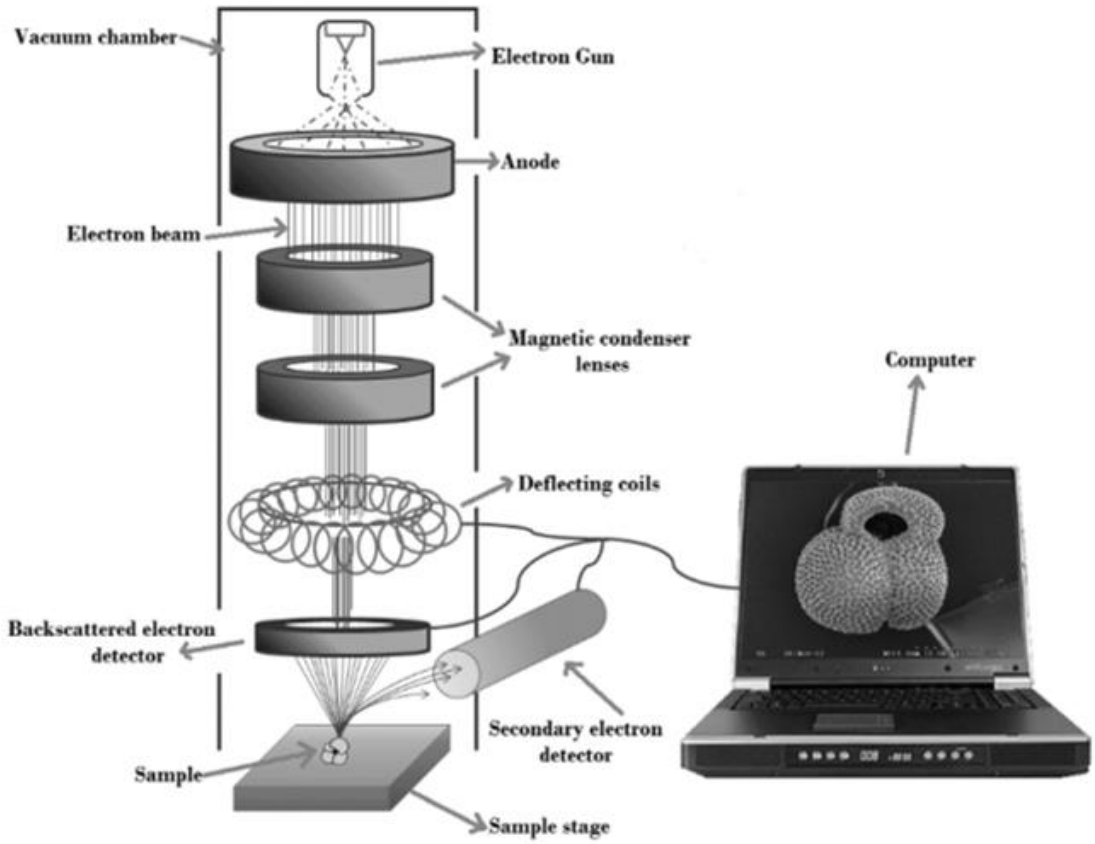

Figure 3.20: *Schematic diagram showing the components of scanning electron microscopy [3.30].*

Electrons are produced by a field emission gun using a solid-state emitter. The electrons generated are then accelerated toward the anode with energy of between 0.1- 30 KeV [3.31]. The diameter of the electron beam produced is too large to be used in producing high resolution images. For that reason, electromagnetic lenses and apertures are needed to focus the electron beam to a smaller spot size [3.31].

The first of these lenses is the condenser lens (*see figure 3.20*). The condenser lens, this consists of two iron poles pieces in which there is a copper winding to provide the magnetic field. It is this magnetic field that focuses the beam of electrons [3.31]. Figure 3.21 below shows the electron beam travelling through the condenser lens.

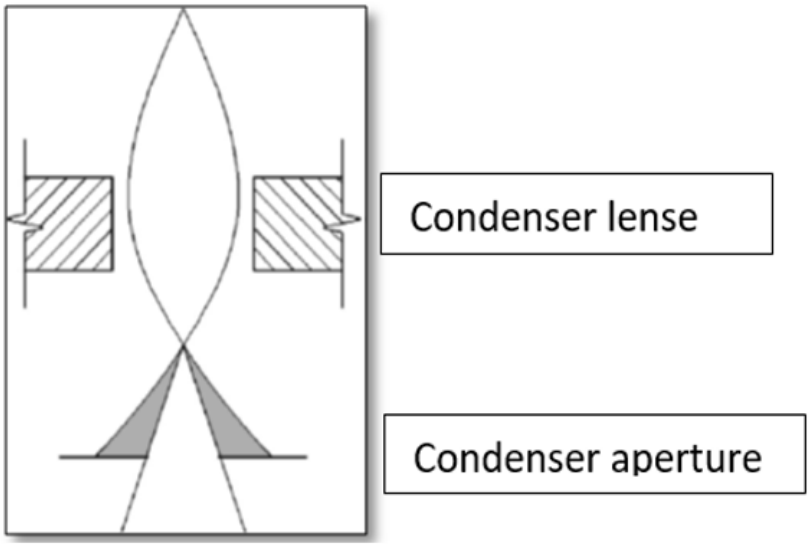

Figure 3.21: *Schematic diagram of incident electron beam passing through condenser lenses [3.31].*

Below the condenser lens is the objective lens. This focuses the electron beam on the sample surface and provides further demagnification [3.31].

SEM is based on the interaction of the electron beam with the sample [3.32]. The interaction between the electron beam and the sample can be elastic or inelastic depending on whether energy is lost during the interaction or not. When no energy is lost, the interaction is said to be elastic and when the energy is lost the interaction is said to be inelastic.

When the electron beam impinges on the surface of the sample, a variety of emission can be produced, these include secondary electrons, backscattered electrons, Auger electrons, X-rays and Cathodoluminescence [3.33]. Figure 3.22 below shows some of the emissions that can be produced as a result of an interaction between the primary beam and the surface of the sample.

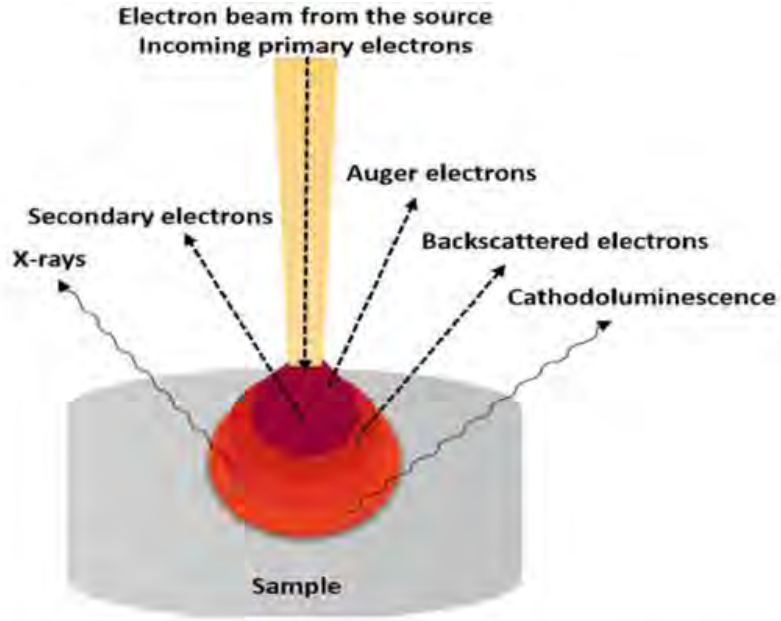

Figure 3.22: *Schematic diagram showing interaction between sample and the incident electron beam and the emissions that form [3.29].*

Of these emissions, it is the secondary electrons and backscattered electrons are mostly used to produce images [3.29].

Secondary electrons are low energy electrons that form because of inelastic collision between incident electron beam and the electrons of the sample [3.34]. Being low energy (<50 keV), these electrons only penetrate the sample to within nanometres of the surface [3.34]. As a result, secondary electrons are useful in providing topographic information about the sample [3.34].

Backscattered electrons are electrons that are reflected when the incident electrons are reflected upon hitting the sample. These results from inelastic collision between the incident electron beam and the nucleus. Backscattered electrons are high energy electrons and as a result penetrate the sample deeper that does secondary electrons. Backscattered electrons are useful in providing compositional and topographical information about the sample. Backscattered electrons give different contrast between areas with different chemical composition [3.35]. Elements with higher atomic number appear brighter than those with low atomic number.

The incident electron beam can be absorbed by the sample, the electrons that are absorbed are called primary electrons. Absorption of these electrons lead to the excitation of the electrons within the sample. When these electrons undergo de-excitation, x-ray is emitted. The x-ray is characteristic of elements present in the sample therefore these can provide compositional information [3.33].

3.6.1 Scanning Electron Microscopy experimental setup

The morphology of the thin films was characterized with field emission scanning electron microscope (SEM) using in-lens detector as a charge collector. The images were generated with a combination of backscattered and secondary electrons. The working distance for the imaging was set at 4.7 mm, with the electrons energized to 5 keV.

3.7 Atomic force microscopy

Atomic force microscopy (AFM) is a type of microscopy that is used to study the roughness of surfaces. Developed by Binning and others in 1986 [3.36], AFM falls under a family of microscopes known as Scanning Probe Microscopy (SPM). This group of microscopes also includes other techniques like Scamming Tunnelling Microscopy (STM), Scanning Force Microscopy (SFM) and Scanning near Field Optical Microscopy (SNFOM) [3.37].

AFM consists of a cantilever with a sharp probe at the end as can be seen in figure 3.23 below. The cantilever can be made up of silicon (Si) or silicon nitride (Si_3N_4). The sharp probe at the end of the cantilever is used to scan the surface of the sample to generate a 2D or 3D topographic image of the sample. The probe is placed closed to the surface of the sample and the sample is scanned while the force between the surface and the probe remains constant.

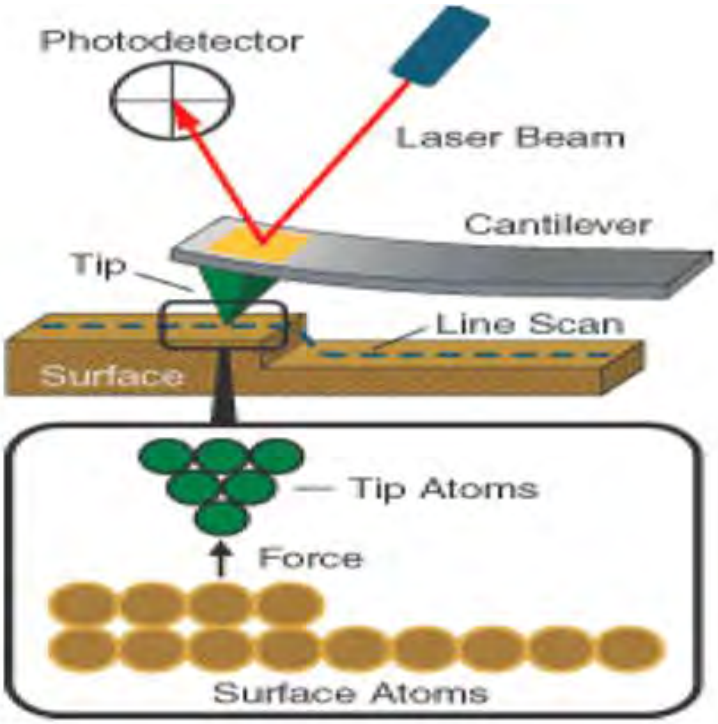

Figure 3.23: *Schematic diagram of atomic force microscopy [3.38].*

A laser beam is focused on the back of the cantilever (*see figure 3.23*). This beam is reflected to the detector where it is converted to electrical charge.

During operation, the cantilever is in contact with the sample and as it moves, the scanning of the surface occurs. This changes the direction of laser light which in turn changes the amount of light going to the detector.

3.7.1 Mode of Operation

Atomic force microscope can be operated in one of two modes i.e., contact mode or tapping mode. When operated in contact mode, there is a constant contact between the probe tip and sample. This contact is maintained by a feedback control. In the contact mode, image is constructed based on the deflection required to keep the force constant.

When AFM is operated in the tapping mode, the tip of the cantilever comes into contact with the surface of the sample for a short period of time. In this mode, the cantilever vibrates at its resonance frequency and as it comes into contact with the sample, the oscillation is affected by

this interaction. This leads to the z-axis of the piezoelectric scanner being adjusted with the voltage so that the pre-set amplitude of oscillation is maintained. Image and height of the surface are created based on this voltage.

3.7.2 Atomic force microscopy experimental setup

The surface morphology of the Zn-Sn thin films was studied with Veeco Nanoman V AFM. The AFM operated in the tapping mode with a resonance frequency of 50 kHz and the scan rate of 0.8 Hz. A silicon nitride cantilever with a silicon (Si) tip and a spring constant of 0.34 N/m was used. The images where collected in a scan area of 10 μm × 10 μm.The collected images where then analysed with NanoScope analysis software.

3.8 Phase formation

Real time RBS can be used to study and follow phase formation in real time. For phase transformation to occur in solids, an external stimulus for example heat must be applied for diffusion to occur. The process of diffusion is fundamental to phase transformation [3.39]. Considerable effort has been put into understanding phase transformation in solid and especially in understanding which phase forms first and in understanding the sequence of phase formation thereafter [3.40]. Two models have been developed in this regard, the Walser-Bene [3.40] and Effective Heat of Formation model [3.41] respectively.

3.8.1 Walser-Bene Model

The Walser-Bene Model (W-B) was one of the first model used to predict the formation of the first phase in solid thin films. The rule with regards to the formation of the first phase was formulated based on the studies of metal-silicon couples [3.42] and it states as follows [3.41]:

"The first compound nucleated in planar binary reaction couples is the most stable congruently melting compound adjacent to the lowest-temperature eutectic on the bulk equilibrium phase diagram".

According to this model, nucleation favours congruently melting phase over non-congruently melting phases because of a higher energy barrier [3.43]. The W-B model was further extended and applied to metal-metal systems. The rule was thus restated as follows [3.43]:

"The first phase nucleated in metal-metal thin-film reaction is the phase immediately adjacent to the low-temperature eutectic in the binary phase diagram."

While the W-B was successful in predicting the formation of first phase, it did so without taking into consideration thermodynamics. The result of this failure is that the W-B does not take into consideration that other phases can form from a thermodynamic standpoint other than those predicted by the model [3.43]. As a result, the Effective Heat of Formation model (EHF) model was developed.

3.8.2 Effective Heat of Formation model

The Effective Heat of Formation model (EHF) combines thermodynamics and kinetics in evaluating phase formation in thin films. First proposed by Pretorius [3.44], this model has been applied to several systems including metal-metal, silicon-metal, and germanium-metal systems [3.45].

Changes in Gibbs free energy, given by equation 3.15, is the force that drives chemical reactions:

$$\Delta G^{\circ} = \Delta H^{\circ} - T\Delta S^{\circ} \tag{3.15}$$

where ΔH° is the change in enthalpy, ΔS° is the change in entropy and T is the temperature.

In solid state reactions, the value of $T\Delta S^{\circ}$ is small [3.46] and can therefore be ignored. The result is that ΔG° can be approximated with ΔH°.In the EHF model, the concentration of the elements that are involved at the growth interface is taken into consideration. Accordingly, the EHF model proposes that elements mix and interact at an effective concentration. This concentration could be different from the physical concentration at the interface [3.45]. As a result, the effective heat of formation $\Delta H'$can be calculated with equation 3.16 below:

$$\Delta H' = \Delta H^{\circ} \times \left(\frac{effective\ concentration\ of\ limiting\ element}{compound\ concentration\ limiting\ element}\right) \tag{3.16}$$

where $\Delta H'\ and\ \Delta H^{\circ}$ are effective heat of formation and heat of formation, both expressed in kJ per mole of atom.

The EHF can be used to predict phase formation if effective concentration of the reacting elements is known, these cannot be calculated directly [3.45].

It was shown by Brown et al. [3.44] that the activation energy for interdiffusion is directly proportional to the melting point of the solid. Activation energy (E_a) is related to the mobility of atoms. The smaller the activation energy, the greater the mobility of atoms. The greatest mobility of the atoms and the most effective mixing at the interface occurs at liquidus minimum [3.45]. Accordingly, the EHF rule for the formation phase can thus be stated as follows for metal-metal systems [3.47]:

"The first compound to form during metal-metal interaction is the phase with the most negative effective heat of formation at the concentration of the liquidus minimum of the binary system".

In recent times, a more general rule for phase formation that applies to both phase formation and phase decomposition was developed. This rule is stated as follows [3.46]:

"Phases will react with each other to form a phase, with a composition lying between that of the interacting phases, whose effective heat of formation, calculated at the concentration closest to that of the liquidus minimum within the composition range, is the most negative."

3.9 Reaction Kinetics Analysis

As previously stated, real time RBS is a non-destructive technique that can be used to study solid state reactions in thin films. When coupled with *in situ* annealing, real time RBS allows one to follow reaction in real time. By analysing the data obtained, it is possible to obtain parameters like activation energy (E_a) and diffusion coefficient (D).

The process of diffusion can occur through the lattice or through the grain boundaries. In the case of lattice diffusion, which is associated with a higher E_a,vacancies play a significant role in the movement of atoms. Grain boundary diffusion is associated with low E_a.

Growth of phases in thin films can be diffusion controlled or reaction control [3.45].For diffusion-controlled reaction that are thermally activated, the reaction rate is proportional to diffusion coefficient D [3.48] as shown by equation 3.17:

$$rate\ \alpha\ D\ \alpha\ exp\left(\frac{-E_a}{k_B T}\right) \tag{3.17}$$

where E_a is the activation energy,k_B is the Boltzmann's constant and T is the temperature in Kelvin.

Fisk's law, given by equation 3.18, is often used to describe the process of diffusion. This gives the relationship between the flux of atom (j_A) and the concentration gradient [3.49]:

$$j_A \approx -D_A^f \frac{dc_A}{dx} \tag{3.18}$$

where D_A^f is the diffusion coefficient of A.

The pre-exponential coefficient (D_0^f) and the activation energy (E_a), two important parameters for thermally activated reaction are related to the diffusion coefficient (D_A^f) by equation 3.19:

$$D_A^f = D_0^f exp\left(\frac{-E_a}{k_B T}\right) \tag{3.19}$$

3.9.1 Growth of a single phase

If the reaction of A and B to form A_mB_n, as shown by equation 3.20, is diffusion controlled, then the growth rate $\left(\frac{dx}{dt}\right)$ of A_mB_n can be determined:

$$mA + nB = A_mB_n \tag{3.20}$$

The increase in the thickness of A_mB_n is related to the fluxes of atoms j_A and j_B to the reaction interface where the compound A_mB_n is formed.For every mole of atom A that reaches the interface,$\frac{1}{m}$ moles of A_mB_n is formed.The growth rate ($\frac{dx_A}{dt}$) due to an influx j_A can be written as:The growth rate due flux of A and B respectively are given by equations 3.21 and 3.22 respectively:

$$\frac{dx_A}{dt} = \frac{|j_A|}{m} V_{A_mB_n} \tag{3.21}$$

Where $V_{A_mB_n}$ is the volume of 1 mole of A_mB_n molecules expressed in $\frac{cm^3}{mole}$.

Similarly,the growth rate of A_mB_n due to an influx of j_B can be expressed as:

$$\frac{dx_B}{dt} = \frac{|j_A|}{n} V_{A_mB_n} \tag{3.22}$$

where $V_{A_mB_n}$ is the volume of one mole of A_mB_n expressed in $\frac{cm^3}{mole}$

By combining equations 3.21 and 3.22, the growth rate due to both A and B can be obtained by equation 3.23:

$$\frac{dx}{dt} = \left(\frac{|j_A|}{m} + \frac{|j_B|}{n}\right) V_{A_mB_n} \tag{3.23}$$

Flux for individual particle can be obtained from the Nernst-Einstein equation 3.24:

$$j_i = -C_A \frac{D_A^{ne}}{k_B T} \frac{d\mu_A}{dx} \tag{3.24}$$

The chemical potential of each element of the growing layer is given by 3.25 and 3.26 respectively:

$$\Delta\mu_A = \frac{\Delta G_{A_mB_n}}{m} \tag{3.26}$$

where $\Delta G_{A_mB_n}$ is the change in Gibbs free energy for the formation of one molecule of A_mB_n

Substituting equation 3.24 into equation 3.23 we get equation 3.27:

$$\frac{dx}{dt} = \left(\frac{D_A}{m} + \frac{D_B}{n}\right)\frac{\Delta G_{A_mB_n}}{k_B T}\frac{1}{x} \tag{3.27}$$

The equation for growth rate can be rewritten in terms of interdiffusion coefficient D =$N_B D_A$ + $N_A D_B$, where $N_A = \frac{m}{(m+n)}$ and $N_B = \frac{n}{(m+n)}$ are the fractional concentrations of A and B in compound A_mB_n:

$$\frac{dx}{dt} = \frac{(m+n)^2}{mn}\frac{\Delta H_{A_mB_n}}{k_B T}\frac{D}{x} \tag{3.28}$$

The approach to second phase and phases subsequent thereafter is slightly different from the approach presented in the above section. Consider the formation of A_mB_n as a result of the reaction of B with compound A_pB_q as shown in equation 3.29:

$$mA_pB_q + (pn - mq)B \rightarrow pA_mB_n \tag{3.29}$$

The chemical potentials, $\Delta\mu_A$ and $\Delta\mu_B$, can be expressed as follows:

$$\Delta\mu_A = \frac{m+n}{m}\Delta H^R_{A_mB_n} \tag{3.30}$$

$$\Delta\mu_B = \frac{m+n}{n}\Delta H^R_{A_mB_n} \tag{3.31}$$

According to equation 3.29, the growth due to specific species can be expressed as follows:

$$dx_A = \left(\frac{pn}{pn-mq}\frac{|j_A|dt}{m}\right)V_{A_mB_n} \tag{3.32}$$

$$dx_B = \left(\frac{pn}{pn-mq}\frac{|j_B|dt}{n}\right)V_{A_mB_n} \tag{3.31}$$

Equations 3.32 and 3.33 can be combined to give the total growth rate:

$$\frac{dx}{dt} = \frac{pn}{pn-mq}\frac{(m+n)^2}{mn}\frac{\Delta H_{A_mB_n}}{k_B T}\frac{D}{x} \tag{3.34}$$

If q = 0, equation 3.34 reduces to 3.26 since the heat of reaction in this case is the heat of formation.

3.9.2 Determination of kinetics for Isothermal annealing

During isothermal annealing the temperature is constant. Integration of the growth rate equation i.e., equation 3.34 give rise to equation 3.35, this equation gives the relationship between thickness and time:

$$x^2 = \frac{pn}{pn-mq}\frac{(m+n)^2}{mn}\frac{\left|\Delta H^R_{A_mB_n}\right|}{k_BT}D(t-t_0) + x_0^2 \tag{3.35}$$

Equation 3.35 can be simplified to the phenomenological relation by defining $t_0 = 0$ [3.49]:

$$x^2 - x_0^2 = k_D t \tag{3.36}$$

where k_D is the reaction constant.

k_D can be related to diffusion coefficient through equation 3.37:

$$k_D = 2\frac{(m+n)^2}{mn}\frac{\left|\Delta H^R_{A_mB_n}\right|}{k_DT}D \tag{3.37}$$

By plotting ($x^2 - x_0^2$) against time, a straight line is obtained in which the slope is equal to k_D.The activation energy (Ea) and the pre-exponential factor are obtained from a plot of $ln(k_Dt)$ against $\frac{1}{T}$. The slope of this plot gives the Ea while the offset gives the D.

3.9.3 Determination of kinetics for ramped annealing

For ramped annealing, the temperature is increased at a constant rate which can be given by the following expression: $\rho = \frac{dT}{dt}$.

In such a case, both D and T are a function of time and the integration of equation 3.34 tells us how the thickness changes over. Integration of equation 3.34 is accomplished in the following way:

$$x^2 = 2\frac{pn}{pn-mq}\frac{(m+n)^2}{mn}\frac{\left|\Delta H^R_{A_mB_n}\right|}{k_B}\int_{t_0}^{t}\frac{D(T(t))}{T(t)}dt + x_0^2 \tag{3.38}$$

$$x^2 = 2\frac{pn}{pn-mq}\frac{(m+n)^2}{mn}\frac{\left|\Delta H^R_{A_mB_n}\right|}{k_B}\frac{D_0}{\rho}\int_{T_0}^{T}\frac{exp\left(-\frac{E_a}{k_BT}\right)}{T}dT + x_0^2 \tag{3.39}$$

$$x^2 \cong 2\frac{pn}{pn-mq}\frac{(m+n)^2}{mn}\frac{\left|\Delta H^R_{A_mB_n}\right|}{E_a\rho}T^2D_0\,exp\left(-\frac{E_a}{k_BT}\right)\Big|^T_{T_0} + x_0^2 \qquad (3.40)$$

Equation 3.40 may then be used to fit the data by varying the values of D, E_a and x_0 provided the thickness (x) is known as a function of temperature T [3.49].

3.8 References

[3.1] Lin, Y. ed., 2016. *Advanced Nano deposition methods*. John Wiley & Sons.

[3.2] Dopp, C.2007. *Design Modification of a High Vacuum Unit for Thin Film Formation by Electron Beam Evaporation*, Diploma *Thesis*, Savonm ia University of Applied Science.

[3.3] Cullity, B.D. and Stock, S.R., 1978. Elements of X-ray Diffraction, 2" edition. *Assison-Wesley publishing company, USA*.

[3.4] Mpanza, T., 2018. *Synthesis and characterization of tungsten oxide wo3 nanostructures thin films for gas sensing applications* (Doctoral dissertation, University of Zululand).

[3.5] Thabethe, T.T., 2017. *The interfacial reaction and analysis of W thin film on 6H-SiC annealed in vacuum, hydrogen and argon* (Doctoral dissertation, University of Pretoria).

[3.6] Serway, R.A. and Jewett, J.W., 2018. *Physics for scientists and engineers*. Cengage learning.

[3.7] Gegier, H. and Marsden, E., 1909. On a diffuse reflection of the α-particles. *Proceedings of the Royal Society of London. Series A, Containing Papers of a Mathematical and Physical Character*, *82*(557), pp.495-500.

[3.8] Chu, W.K., Mayer, J.W. and Nicolet, M.A., 1978. Backscattering Spectrometry (New York: Academic).

[3.9] Alfassi, Z. and Peisach, M., 1991. *Elemental analysis by particle accelerators*. CRC Press.

[3.10] Verma, H.R., 2007. *Atomic and nuclear analytical methods*. Springer-Verlag Berlin Heidelberg.

[3.11] Feldman, L.C., Mayer, J.W. and Grasserbauer, M., 1987. Fundamentals of surface and thin film analysis: North Holland, Amsterdam, 1986 (ISBN 0-444-00989-2). xviii+ 352 pp. Price Dfl. 125.00.

[3.12] Wang, Y. and Nastasi, M., 2011. Handbook of modern ion beam materials analysis. *MRS BULLETIN*, *36*.

[3.13] Rennie, J., Elliott, S.R. and Jeynes, C., 1986. Rutherford backscattering study of the photodissolution of Ag in amorphous GeSe2. *Applied physics letters*, *48*(21), pp.1430-1432.

[3.14] Theron, C.C., Mars, J.A., Churms, C.L., Farmer, J. and Pretorius, R., 1998. In situ, real-time RBS measurement of solid state reaction in thin films. *Nuclear Instruments and Methods in Physics Research Section B: Beam Interactions with Materials and Atoms*, *139*(1-4), pp.213-218

[3.15] Pondo, K.J., 2010. *In Situ Real-Time Rutherford Backscattering Spectrometry Study of Ni/Ge Interaction* (Doctoral dissertation, University of Zambia).

[3.16] Demeulemeester, J., 2010. Elemental diffusion in ternary silicide growth unraveled by in situ real-time Rutherford backscattering spectrometry and artificial neural network analysis.

[3.17] Theron, C.C., Lombaard, J.C. and Pretorius, R., 2000. Real-time RBS of solid-state reaction in thin films. *Nuclear Instruments and Methods in Physics Research Section B: Beam Interactions with Materials and Atoms*, *161*, pp.48-55.

[3.18] Ossi, P.M., Agarwal, N.R., Fazio, E., Neri, F. and Trusso, S., 2014. Laser-mediated nanoparticle synthesis and self-assembling. In *Lasers in Materials Science* (pp. 175-212). Springer, Cham.

[3.19] Shugaev, M.V., Wu, C., Armbruster, O., Naghilou, A., Brouwer, N., Ivanov, D.S., Derrien, T.J.Y., Bulgakova, N.M., Kautek, W., Rethfeld, B. and Zhigilei, L.V., 2016. Fundamentals of ultrafast laser–material interaction. *Mrs Bulletin*, *41*(12), pp.960-968.

[3.20] Liu, X., Du, D. and Mourou, G., 1997. Laser ablation and micromachining with ultrashort laser pulses. *IEEE journal of quantum electronics*, *33*(10), pp.1706-1716.

[3.21] Shaheen, M., Fundamental Studies of Femtosecond Laser Interactions with Solids and Their Applications to Laser Ablation Inductively Coupled Plasma Mass Spectrometry for Environmental Analysis.Ph.D Thesis, University of Windsor (2010).

[3.22] Patterson, F.G., Perry, M.D., Gonzales, R. and Campbell, E.M., 1990, May. Multiterawatt Nd: glass lasers based on chirped-pulse amplification. In *Femtosecond to Nanosecond High-Intensity Lasers and Applications* (Vol. 1229, pp. 2-18). International Society for Optics and Photonics.

[3.23] Hoffmann, E., Stephanowitz, H., Ullrich, E., Skole, J., Lüdke, C. and Hoffmann, B., 2000. Investigation of mercury migration in human teeth using spatially resolved analysis by laser ablation-ICP-MS Dedicated to Professor Dr. D. Klockow on the occasion of his 65th birthday. *Journal of Analytical Atomic Spectrometry*, *15*(6), pp.663-667.

[3.24] Geertsen, C., Briand, A., Chartier, F., Lacour, J.L., Mauchien, P., Sjöström, S. and Mermet, J.M., 1994. Comparison between infrared and ultraviolet laser ablation at atmospheric pressure—implications for solid sampling inductively coupled plasma spectrometry. *Journal of analytical atomic spectrometry*, *9*(1), pp.17-22.

[3.25] Cheriaux, G. and Chambaret, J.P., 2001. Ultra-short high-intensity laser pulse generation and amplification. *Measurement Science and Technology*, *12*(11), p.1769.

[3.26] Rudd, J.V., Korn, G., Kane, S., Squier, J., Mourou, G. and Bado, P., 1993. Chirped-pulse amplification of 55-fs pulses at a 1-kHz repetition rate in a Ti: Al 2 O 3 regenerative amplifier. *Optics letters*, *18*(23), pp.2044-2046.

[3.27] Backus, S., Durfee III, C.G., Murnane, M.M. and Kapteyn, H.C., 1998. High power ultrafast lasers. *Review of scientific instruments*, *69*(3), pp.1207-1223.

[3.28] Lenzner, M., Spielmann, C., Wintner, E., Krausz, F. and Schmidt, A.J., 1995. Sub-20-fs, kilohertz-repetition-rate Ti: sapphire amplifier. *Optics letters*, *20*(12), pp.1397-1399.

[3.29] Akhtar, K., Khan, S.A., Khan, S.B. and Asiri, A.M., 2018. Scanning electron microscopy: Principle and applications in nanomaterials characterization. In *Handbook of materials characterization* (pp. 113-145). Springer, Cham.

[3.30] Hussain, S., 2008. Investigation of structural and optical properties of nanocrystalline ZnO.

[3.31] Zhou, W. and Wang, Z.L. eds., 2007. *Scanning microscopy for nanotechnology: techniques and applications*. Springer science & business media.

[3.32] Schroder, D.K., 2006. Semiconductor material and device characterization, John Wiley&Sons. *Inc., Publication, Canada*, p.101.

[3.33] Ul-Hamid, A., 2018. *A beginners' guide to scanning electron microscopy* (Vol. 1, p. 402). Cham: Springer International Publishing.

[3.34] Kazmivuk, V. (2012). Scanning Electron Microscopy. Available at: www.intechopen.com/books/1505 (Accessed: 06/10/2021).

[3.35] Hafner, B., 2007. Scanning electron microscopy primer. *Characterization Facility, University of Minnesota-Twin Cities*, pp.1-29.

[3.36] Binning, G.Quate, C.F.Gerber, C.H. Atomic force microscope. Phys. Rev. Lett. 56 (9), (1986) 930.

[3.37] Bowen, R. and Hilal, N., 2009. *Atomic force microscopy in process engineering: An introduction to AFM for improved processes and products*. Butterworth-Heinemann.

[3.38] Vilalta-Clemente, A., Gloystein, K. and Frangis, N., 2008. Principles of Atomic Force Microscopy (AFM). *Proceedings of Physics of Advanced Materials Winter School*.

[3.39] Callister Jr, W.D., 2003. Recovery, Recrystallization, and Grain Growth. *Materials Science and Engineering, An Introduction, Sixth Edition, John Wiley & Sons*, pp.180-184.

[3.40] Walser, R.M. and Bene, R.W., 1976. First phase nucleation in silicon–transition-metal planar interfaces. *Applied Physics Letters*, *28*(10), pp.624-625.

[3.41] Baglin, J.E., Campbell, D.R. and Chu, W.K., 1984. Thin films and interfaces II.

[3.42Tsaur, B.Y., Lau, S.S., Mayer, J.W. and Nicolet, M.A., 1981. Sequence of phase formation in planar metal-Si reaction couples. *Applied Physics Letters*, *38*(11), pp.922-924.

[3.43] Bené, R.W., 1982. First nucleation rule for solid-state nucleation in metal-metal thin-film systems. *Applied Physics Letters*, *41*(6), pp.529-531.

[3.44] Brown, A.M. and Ashby, M.F., 1980. Correlations for diffusion constants. *Acta Metallurgica*, *28*(8), pp.1085-1101.

[3.45] Theron, C.C., *In situ, real-time characterization of solid-state reaction in thin films*.Ph.D Thesis, Stellenbosch University, South Africa, (1997)

[3.46] Pretorius, R., Marais, T.K. and Theron, C.C., 1993. Thin film compound phase formation sequence: An effective heat of formation model. *Materials Science Reports*, *10*(1-2), pp.1-83.

[3.47] Pretorius, R., 1990. R. de Reus, AM Vredenberg and FW Saris. *Mater. Lett*, *9*, p.12.

[3.48] Arrhenius, S., 1889. Physik Chem.4, 226

[3.49] Fick, A., 1855. V. On liquid diffusion. *The London, Edinburgh, and Dublin Philosophical Magazine and Journal of Science*, *10*(63), pp.30-39.

CHAPTER 4

Results and Discussion

4. Overview

In this chapter, the author will present the experimental results and discuss the observations using both imperial and analytical methods. As stated in **Chapter 1**, the overall aim of this research study was to compare isothermal annealing to non-isothermal annealing (*femtosecond laser*) of the zinc-tin (Zn-Sn) bilayer system.

Electron beam evaporation system (*e-beam)* was used to deposit thin films of tin (Sn) on borosilicate glass substrate, after which zinc (Zn) was deposited on top of Sn to form a metallic bilayer. This metallic bilayer was then subjected to isothermal annealing inside Rutherford backscattering spectrometry (RBS) chamber, the chamber was pumped down to a base pressure better than $5 \times 10^{-6}\ mbar$ prior to starting the experimental run. The annealing was carried out at a constant ramp rate of 2 ºC/min from room temperature to a terminal temperature of 350 ºC, this was done while the film was being probed with 3.045 MeV alpha particles. The experiment was carried out in real-time mode, with the spectrum collected every 30 s. Based on the colour coded contour plot obtained during the *in situ* RBS run, three temperature points were selected. Temperatures that were selected were 180 ºC, 200 ºC and 260 ºC, these correspond to start, middle and end of the reaction respectively. These temperatures were used to anneal pristine samples in the furnace in order to carry out complimentary characterization techniques to further study the samples in the temperatures of interest.

The pristine and annealed bi-metallic layered thin film samples were subjected to morphological characterization using scanning electron microscopy (SEM) and atomic force microscopy (AFM). The microstructure of the thin films was probed using X-ray diffractometer (XRD) in a θ - 2θ configuration.

The raw data from RBS, X-ray diffraction and atomic force microscope were analysed using SIMNRA, Origin and Nanoscope respectively.

4.1 Thin film deposition

Thin films of zinc (Zn) and tin (Sn) were deposited on a glass substrate using an electron beam evaporator. Targets of pure zinc and tin were loaded in their respective crucibles inside the electron beam chamber. The chamber was pumped down to a base pressure of 1×10^{-7} mbar. This was followed by de-gassing the targets to remove any desorbed atmospheric gasses from the target metals. Thin films were deposited when a tungsten filament was resistively heated, and thermionic electrons were emitted tungsten. These emitted electrons were used to heat up the target metals. The deposition rate of the metals was approximately 3 – 4 Å/s, and the thickness of the films were 50 nm each. Tin was deposited first onto a glass substrate, this was then followed by a layer of zinc.

4.2 Surface Morphology and microstructural studies

4.2.1. Pristine Films and metallic bilayer

The growth of thin film on a substrate can be described via one of three growth mechanisms that were discussed in **Chapter 1** which are *Volmer-Weber (V-W) [4.1], Frank-van der Merwe (F-M) [4.2]* and *Stranski–Krastanov (S-K)* [4.3]. Figure 4.1 below shows the scanning electron microscope micrograph of Sn thin film on a glass substrate. It can be observed from the micrograph that Sn film formed a closely packed cluster of islands on the substrate. During deposition of Sn layer, the glass substrate was at room temperature, therefore the grown film was under residual tensile stress [4.4], due to the temperature gradient between the incident Sn atoms and the cold substrate. Lattice mismatch between amorphous glass substrate and the incident hot Sn atoms could have likely contributed to the residual stress. As a result of this, cracks can be observed on the thin film due to the fore mention factors.

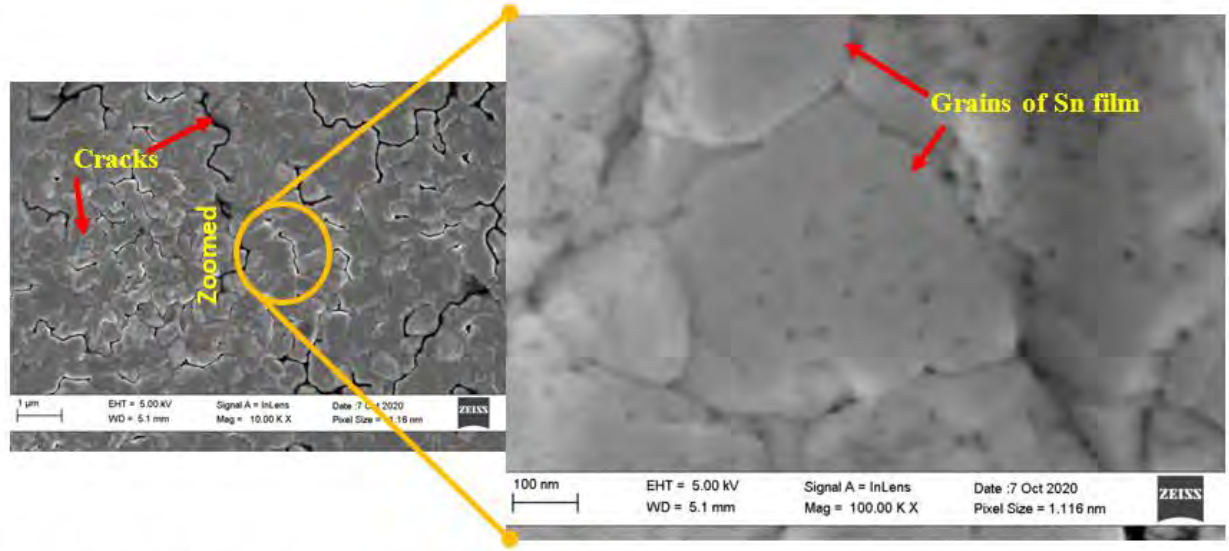

Figure 4.1: *Scanning electron micrograph of Sn film on a glass substrate deposited using e-beam evaporator.*

Based on what can be observed from the micrograph (*figure 4.1*), it can be suggested that the growth of Sn on glass follows Volmer-Weber (V-W) growth mechanism. As mentioned in **Chapter 1**, in V-W growth mechanism, adatom cohesive force is stronger than surface adhesive force. This leads to a higher probability of cracks forming. Having deduced from the SEM micrograph that the growth mechanism of Sn film on glass is V-W, it is expected that the film will be rough because of the cluster of islands of Sn.

The root mean square roughness (R_a) of the thin film was measured using atomic force microscopy (AFM) that was operated in tapping mode. Figure 4.2 below is an AFM micrograph of pristine Sn thin film on a glass substrate. The root mean square roughness (R_a) was measured and found to be 12.6 nm. This R_a value agrees with the R_a value of a typical film that follows V-W growth mechanism [4.5].

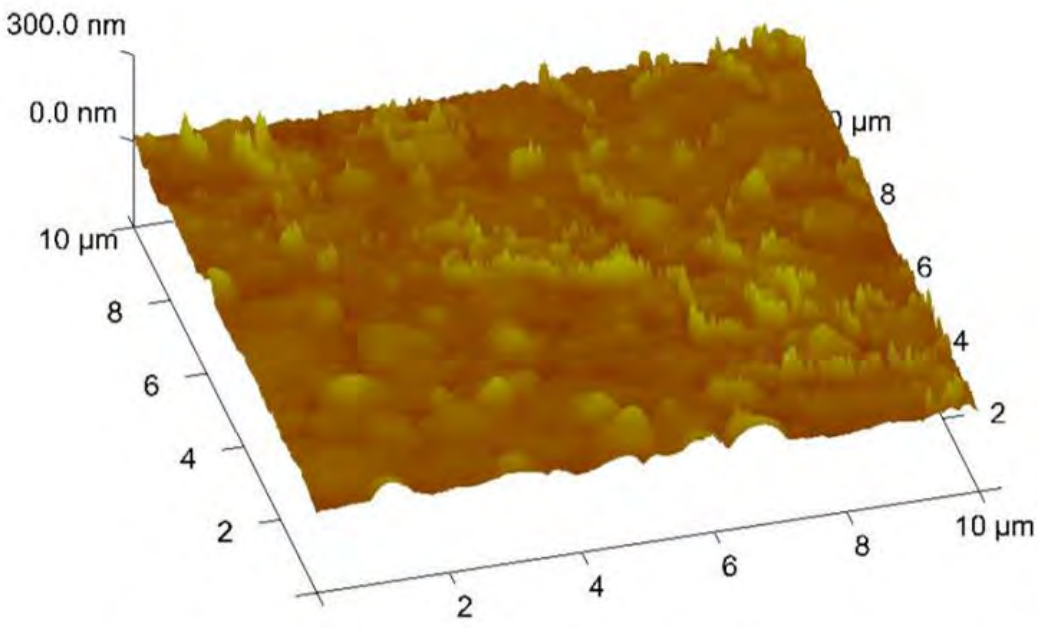

Figure 4.2: *AFM micrograph showing surface morphology of pristine Sn on a glass substrate.*

The microstructure of pristine Sn thin film was measured using x-ray diffraction technique (XRD), a D8 advanced Bruker diffractometer was used for this purpose. The diffractometer used monochromatic $K_{\alpha 1}$ copper as the X-ray source with wavelength of 1.54Å. The X-ray tube was operated with voltage and current of 40 kV and 40 mA respectively. Data was collected between 20^o and 90^o in 2θ, the step size and time for the measurement were 0.034 and 1s per step respectively.

From the x-ray diffraction pattern in figure 4.3, it can be observed that the film has crystalline microstructure due to sharp Bragg's diffraction peak. The film shows strong diffraction peak at 2θ = 30.7°, this Bragg peak belongs to the [200] lattice plane which is observed to be a preferential orientation. The other diffraction peaks at 2θ are used to confirm the crystal structure, which was confirmed to be body centered tetragonal crystal structure from the JCPDS card number 00-004-0673. The average crystal size of the film was calculated with the Debye-Scherrer [4.6] equation and found to be 431 nm.

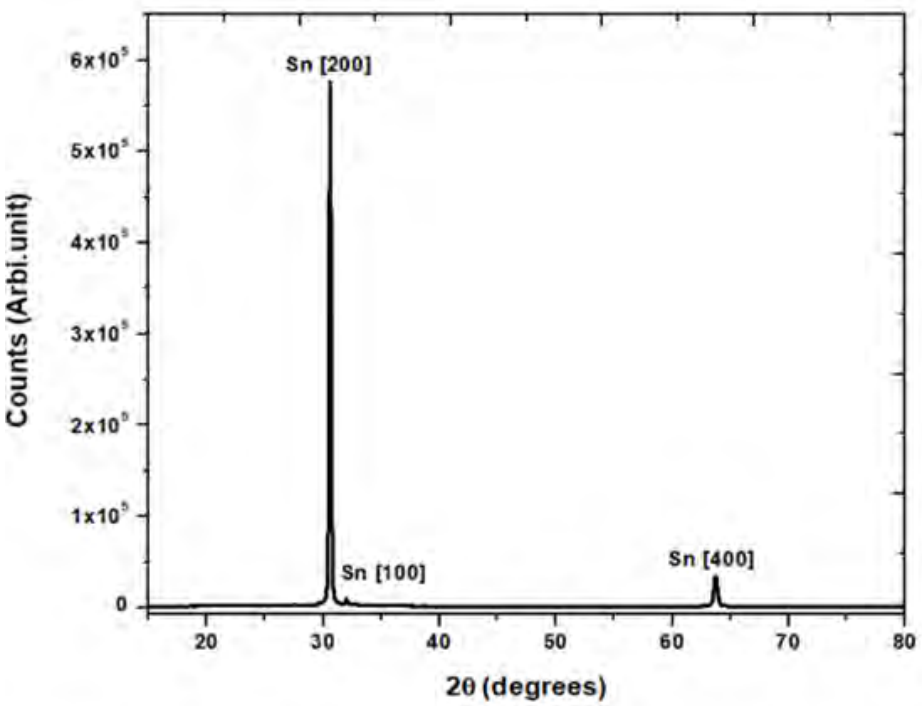

Figure 4.3: *XRD pattern of pristine Sn on a glass substrate.*

A thin layer of Zn of approximately 50 nm (as *measured from crystal monitor*) was deposited on a glass substrate using e-beam. The morphology of the film was characterized with scanning electron microscope (SEM) using in-lens detector as a charge collector. The image was generated with a combination of backscattered and secondary electrons. Figure 4.4 shows the SEM micrograph obtained. From figure 4.4, it can be observed that the film consists of distorted cuboid like structures and it is not homogenous.

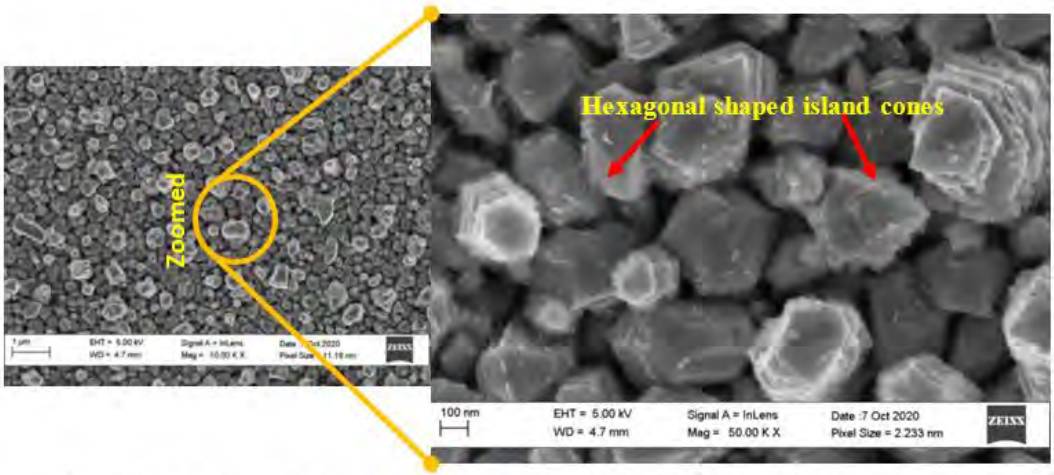

Figure 4.4: *Scanning electron micrographs of Zn thin film deposited on a glass substrate using electron beam evaporator.*

Based on what can be observed from the micrograph, the growth of Zn on a glass substrate can be suggested to be Volmer-Weber (V-W). This is due to cluster of islands observed and the separation of crystals, which is due to adatom cohesive force being stronger than surface adhesive force, hence the lack of homogeneity of the film. Atomic force microscope (AFM) was used to measure the root mean square roughness (R_a) and it was found to be 156 nm. Figure 4.5 shows the AFM image of pristine Zn thin film on a glass substrate.

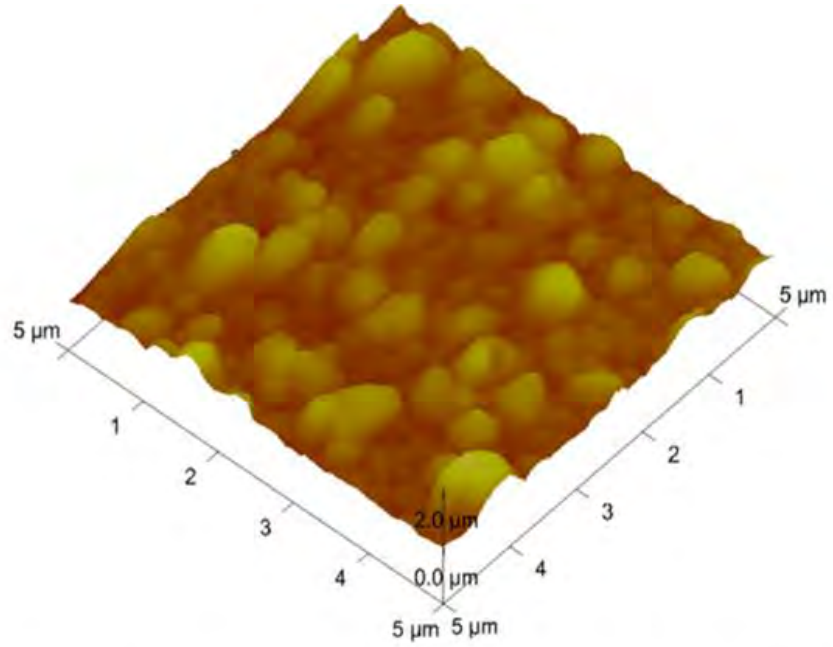

Figure 4.5: *AFM micrograph showing the surface morphology of pristine Zn on a glass substrate.*

The microstructure of Zn film was characterised using X-ray diffractometer in a θ - 2θ configuration, the film showed a strong Bragg's peak at 2θ = 36.4° as shown in figure 4.6 below. This peak correspond to the [002] lattice plane as recorded in the JCPDS card number 00-004-067. The average crystallites sizes in the film were calculated using the Deybe-Scherrer equation, the sizes were calculated to be 346 nm.

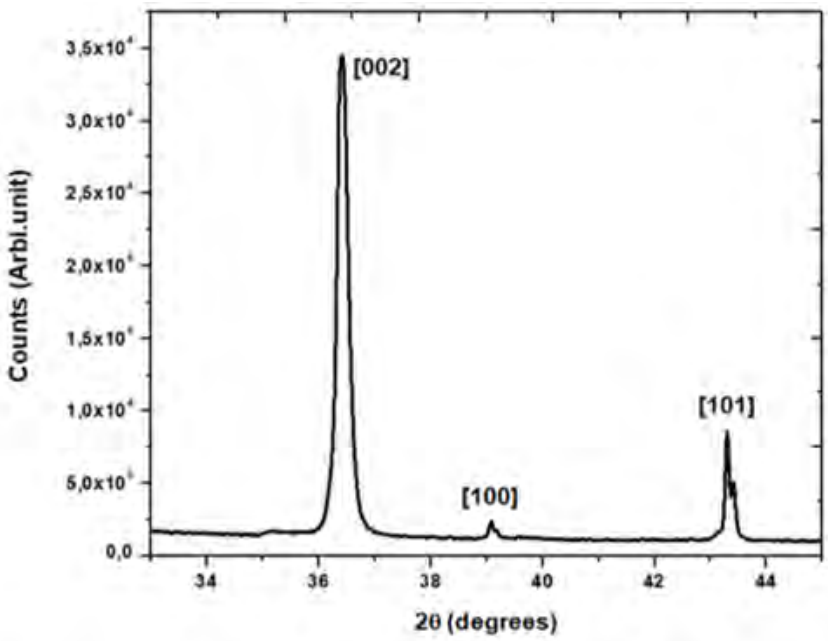

Figure 4.6: *XRD pattern of pristine Zn on a glass substrate.*

4.2.2 Metallic bilayer morphological and microstructural analysis

The surface morphology of the metallic bilayer (*50 nm of Zn deposited on top of 50 nm of Sn layer*) was characterized using scanning electron microscopy (SEM). The SEM micrograph is shown in figure 4.7. From the micrograph, it can be observed that the bilayer exhibited a closely packed cluster of crystallites with average size of 100 nm. It can also be observed from the micrograph, that the shape of the crystals is not discernible and cannot be put into a specific category of geometric shape.

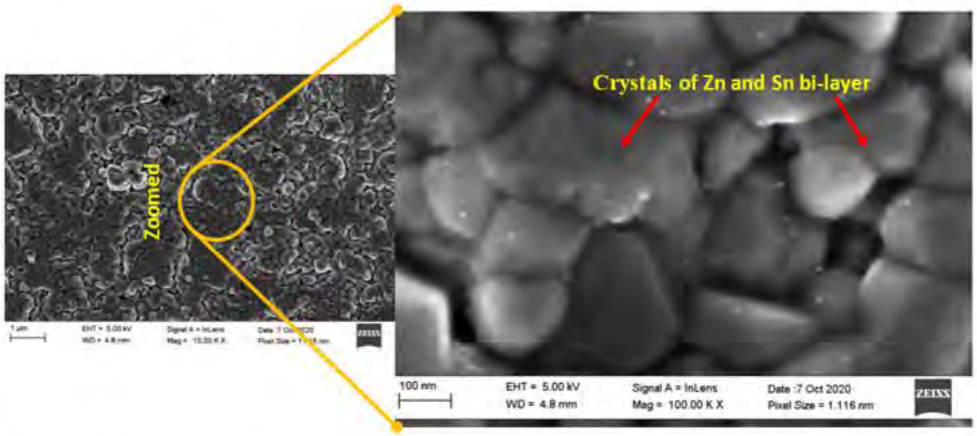

Figure 4.7: *Scanning electron micrograph of bilayer of Sn and Zn film on glass, deposited using e-beam evaporator.*

Taking into consideration the structures of pristine Sn and Zn in figure 4.1 and figure 4.4 respectively, there is a likelihood that Zn atoms filled the cracks that were observed on the Sn film. With Zn having a higher melting point (420 ºC) [4.7] than Sn (232 ºC) [4.8], the hotter atoms of Zn melt the top atomic layer of Sn. Because of this, partial mixing of the metals at the interface might have occurred. This mixing resulted in the irregular shape of the metallic bilayer that can be observed from the SEM micrograph. Additionally, the lattice parameters mismatch of Zn and Sn add to the residual tensile stress of the bilayer, which results in cracks and islands clusters. This can further be observed from figure 4.8, the AFM micrograph of the metallic bilayer in 3-D. The image shows the presence of cracks and cluster of islands. The R_a value for this bilayer was measured by AFM and was found to be 45.7 nm.

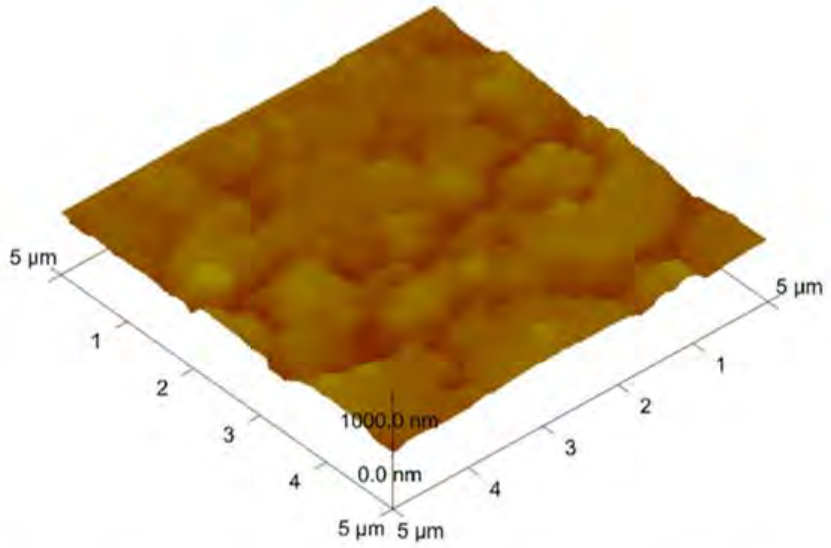

Figure 4.8: *AFM micrograph showing the surface morphology of pristine tin-zinc (Zn-Sn) bilayer on a glass substrate.*

The microstructure of pristine Zn-Sn film was characterized using x-ray diffractometer (XRD). Figure 4.9 shows the XRD patterns of pristine Zn-Sn thin films. The presence of more than one diffraction peak for both Sn and Zn suggests that the films are polycrystalline in nature. This is in agreement with the observations seen on the XRD patterns of pure Sn and Zn in figures 4.3 and 4.6 respectively. From figure 4.9 it can be seen that Sn film has a preferred orientation of [200] lattice planes with a diffraction peak centered at $2\theta = 30.7^{o}$. Zn is shown to have preferred orientation of [002] lattice plane, with the diffraction peak centered at around $2\theta = 36.4^{o}$. From the JCPDS card number 00-004-0673, Sn film has a body centered tetragonal crystal structure. On the other hand, Zn film was observed to have a hexagonal structure as deduced from JCPDS card 00-004-0831.

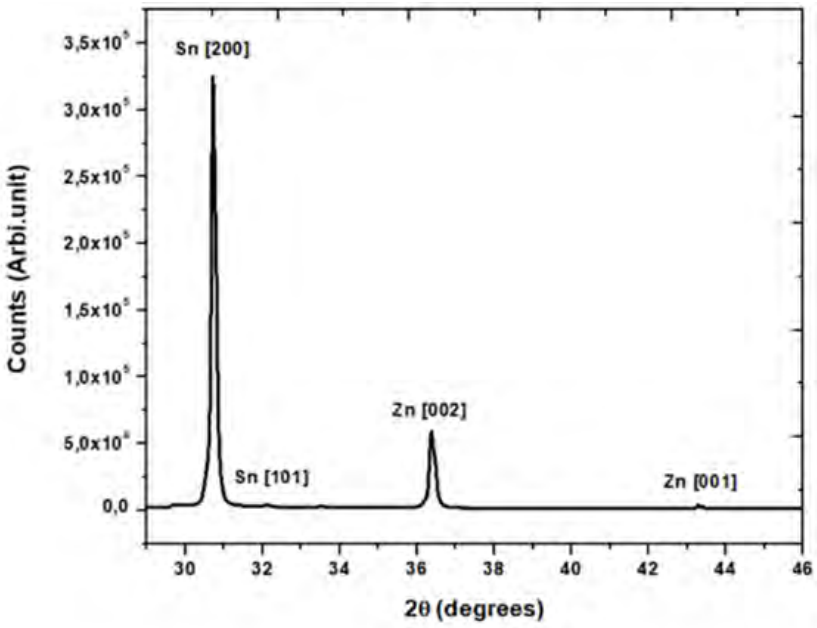

Figure 4.9: *XRD pattern of the as-deposited Zn-Sn bilayer.*

The Zn [100] lattice plane diffraction (*seen in figure 4.6*) is not observed in the metallic bilayer, this could be related to the low intensity of the peak. The intensities of the peaks of both Sn and Zn are reduced when compared to the peaks for the individual elements in figure 4.3 and figure 4.6, respectively.

4.3 Isothermal annealing of Zn-Sn metallic bilayer

4.3.1 In situ RBS study of bi-metallic layer

The Zn-Sn metallic bilayer was subjected to isothermal annealing inside Rutherford backscattering Spectrometry (RBS) chamber. The chamber was pumped down to a base pressure of $5 \times 10^{-6}\ mbar$ prior to starting the experimental run. The annealing was carried out at a constant ramp rate of 2 ºC/min from room temperature to a terminal temperature of 350 ºC, this was done while the metallic bilayer film was being probe with 3.045 MeV alpha particles.

Raw Rutherford backscattering raw data from the experiment was analysed with SIMNRA software in order to determine the thickness of the layers and to quantify the diffusion of the atomic species for depth profiling.

4.3.2 Introduction to RBS analysis

The analysis of the main RBS results will be presented in this section. However, it is necessary to introduce the relevant information that will become important in understanding the results that will be presented. Furthermore, information presented in this section provides reasons and support for selecting the annealing temperatures that were selected for annealing the sample in section 4.5 of this thesis (*vacuum annealing*).

The benefit of using in situ, real-time RBS in studying thin films have been given in the previous chapter. For example, it was mentioned that this technique combines both the depth profiling and compositional study capabilities of conventional RBS with *in-situ* annealing [4.9]. As a result, a single real-time RBS run can be used to study diffusion process in a quantitative way [4.10].This eliminates the risk of overlooking important stages in solid phase reaction [4.10]. Furthermore, because of depth information that can be obtained from this technique, it can be used in kinetics studies in order to obtain kinetic energies and pre-exponential co-efficient.

Figure 4.10a) and b) show the spectra of Zn and Sn respectively on glass substrate. The figures show the typical channel position that Zn and Sn respectively occupy when it is on the surface. The channel position for Zn and Sn are approximately 1450 and 1750 respectively. These positions will become relevant when looking at the spectra of Zn-Sn bilayer later and the shifts that occurs in the channel position.

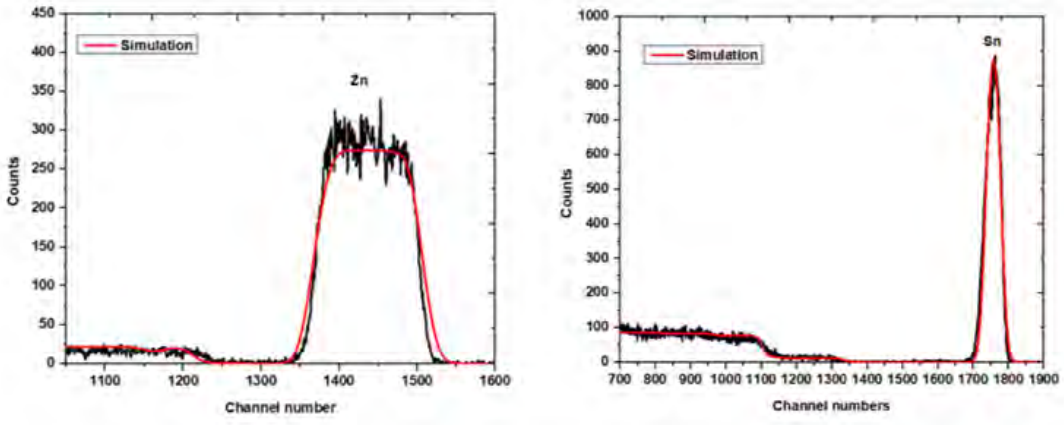

Figure 4.10: *a) Spectra of Zn on glass and b) Spectra of Sn on glass with simulation in red.*

When the film is made up of more than one element, particles scattered by the different elements form separate peaks [4.9]. As a result, the spectra of Zn-Sn bilayer shown in figure 4.11 below, has 2 separate peaks, one for Sn and one for Zn. The separation of these peaks is based on atomic numbers [4.11], with the element with a bigger atomic number, in this case Sn appearing on higher channels while Zn which has a smaller atomic number appears on lower channel. The position of Sn is however lower than the expected channel position of 1750 that is expected based on figure 4.10 (b).This is because of the Zn that is deposited on top of Sn which shift Sn to lower channel where compared to when it is on the surface.

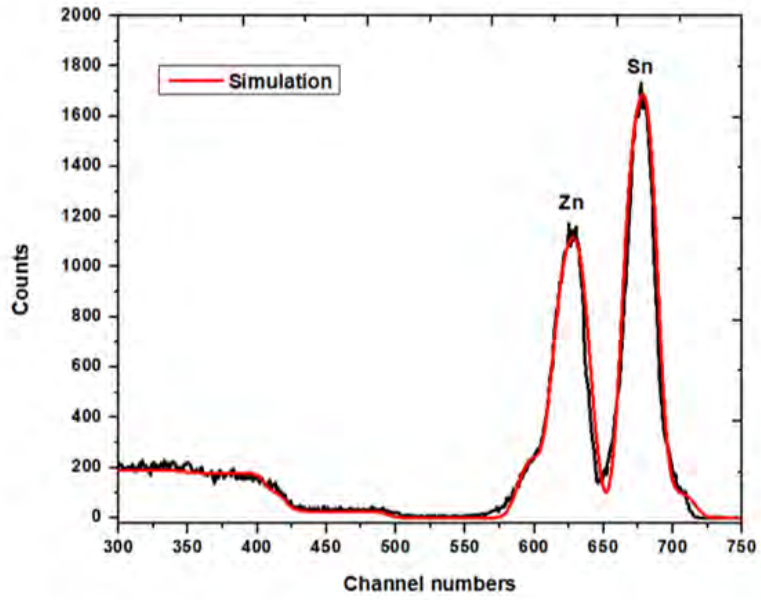

Figure 4.11: *Spectra of Zn-Sn bilayer spectra with simulation in red.*

A colour coded contour map plot of the experimental data is plotted as shown in figure 4.12, this can be divided into 3 zones.

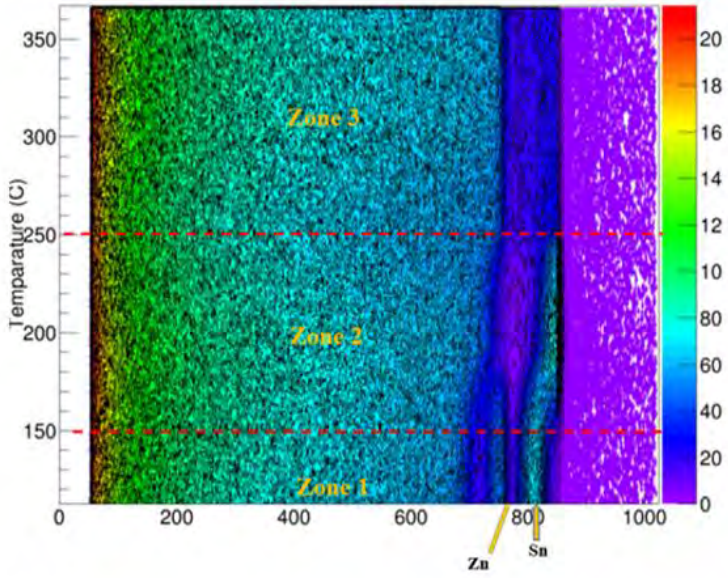

Figure 4.12: *Contour map plot of the experimental data of Zn and Sn bi-metallic thin film during in-situ RBS.*

Zone 1: It can be observed from the figure 4.12 that there is no change in the reaction of Sn and Zn within this temperature range. Both the Zn and Sn appear as straight line with Zn being dark purple in colour and Sn blue in colour (*yellow arrows*).

Zone 2: The colour of both Zn and Sn change slightly in this zone. Furthermore, there is a change in the shape of the Zn and Sn when compared to the straight line seen in Zone 1. This suggests that there is a reaction or intermixing between Sn and Zn within this zone. This will further be demonstrated later when spectra from this region are dealt with. It can also be seen that it is also from within this zone that Sn start to move to the surface or higher channel position as previously mentioned and becomes thin towards the end of this region while Zn almost completely disappears.

Zone 3: This zone corresponds to the end of the reaction as can be observed that both Zn and Sn were not negligible. However, when simulation with SIMRA where carried out for spectra within this zone Sn was present.

From the contour map in figure 4.12, regions of interest are clearly marked, this indicate the temperature where the diffusion and inter-mixing of the Sn atoms with Zn layer is taking place at the interface. The individual spectrum of the experiment in this temperature range are plotted in figure 4.13. The evolution of the Zn and Sn atoms migration is better seen through the peak width, height and shape of the peaks.

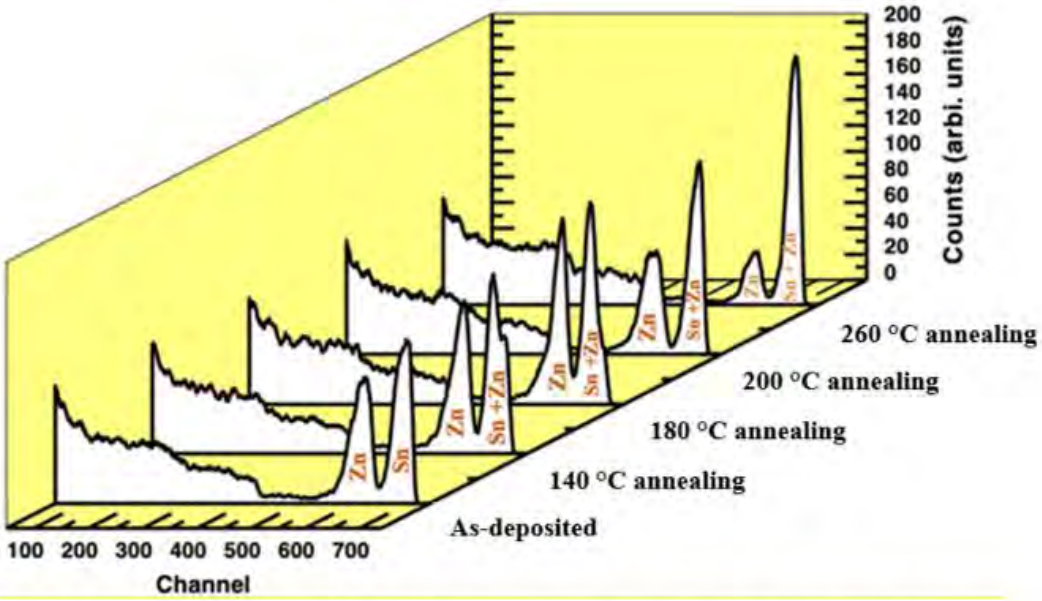

Figure 4.13: *3D plot of the RBS data of the bi-metallic film Zn and Sn in the temperature of interest.*

From figure 4.13, the spectra of the as-deposited film show the Sn and Zn speak, the Sn peak appear at a higher channel due to its heavier atomic number. As the temperatures reaches 140 ^{o}C, there is evidence of Zn atoms mixing with the Sn atoms at the inter phase of the films. This is observed from a shoulder that developed on the Sn peak, which is now labelled Sn + Zn. This inter-mixing and diffusion of the atoms plays out as in the evolution of the Sn and Zn peaks. At 260 ^{o}C, it appears that majority of the Zn atoms have diffused and evaporated off the sample, with only small amount of the Zn atom left in the sample.

Figure 4.14 show the spectra and simulation of the spectra in the region of interest, the rest are attached as **Appendix A**. Figure 4.14 a) is a spectra obtained at a temperature of 160 ^{o}C and corresponds to approximate the start of the reaction. Note the small shoulder indicated by the arrow, this was also seen in the figure 4.13.This shoulder is as a result of Sn moving to the surface it mixes with the Zn and thus the Sn layer get bigger. This could also be seen from the simulation of the spectra obtained at 160 ^{o}C, the thickness of the layer was found to be 504 and the concentrations of Zn and Sn were 0.81 and 0.18, respectively. Simulation of spectra corresponding to 165 ^{o}C yielded a thickness of 600 and the concentrations of Zn and Sn were 0.74 and 0.25, respectively.

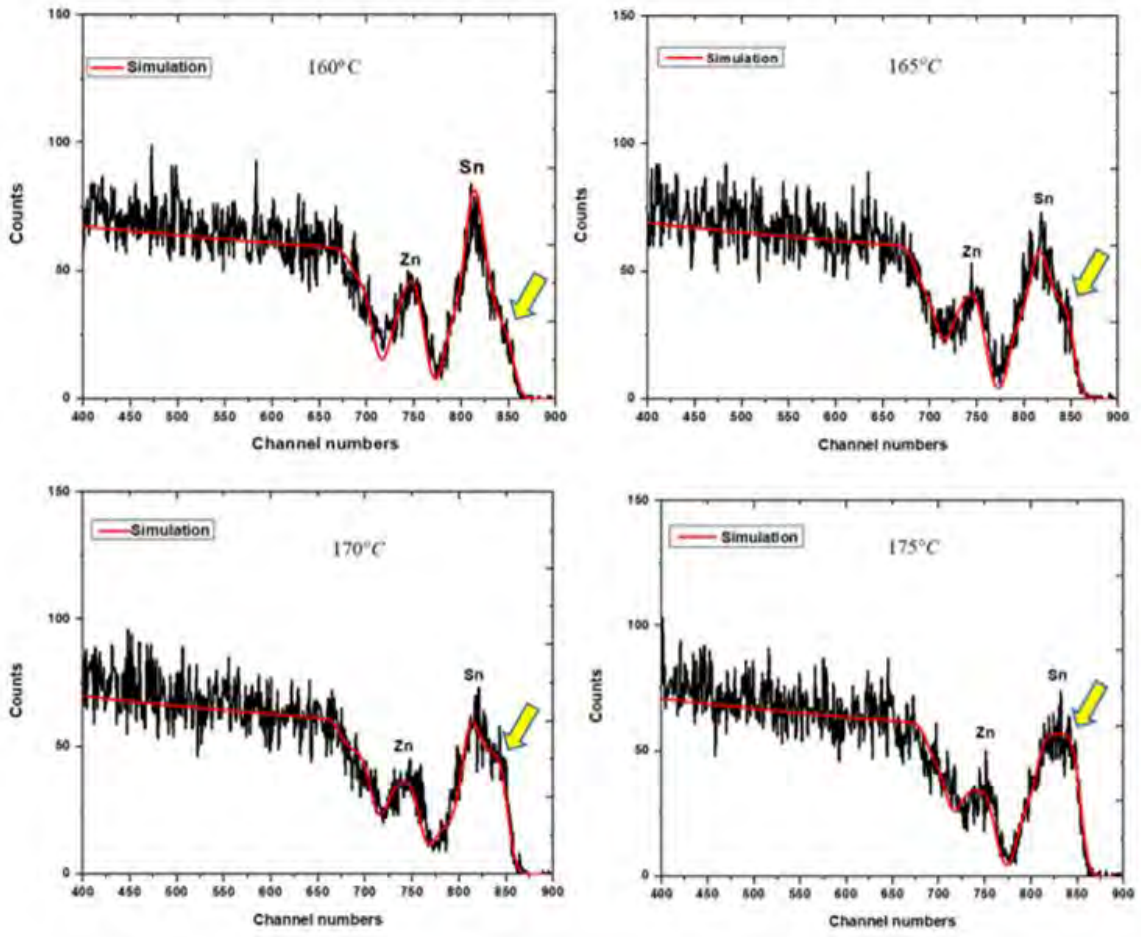

Figure 4.14: *In situ RBS spectra with simulation. Yellow arrow shows the evolution of the shoulder with temperature from 160 °C to 175 °C.*

Figure 4.15 shows the relationship between annealing temperature and the thickness of the layers. It can be observed that Sn and Zn follow almost a similar trend initially. However, Sn thickness increase sharply between the temperatures of 165 °C and 167 °C, thereafter the thickness remains relatively constant.

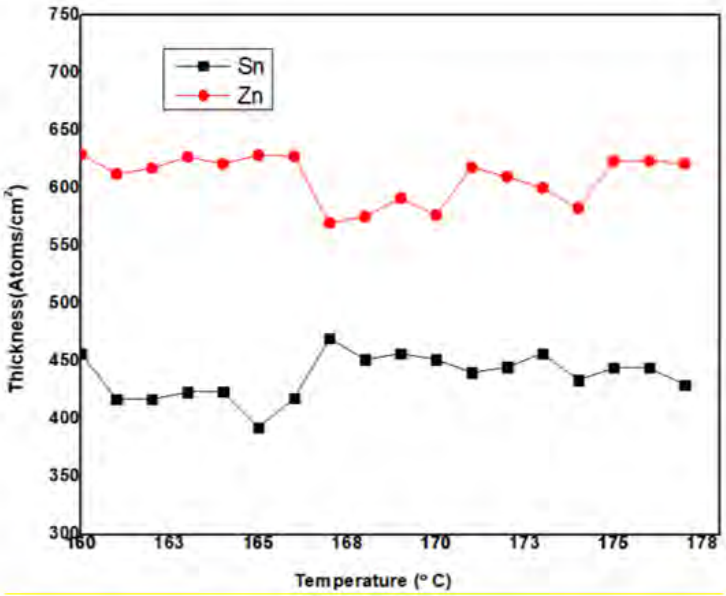

Figure 4.15: *Overview of the evolution of thickness during ramp annealing of Zn-Sn thin film from room temperature to 350 °C.*

4.3.3 Determination of Activation energy

The activation energy and the diffusion coefficient of the inter-mixing is calculated using Arrhenius [4.12] equation in it logarithmic form. Equation 4.1 and 4.2 below show Arrhenius equation and the logarithmic form of the equation respectively:

$$k = Ae^{\frac{-E_a}{RT}} \tag{4.1}$$

$$lnk = lnA - \frac{E_a}{R}\left(\frac{1}{T}\right) \tag{4.2}$$

where T is temperature (*in Kelvin*), E_a (*is Activation Energy*), R (*is gas constant*), and A (*diffusion coefficient*).

From the 1st order linear regression fitting of data points, the activation energy of the Zn and Sn atoms inter-mixing is 0.46 eV with the diffusion coefficient of 44.6 kJ/mol.The E_a obtain falls within the accepted range of between 41.0 kJ/mol - 45.0 kJ/mol [4.13] [4.14]

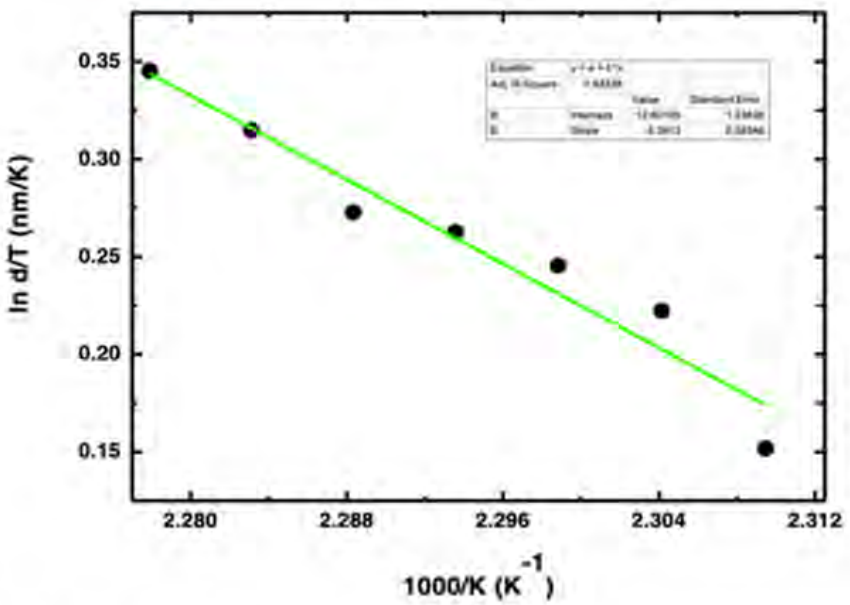

Figure 4.16: *Plot of logarithmic of the Arrhenius equation to determine the activation energy and the diffusion coefficient.*

From the RBS the experiment it seems that the Sn and Zn did not form an alloy but only inter-mixed, with the Zn atoms evaporating off the sample at higher temperatures. This is in agreement with the XRD results, which did not show any alloy formation of Zn-Sn.

4.4 XRD of in situ annealed Zn-Sn metallic bilayer

Tin-zinc metallic bilayer that was subjected to in-situ, real time RBS analysis was characterized with XRD. Figure 4.17 show the pattern that was obtained. There are 4 identifiable peaks in the pristine Zn-Sn film which are Sn [200], Sn [101], Zn [002] and Zn [101].

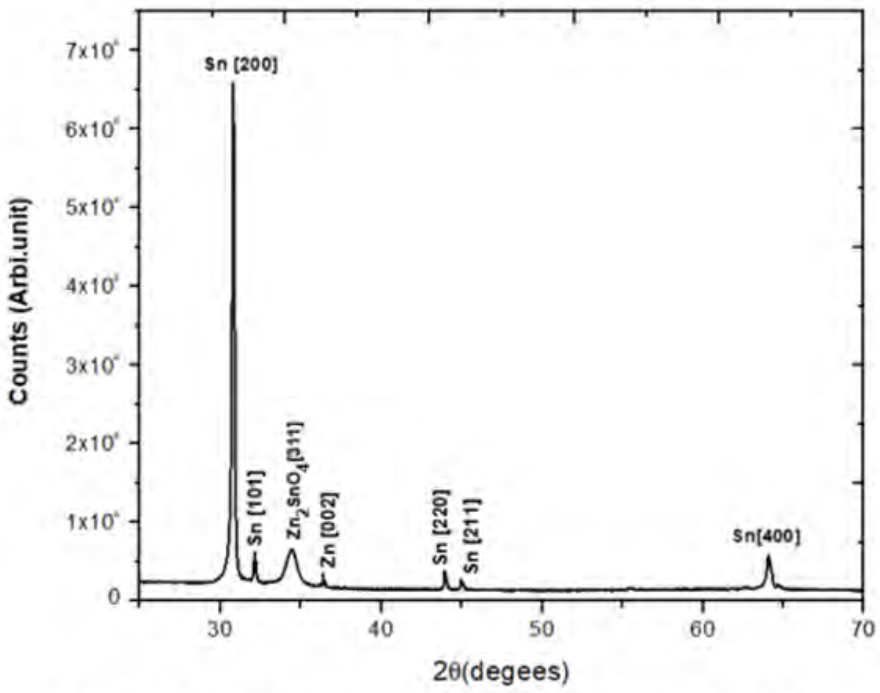

Figure 4.17: *XRD pattern of in situ, real time RBS thin film.*

In addition to the peaks that are seen in the pristine film (*figure 4.9*), the in-situ, real time RBS annealed film showed the presence of another peak. A $Zn_2SnO_4(311)$ peak evolved at 2θ = 34.290. This corresponds to FCC structure. The presence of this peak is from degassing of the chamber component at higher temperature.

4.5 Vacuum Annealed Metallic bilayer.

4.5.1 Morphological and microstructure Analysis of vacuum annealed Zn-Sn

The morphology and microstructure of vacuum annealed Zn-Sn thin films was studied with scanning electron microscopy (SEM), atomic force microscopy (AFM) and x-ray diffraction (XRD) respectively. Figure 4.18 shows the SEM micrograph of pristine thin film. The micrograph shows clear edges of the crystal clusters, with no evidence of any Sn tissue on the cracks as labelled in the figure. From this, it can be suggested that the Sn atoms start diffusing via the Zn cracks, this is seen well on the higher magnification micrograph. The edges of the Zn crystal are no longer sharp due to the presence of Sn atoms that diffused through, and start to interact with the Zn atoms. This observation is in agreement with the RBS simulated data, which show migration of Sn atoms.

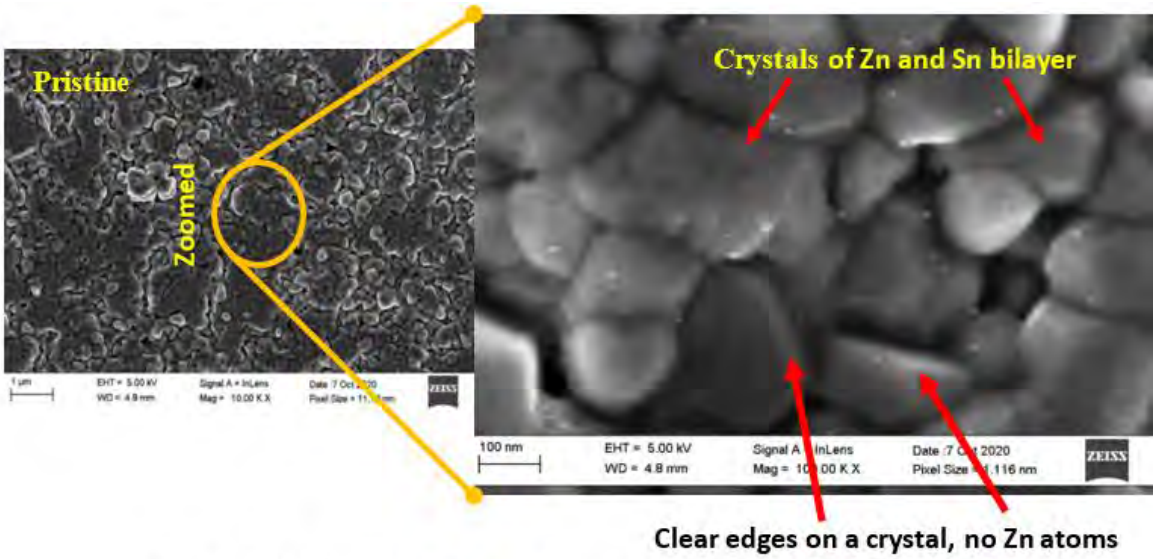

Figure 4.18: *Scanning electron micrograph of pristine Zn-Sn bilayer.*

SEM micrographs of samples annealed at 180 ºC, 200 ºC and 260 ºC are shown in figure 4.19 (a-c). These temperatures were chosen based on the contour plot obtained from the *in situ*, real time RBS as shown in figure 4.12, and they correspond to the start, middle and the end of the reaction, respectively. From the micrographs, it can be observed that the morphology of the sample has evolved due to annealing. The surface morphology of the pristine sample (figure 4.18), which had a layer of Zn on top, that had irregular shaped crystal, has a similar surface morphology to that of the sample annealed at 180 ºC (figure 4.19a). This observation supports the analysed data from the RBS simulation, which showed the diffusion of Sn atom at this temperature.

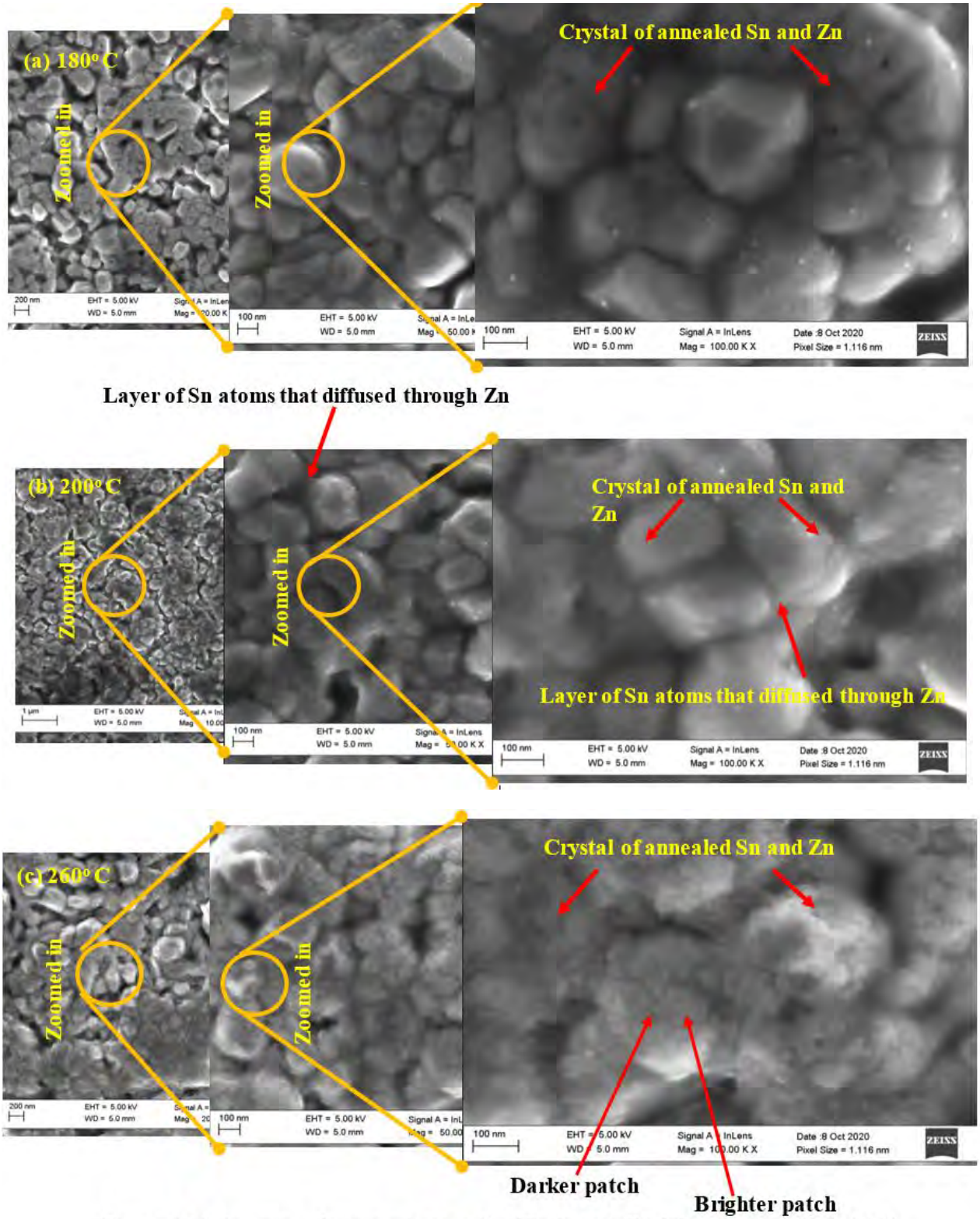

Figure 4.19: *Scanning electron micrograph of Zn-Sn metallic bilayer annealed at a) 180 °C, b) 200 °C and c) 260 °C.*

At the annealing temperature of 200 ºC, the SEM micrographs is now showing to have a layer of Sn atoms as shown in figure 4.19b. From the micrograph, it appears that the Sn atom first diffuse through the cracks of the top Zn layer.

At 260 ºC, there appear to be mixing of the Sn and Zn atoms, as seen from the morphology of the samples. The sharp edges of the crystal are visibly gone, with micrograph showing bright and darker patches, which in the electron microscopy infer to the difference on the atomic number, with heavier atomic number atoms appearing as darker, compared to the brighter low atomic number atoms. This confirms the diffusion of the Sn atom to the surface of the sample.

A cross-section view micrograph of the annealed samples are shown in Figure 4.20 (a-c), from the micrographs the interface between the Zn and Sn layers is not clearly visible. The 180 ºC and 200 ºC annealed samples exhibit a rough and conglomeration of the Zn and Sn atom into clusters, but for the 260 ºC annealed sample has a smoother appearing layer which is as a results of Zn and Sn mixing.

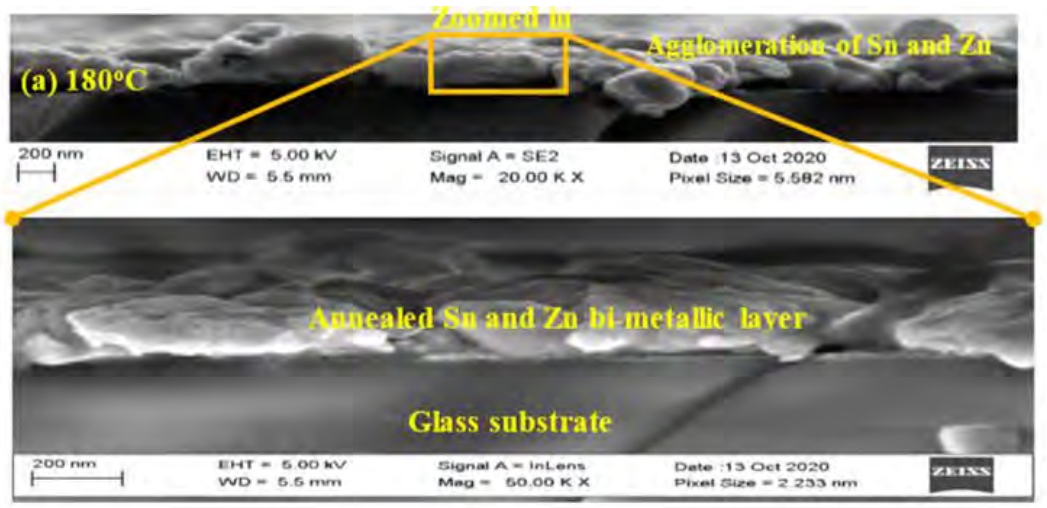

Figure 4.20: *a) Cross section view of micrograph of Zn-Sn bilayer annealed at 180 ºC*

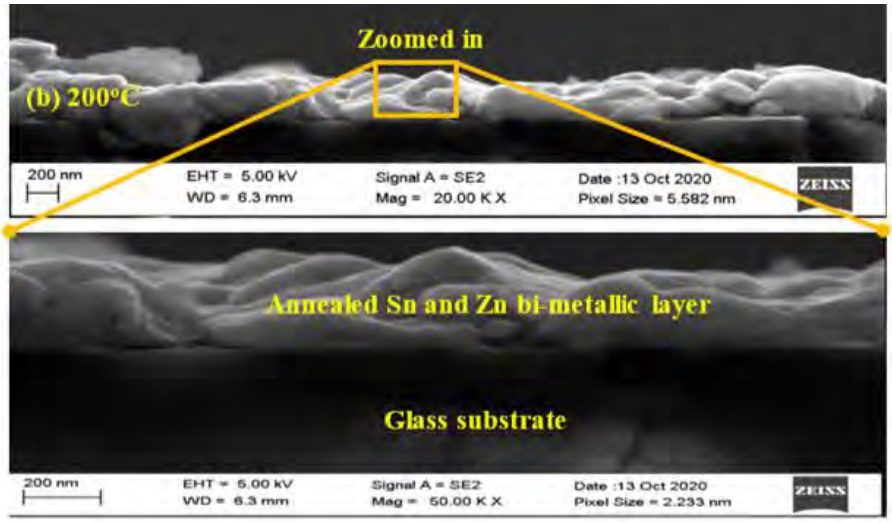

Figure 4.20: *b) Cross section view of micrograph of Zn-Sn bilayer annealed at 200 ºC*

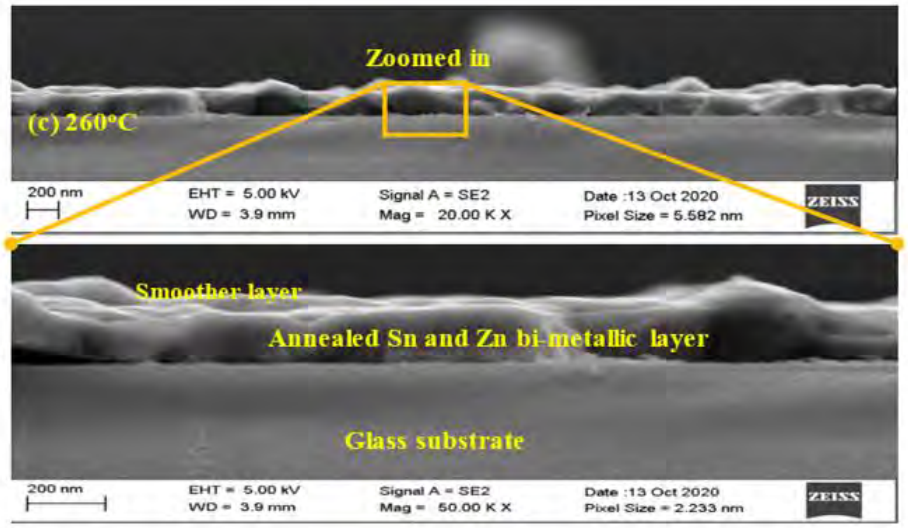

Figure 4.20: *c) Cross section view of micrograph of Zn-Sn bilayer annealed at 260 ºC*

The evolution of the surface roughness of the samples was studied using AFM. It can be seen from the figure 4.21 that films are not smooth. The AFM micrograph analysis as shown in figure 4.21 report an R_a values for the samples annealed at 180 ºC, 200 ºC and 260 ºC to be 52.4 nm, 39.4 nm and 38.3 nm respectively. It is also observed that as the annealing temperature increases, the cluster of islands become bigger, as atoms diffuse and coalesce with each, forming a bigger continuous cluster. The decrease in root mean average roughness is also due to the Sn atoms diffusing to the surface through the cracks, with the tissue of Sn atom filling the cracks, by that reducing the roughness as observed from the SEM micrographs.

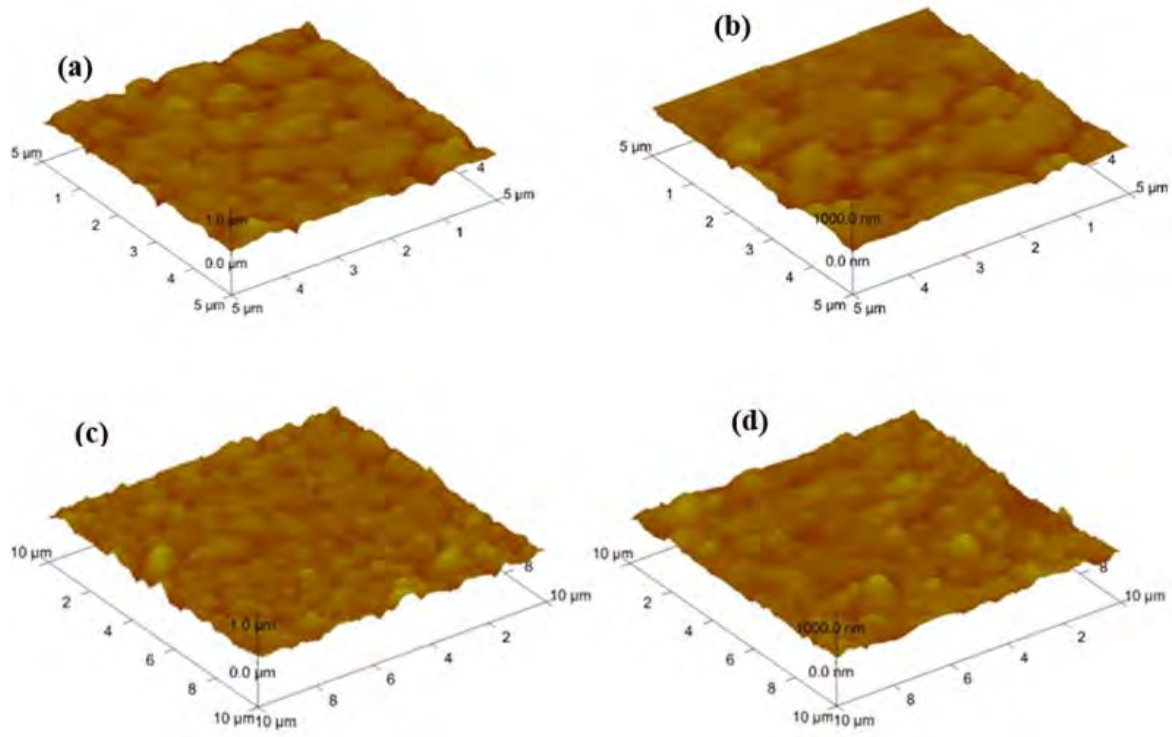

Figure 4.21: *AFM micrograph showing surface morphology of Zn-Sn bilayer: a) Pristine, b)bilayer annealed at 180 ºC, c) bilayer annealed at 200 ºC and d) bilayer annealed at 260 ºC.*

4.5.2 Microstructural Analysis of vacuum annealed metallic bilayer.

XRD pattern of the sample annealed at temperatures 180 ºC, 200 ºC and 260 ºC is shown in figure 4.22, with the as-deposited Zn-Sn metallic bilayer film caption as an insert. The diffraction patterns show Bragg peaks of lattice planes Sn [200], Sn [101], Zn [002] and Zn [001] for the as-deposited film in the insert.

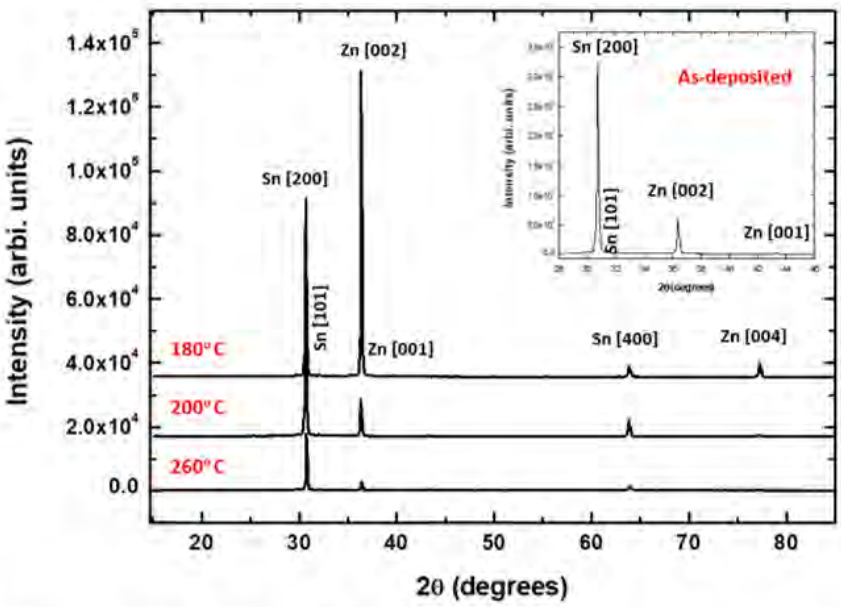

Figure 4.22: *XRD pattern of thin films annealed at different temperatures in the furnace, with an insert of as-deposited film.*

It can be observed that as the annealing temperature increases from 180 ºC to 260 ºC, the intensity of the Sn [200] peak decreases while that of the Zn [002] increase. This is because of mixing at the interface of Sn into the Zn film matrix. There is a little stress that is introduced in the sample as the films are heated. A zoomed-in plot, figure 4.23, of the d-spacing of the lattice plane of Zn and Sn preferential diffraction planes show a strain developing in the Zn layer as the annealing temperature increases. Whereas for the Sn film there is a stress developing in the film as observed by the decrease in the d-spacing of the layer. This could be related to the diffusing and mixing of the Sn atom trough the Zn film during annealing.

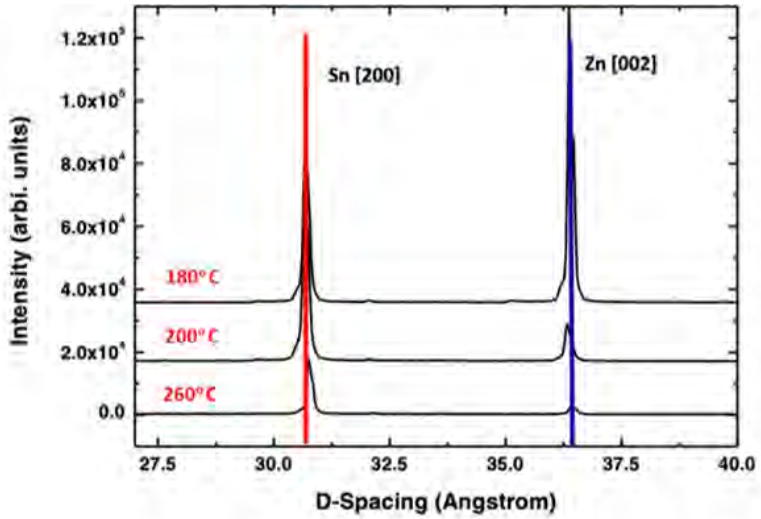

Figure 4.23: *XRD plot of the d-spacing of the preferential orientation of the crystals of Zn and Sn showing stress and strain.*

4.6 Non isothermal annealing of Zn-Sn thin films.

4.6.1 Combine RBS + Laser

Zn-Sn metallic bilayer thin film was subjected to non-isothermal annealing using femtosecond laser. This heating was done in the RBS chamber pumped down to a base pressure of 1×10^{-5} mbar. Laser parameters are shown in table 3.1 in the previous chapter. The focused laser spot was aligned such that it overlays the RBS beam spot on the sample stage. The photons from the laser and the alpha particles from the tandetron accelerator were overlapped on top of each other (*see figure 3.19 in chapter 3*).This was done in order to only probe (*with RBS*) the part of the sample that was heated by the laser.

The laser net-fluence [4.15] used in annealing the samples was calculated using the equation 4.3:

$$F_{net} = \frac{NE_p}{A} \tag{4.3}$$

where N is *number of pulses*, E_p, pulse energy, and A is the area of the laser spot. The spot size of the Gaussian beam [4.16] is calculated using equation 4.4:

$$w(z) = w_0 \sqrt{1 + \left(\frac{Z}{Z_0}\right)^2} \tag{4.4}$$

where $w_0 = \frac{M^2 \lambda}{\pi f}$

The spot was calculated to be to be approximately 0.7 mm. This was chosen in order to align it with the alphas spot, at the same time having sufficient fluence to induce the reaction in the sample.

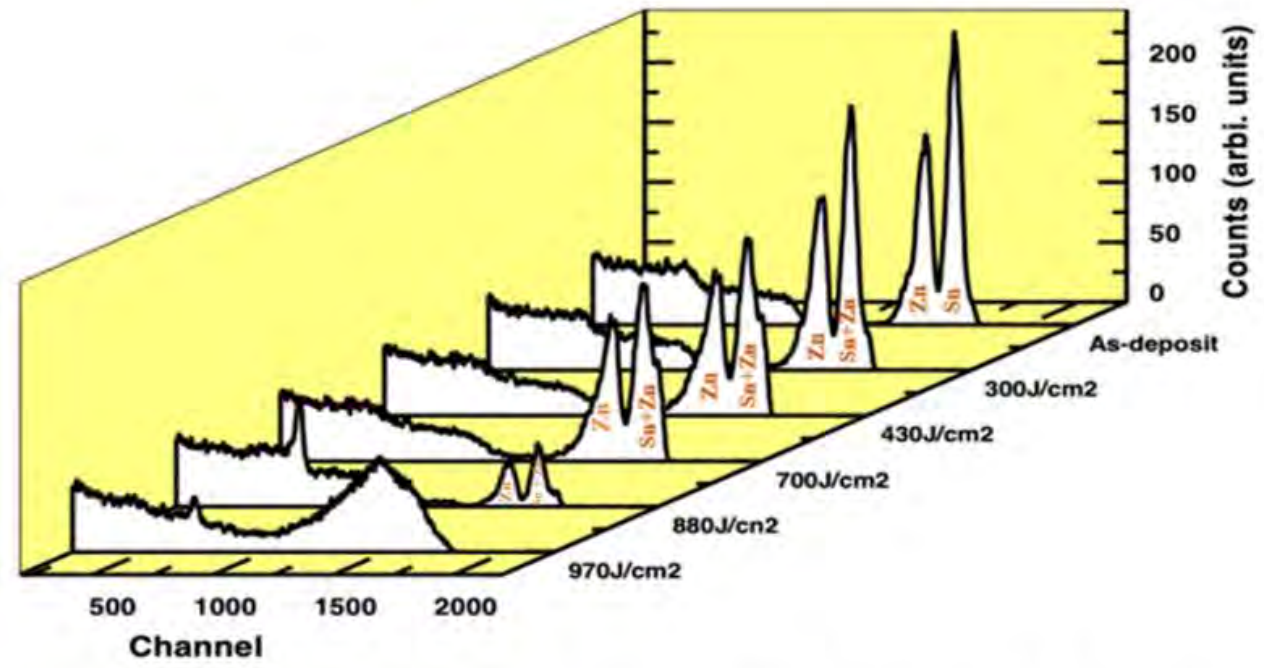

Figure 4.24: *Rutherford backscattering spectrometry of laser heated bi-metallic film showing evolution of the sample as fluence increases.*

Figure 4.24 shows the RBS spectra of laser annealed Zn-Sn thin films. From figure 4.24 it can be observed that the spectra of the as-deposited bi-metallic film show two peaks, that of Sn and Zn atoms, with the peak of Sn appearing at a higher channel. As the laser fluence is increased to 300 J/cm^2, the Sn and the Zn atom atoms start to mix at the interphase of the sample, this can be noticed by the emergence of a shoulder at the Sn peak, which relate to the two atoms mixing. As the laser fluence increases, the inter-mixing continues and the laser heating reached ablation threshold and the sample begins to loose atoms due to fluence being over the ablation threshold.

Simnra was used to simulate the RBS raw data, in order to elucidate more on the atomic depth profile evolution of the Zn and Sn atoms due to laser heating. From the simulated data, it appears that as the energetic photons of the laser interacts with the sample, the concentration of the Sn atoms diffusing into the Zn layer increases as the laser net fluence increases as depicted in figure 4.25.

***Figure 4.25**: Depiction of the Zn and Sn atoms as laser fluence increases.*

The Sn atom diffuses into the Zn top layer, through the porous microstructure of the Zn layer as reported in figure 4.4. This Sn atoms seem to evaporate off the sample as net fluence increases, this is confirmed by the decrease of the peak width of the 970 J/cm^2 net fluence sample. At lower net fluence the thickness appears to be constant with only Sn atoms diffusing through Zn layer, there is no evidence of a new crystallographic phase forming throughout this process. The plot of the depth profile atomic diffusion of the Zn and Sn atoms, is as shown in figure 4.26, clearly expressing how atoms migrate in the sample.

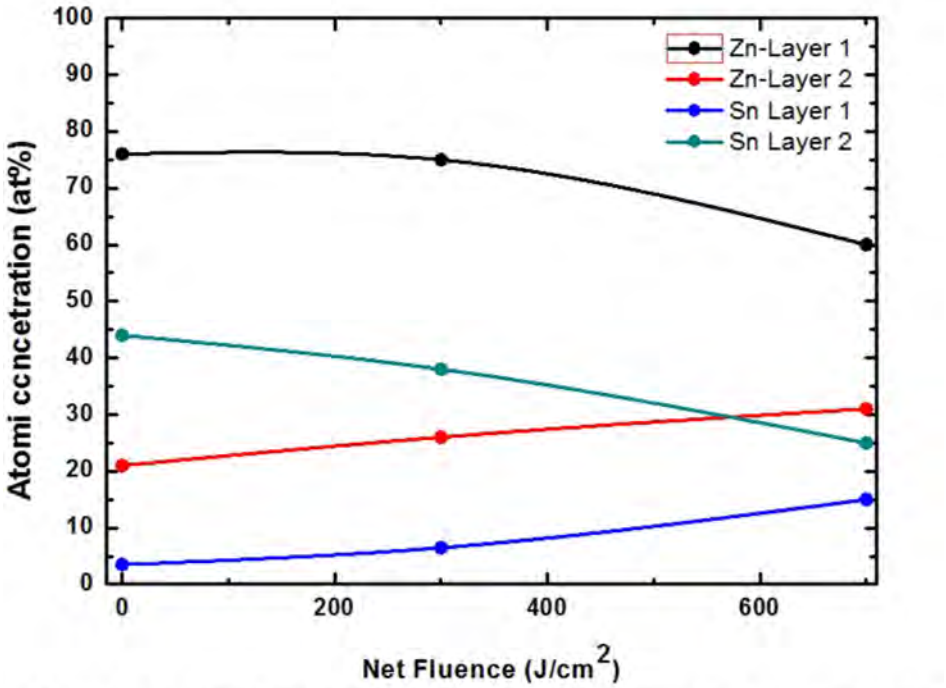

***Figure 4.26**: Plot of the diffusion depth profiling from the RBS raw data simulations.*

4.6.3 Morphology of non-isothermal annealed thin films

Surface morphology of laser annealed Zn-Sn metallic bilayer was studied with SEM, the secondary electrons and backscattered electrons were separately used to generate the micrographs samples. This assisted in better viewing the heat affected areas from femtosecond laser heating. Figure 4.27 shows the micrograph of a Zn-Sn which was subjected to 300 J/cm^2 laser net-fluence. The laser heat affected area is shown inside the yellow circle. From the figure, it can be observed that there is a morphological change where the laser interacted with the sample. The morphological change is due to mixing of the Zn and Sn atoms and recrystallization of the material.

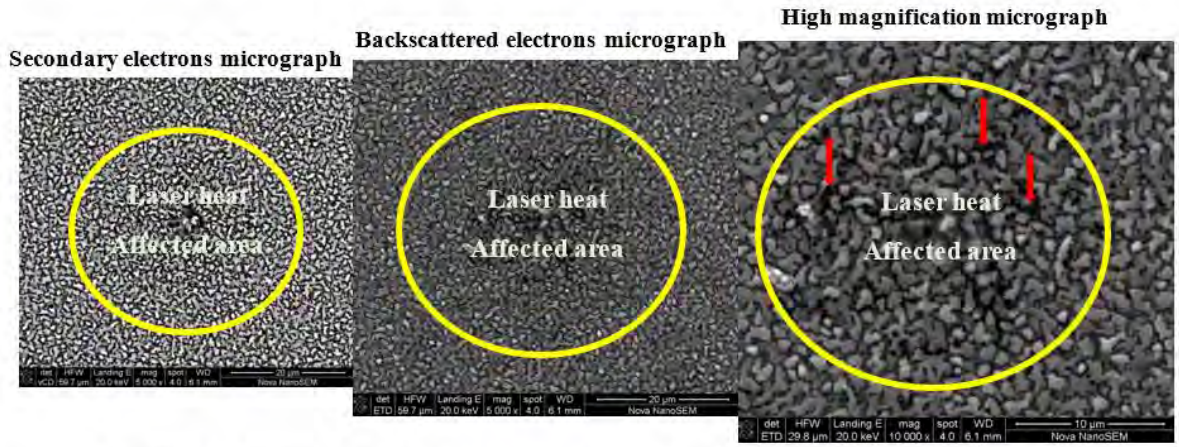

Figure 4.27: *Scanning electron micrograph of Zn-Sn bilayer laser annealed with fluence of 300 J/cm^3*

Figure 4.28 shows scanning micrograph of Zn-Sn bilayer annealed with fluence of 430 J/cm^3.From the figure, it can be seen that the laser showed Gaussian distribution with area of peak intensity shown by yellow encircled areas. It can also be seen that the areas of dark black that where seen in figure 4.27 and shown by red arrows disappear in this figure. This is a result of increased fluence which cause Zn and Sn to melt and fill the gaps between them.

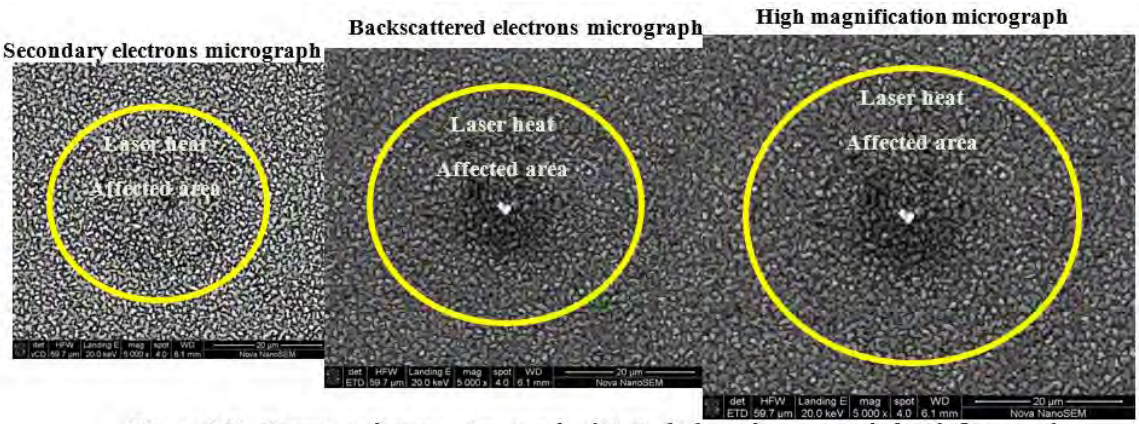

Figure 4.28: *Scanning electron micrograph of Zn-Sn bi-layer laser annealed with fluence of 430 J/cm^3*

Figure 4.29 show SEM micrograph Zn-Sn bilayer annealed with fluence of 720 J/cm^3.The outer margins of the laser as shown in figure 4.28 above become more prominent due to the increase in energy.

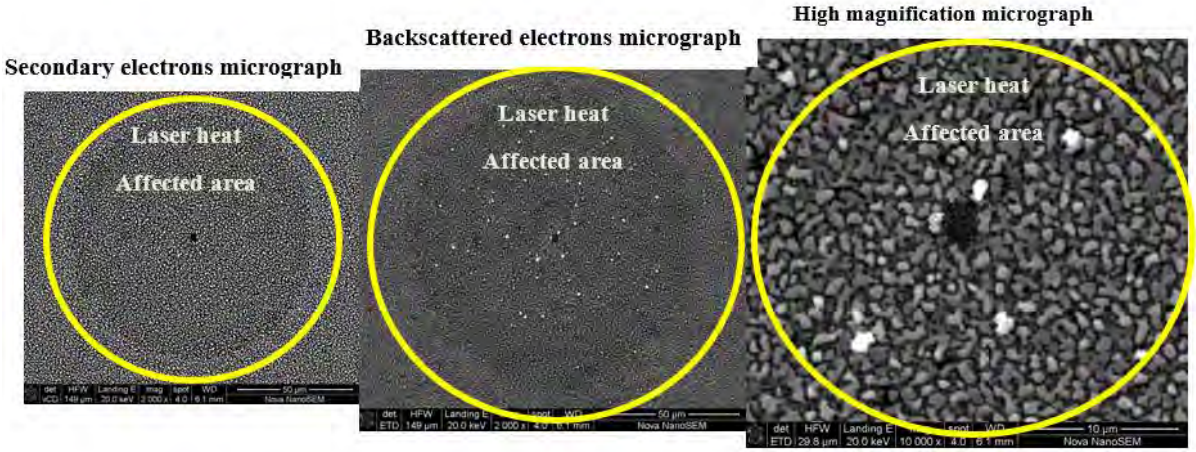

Figure 4.29: *Scanning electron micrograph of Zn-Sn bilayer laser annealed with fluence of 720 J/cm^3*

Figure 4.30 shows the evolution of surface roughness in relation to the laser fluence as it increases from 300 J/cm^3 to 720 J/cm^3. The R_a values for samples annealed with a laser fluence of 300 J/cm^3, 430 J/cm^{3}and 720 J/cm^3 are 43.2 nm, 79.6 nm and 42 nm respectively. The R_a values for samples annealed at 180 ºC, 200 ºC and 260 ºC were 52.4 nm, 39.4 nm and 38.3 nm respectively. This shows a decrease in R_a with an increase in temperature i.e. the samples became smooth with heating. This can be seen in figure 4.21.

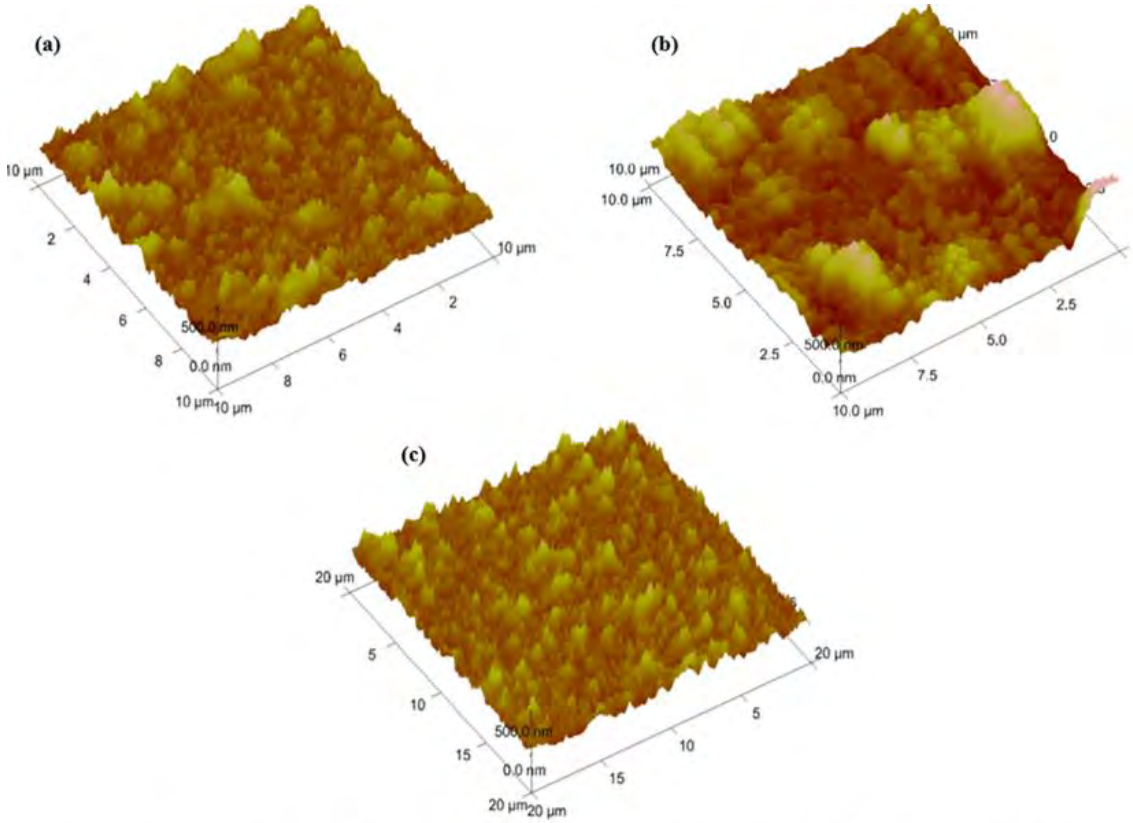

Figure 4.30: *AFM micrographs of Zn-Sn bilayer annealed with laser at different fluence with a) 300 J/cm^3,b) 430 J/cm^3, and c) 720 J/cm^3.*

4.7 Reference

[4.1] Oura, K., Lifshits, V.G., Saranin, A.A., Zotov, A.V. and Katayama, M., Surface Science: An Introduction. 2003. *Berlin: Springer*.

[4.2] Pimpinelli, A. and Villain, J., 1999. *Physics of crystal growth* (p. 400). Cambridge: Cambridge University Press.

[4.3] Venables, J., 2000. *Introduction to surface and thin film processes*. Cambridge University Press

[4.4] Moridi, A., Ruan, H., Zhang, L.C. and Liu, M., 2013. Residual stresses in thin film systems: Effects of lattice mismatch, thermal mismatch and interface dislocations. *International Journal of Solids and Structures*, *50*(22-23), pp.3562-3569.

[4.5] Chen, Y.Y., Duh, J.G. and Chiou, B.S., 2000. The effect of substrate surface roughness on the wettability of Sn-Bi solders. *Journal of materials science: materials in electronics*, *11*(4), pp.279-283. [4.6] Thabethe, T.T., 2017. *The interfacial reaction and analysis of W thin film on 6H-SiC annealed in vacuum, hydrogen and argon* (Doctoral dissertation, University of Pretoria).

[4.7] Goodwin, F.E., 2018. Zinc and zinc alloys. In *Springer Handbook of Materials Data* (pp. 431-442). Springer, Cham.

[4.8] Li, W.L. "Microstructure and adhesion strength of Sn-9Zn-1.5Ag-xBi (x=0wt% and 2 wt. %) /Cu after electrochemical polarization in a 3.5wt% NaCl solution", Journal of Alloys and Compounds

[4.9] Pondo, K.J., 2010. *In Situ Real-Time Rutherford Backscattering Spectrometry Study of Ni/Ge Interaction* (Doctoral dissertation, University of Zambia).

[4.10] Theron, C.C., Lombaard, J.C. and Pretorius, R., 2000. Real-time RBS of solid-state reaction in thin films. *Nuclear Instruments and Methods in Physics Research Section B: Beam Interactions with Materials and Atoms*, *161*, pp.48-55.

[4.11] Wang, Y. and Nastasi, M., 2011. Handbook of modern ion beam materials analysis. *MRS BULLETIN*, *36*

[4.12] Menzinger, M. and Wolfgang, R., 1969. The meaning and use of the Arrhenius activation energy. *Angewandte Chemie International Edition in English*, *8*(6), pp.438-444.

[4.13] Hamada, N., Hamada, M., Uesugi, T., Takigawa, Y. and Higashi, K., 2010. Effect of small addition of zinc on creep behavior of tin. *Materials transactions*, pp.1009131184-1009131184.

[4.14] Shrestha, T., Gollapudi, S., Charit, I. and Murty, K.L., 2014. Creep deformation behavior of Sn–Zn solder alloys. *Journal of Materials Science*, *49*(5), pp.2127-2135.

[4.15] Shimoda, K., 2013. *Introduction to laser physics* (Vol. 44). Springer.

[4.16] Tan, D., Zhang, B. and Qiu, J., 2021. Ultrafast Laser Direct Writing in Glass: Thermal Accumulation Engineering and Applications. *Laser & Photonics Reviews*, *15*(9), p.2000455.

CHAPTER 5

Summary and conclusions

5. Introduction

The aims and objectives of this study were presented in **Chapter 1** of this thesis. In this chapter, an overall summary of this study is given and conclusions based on the results presented in preceding chapters are presented. Possible directions for future studies are also suggested.

The overall aim of this study was to carry out a comparative study of isothermal annealing and non-isothermal annealing (*laser*) of Zn-Sn metallic bilayer. Metallic bilayers of Zn-Sn were successfully deposited with electron beam system (*e-beam*) on a glass substrate. The thickness of each layers was 50 nm as measured by crystal monitor. The thin films were characterized with RBS, SEM, AFM and XRD after being subjected to isothermal and non-isothermal annealing.

5.1 Isothermal annealed and vacuum annealed samples

In the first part of this work, Zn-Sn metallic bilayer was subjected to isothermal annealing inside RBS chamber. It was observed that at the bilayer was annealed there was intermixing of Zn and Sn, however, no reaction and alloying of the two elements occurred.The absence of a peak belonging to Zn-Sn further support that no alloying taking place during isothermal anneling of the bilayer. The activation energy and diffusion coefficient of Zn and Sn intermixing was calculated and found to be 0.46 eV and 44.6 kJ/mol respectively. These values agrees with the findings of Hamada et.al [1] and Shrestha et.al [2] respectively who found that it falls within 41.0 kJ/mol- 45.0 kJ/mol range.

Morphological changes where observed in the bilayer as it was annealed. As the temperature increases, the surface of the bilayer become smooth when observed from the SEM micrographs.AFM also showed a decrease in R_a value as the temperature increases supporting what was observed in the SEM micrograph.

5.2 Non-isothermal annealed samples

The second part of this study involved subjecting the Zn-Sn bilayer to non-isothermal annealing i.e. laser annealing while probing with RBS.The samples were laser annealed inside RBS as explained in Chapter 3, there after characterized with SEM and AFM.

Similar to isothermal annealing where increasing temperature led to mixing of Zn-Sn, increasing fluence led to intermixing of Zn-Sn.SEM micrograph showed morphological changes due to mixing and recrystallization of the material. Furthermore, as the fluence increased from 300 J/cm^3 to 720 J/cm^3 it was observed that the gaps that existed between the atoms at lower fluence disappeared at higher fluence. This due to the fact that atoms melted as fluence increased and filled the gaps that were seen at lower fluence.AFM of laser annealed sample, unlike that of vacuum sample which showed a decrease in R_a with increasing temperature, there is no specific trend that could be observed.

5.3 Future outlook

The work presented in this thesis is part of a long term project within the Tandetron Laboratory of iThemba LABS-NRF, the aim of which is combine laser and RBS in the study of thin films. Of particular interest is the comparison between isothermal and non-isotherm (laser annealing) of thin film. Based on the results from this thesis, the following investigations will be carried out in the near future:

- XRD of the laser annealed spot in order to determine phases present.
- The effects of varying the thicknesses of Zn and Sn.
- The effects of using different substrates on activation energy.
- The effects of varying laser parameters

5.4 References

[1] N. Hamada *et. al.,* Effect of Small Addition of Zinc on Creep Behavior of Tin, Materials Transactions, Vol.51, No.10 (2010), pp. 1747-1752

[2] T. Shrestha *et al,* Creep deformation behavior of Sn–Zn solder alloys, J Mater Sci (2014) 49:2127–2135

APPENDIX A

Isothermal annealed spectra

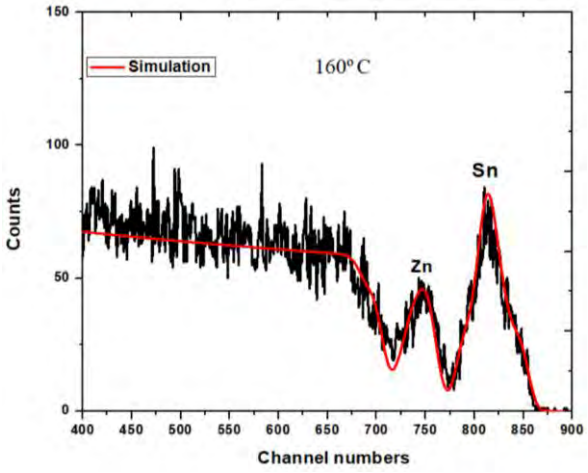

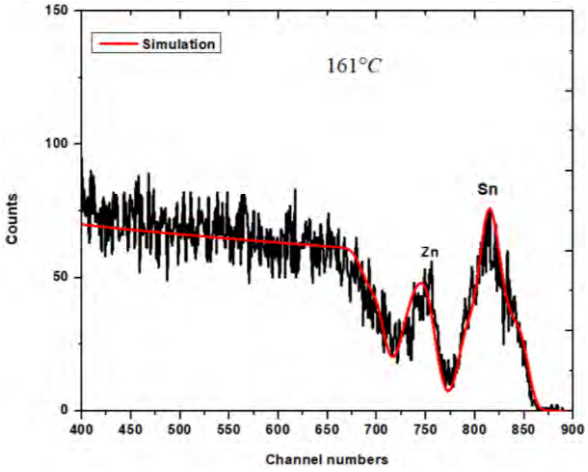

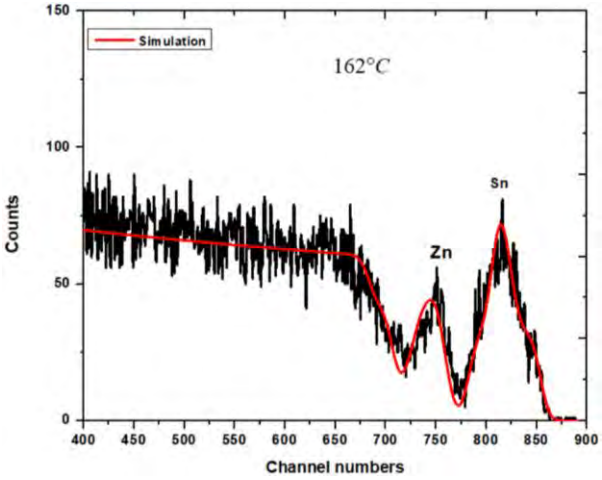

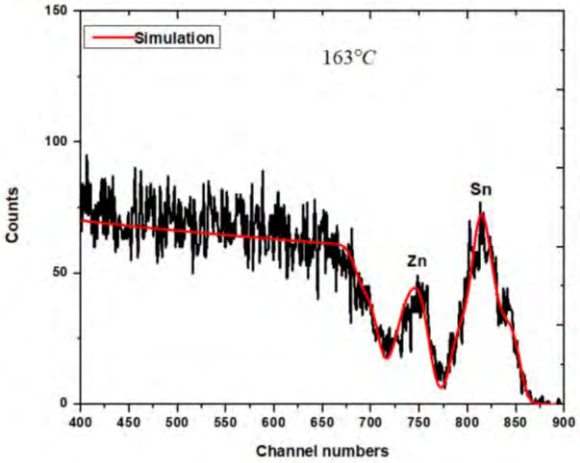

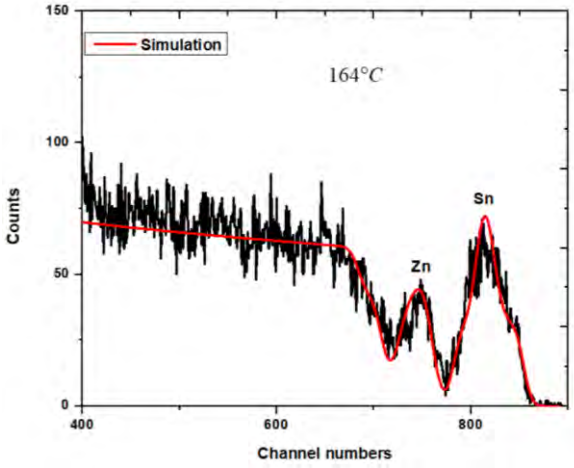

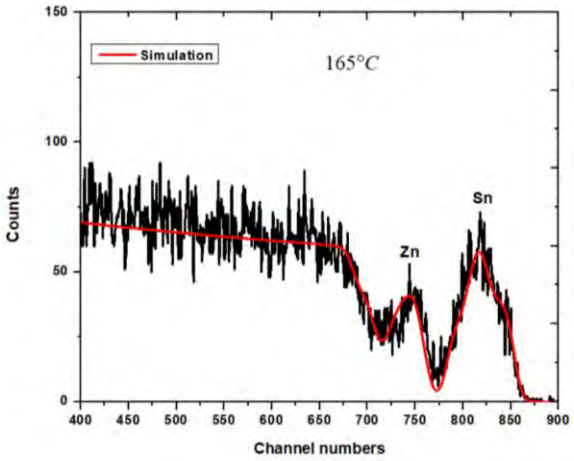

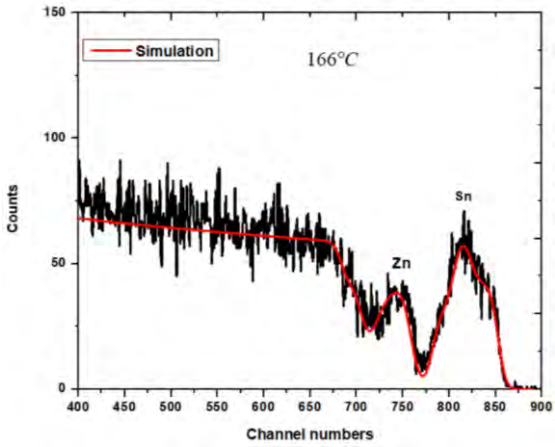
Simulation
166°C
Sn
Zn
Counts
Channel numbers

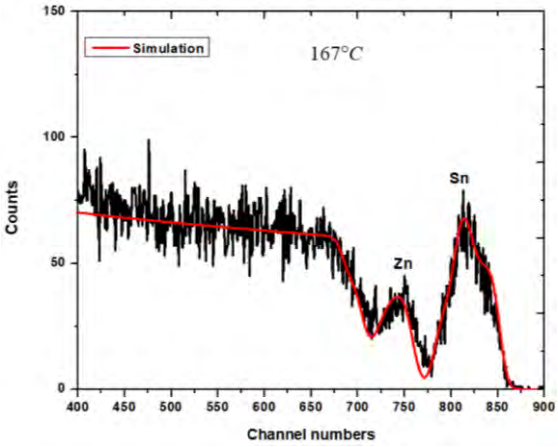
Simulation
167°C
Sn
Zn
Counts
Channel numbers

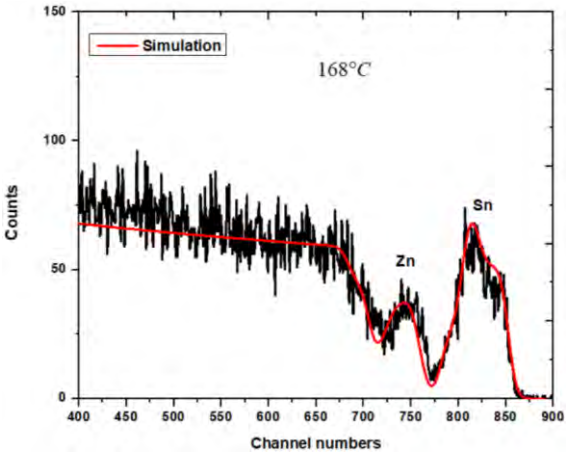
Simulation
168°C
Sn
Zn
Counts
Channel numbers

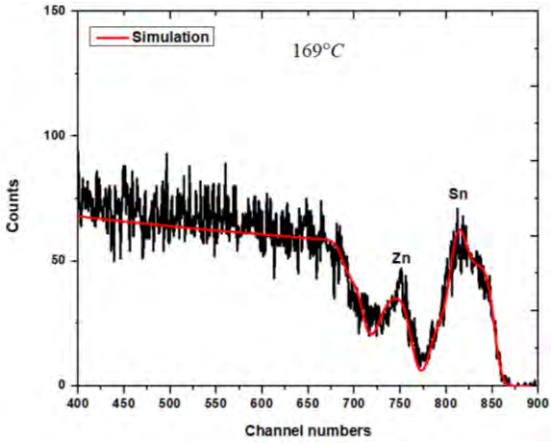
Simulation
169°C
Sn
Zn
Counts
Channel numbers

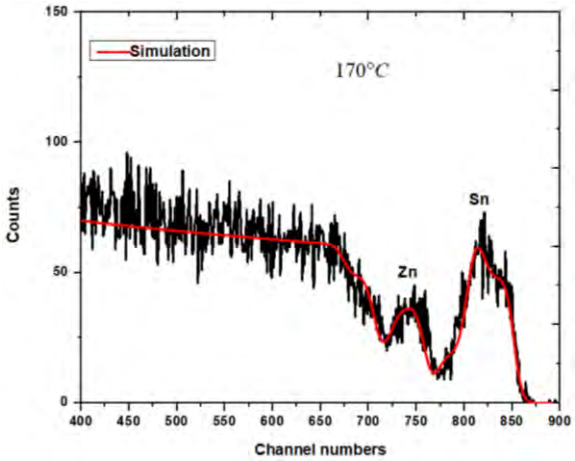
Simulation
170°C
Sn
Zn
Counts
Channel numbers

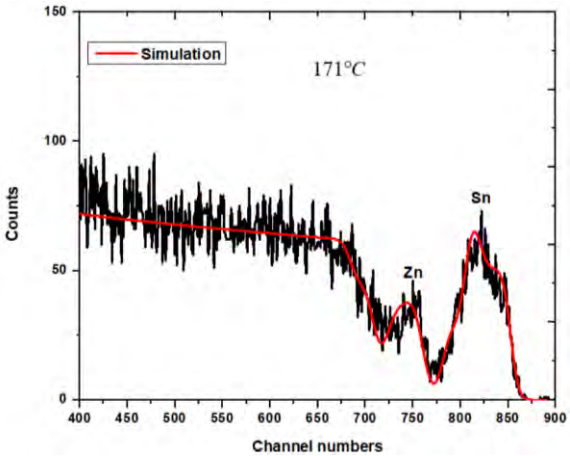
Simulation
171°C
Sn
Zn
Counts
Channel numbers

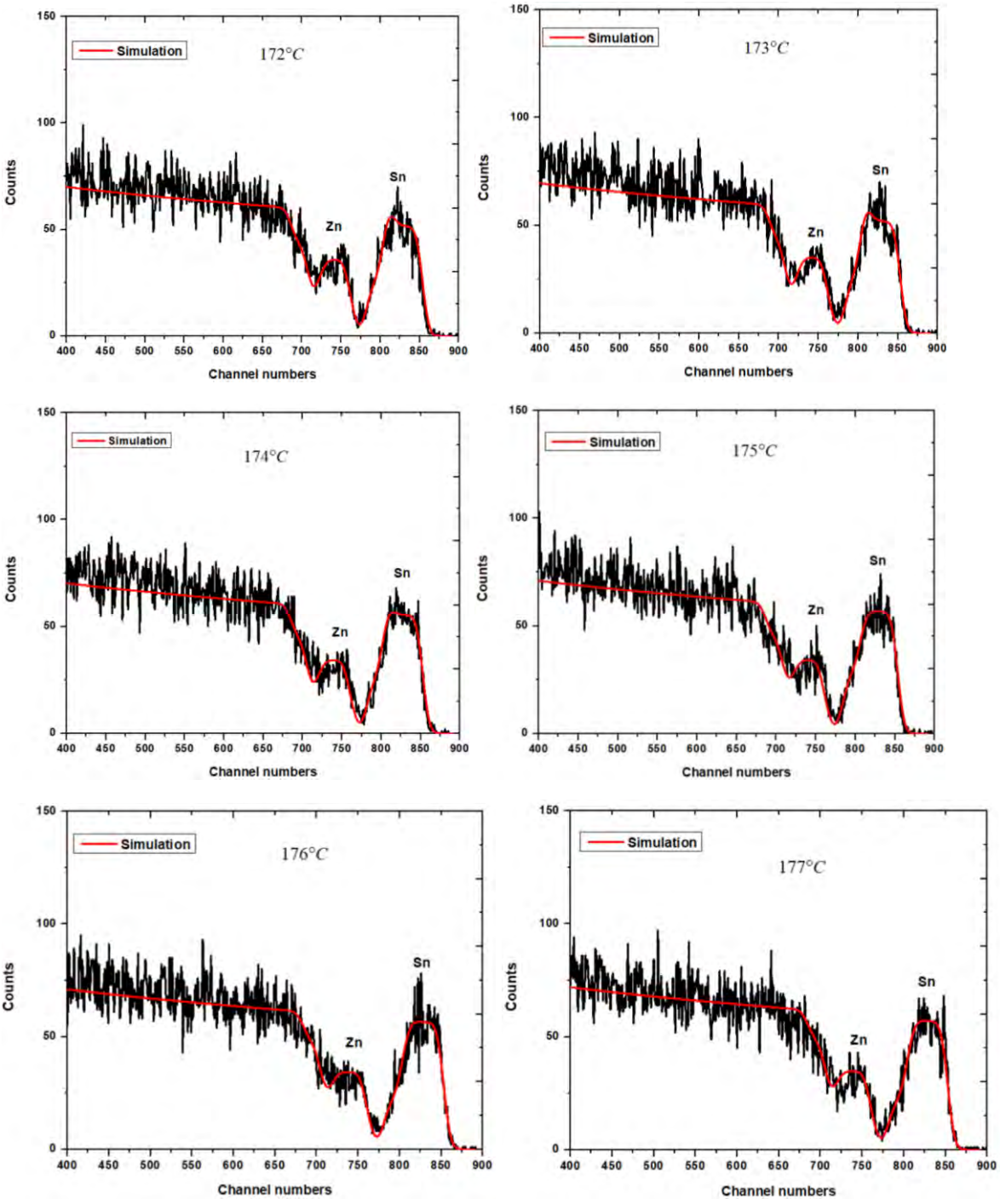
Simulation
172°C
173°C
174°C
175°C
176°C
177°C
Sn
Zn
Counts
Channel numbers

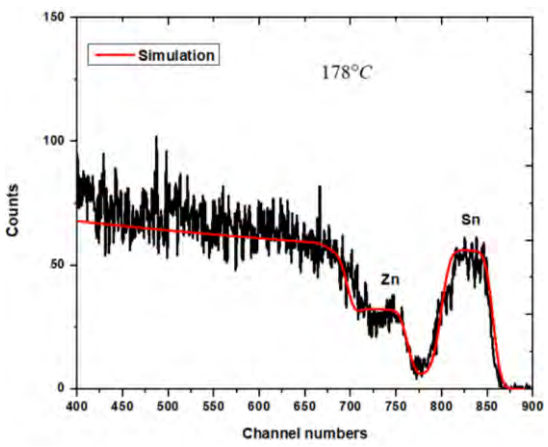
Simulation
178°C
Sn
Zn
Counts
Channel numbers

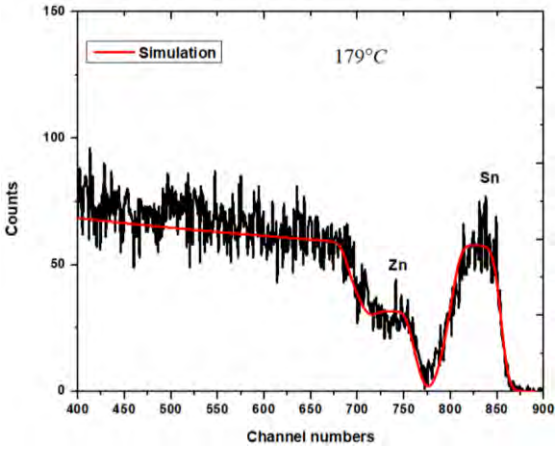
Simulation
179°C
Sn
Zn
Counts
Channel numbers

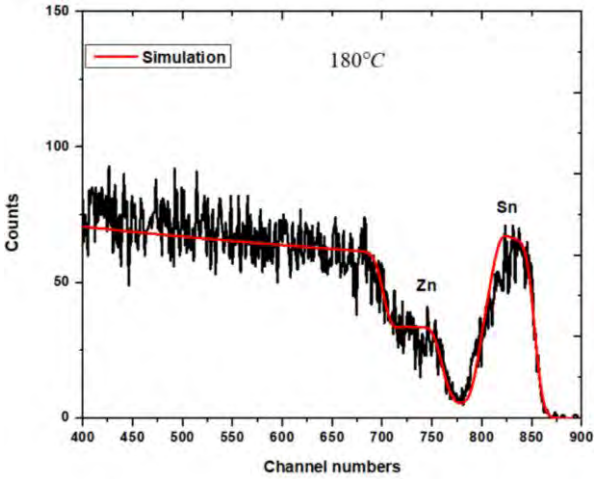
Simulation
180°C
Sn
Zn
Counts
Channel numbers

APPENDIX B

Non-isothermal annealed spectra

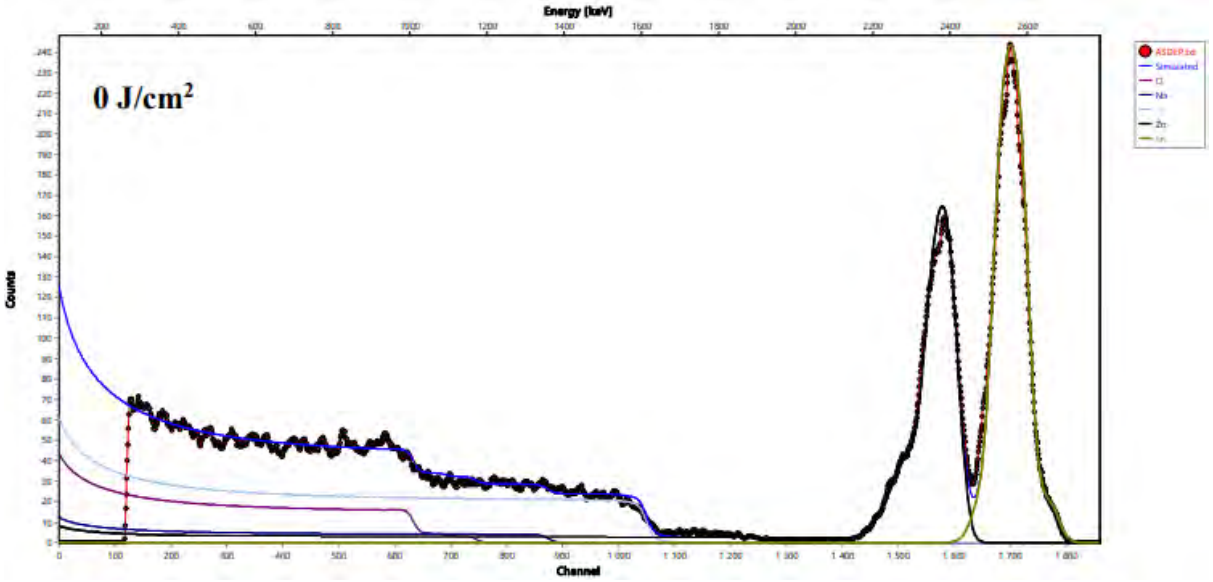

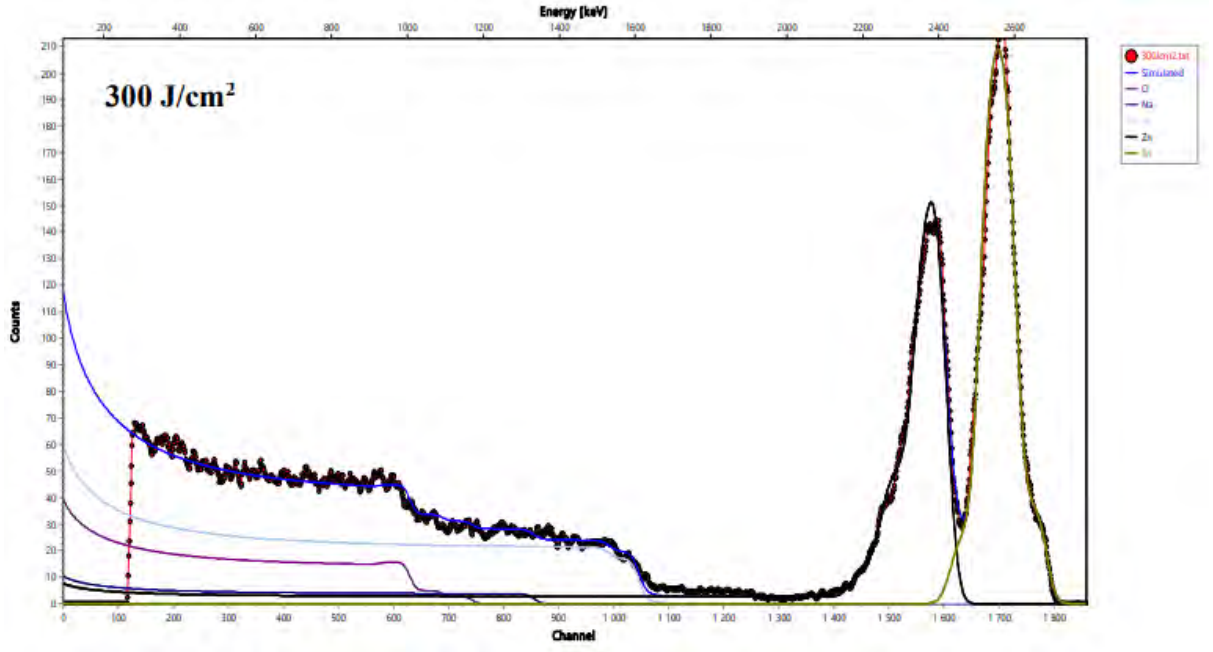

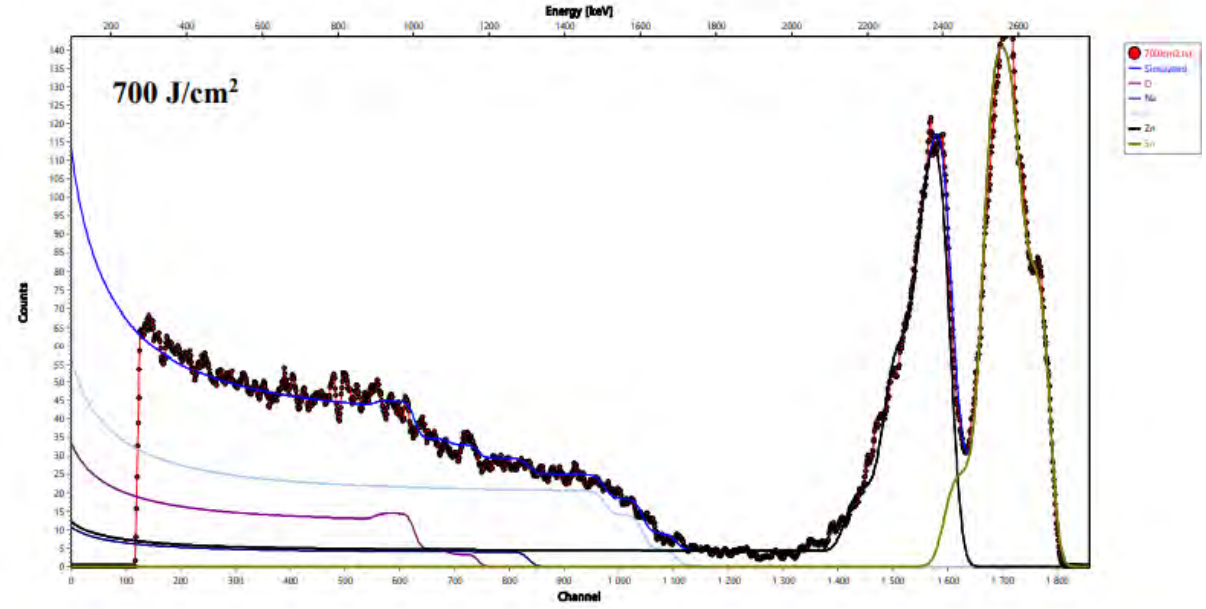
Energy [keV]
700 J/cm²
Counts
Channel

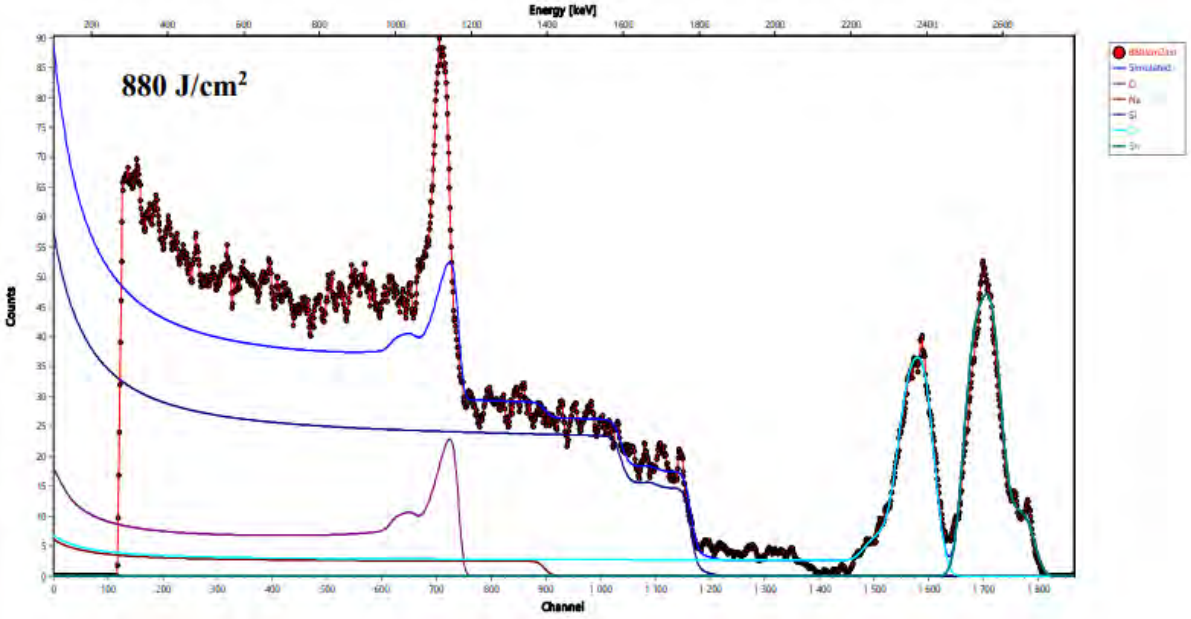
Energy [keV]
880 J/cm²
Counts
Channel